# Multi-fold TDEM Experiment Design for Near-Surface Conductivity Mapping

Eric M. Kazlauskas

*Thesis submitted to the faculty of the Virginia Polytechnic Institute and State University in partial fulfillment of the requirements for the degree of*

Master of Science
In
Geosciences

Chester J. Weiss
Madeline E. Schreiber
James A. Spotila

August 2nd, 2010
Blacksburg, VA

Keywords: time domain electromagnetics, experiment design, Kentland Farm geology, 1D inversion, depth to bedrock, conductivity mapping, zero-crossing moveout

# Multi-fold TDEM Experiment Design for Near-Surface Conductivity Mapping

Eric Kazlauskas

ABSTRACT

Multi-fold Time Domain Electromagnetics (TDEM) is a novel experimental approach that couples elements of traditional land-based TDEM survey designs to obtain a robust data set. This design inherently accommodates a broad range of possible Earth models through a rich combination of analysis opportunities making it ideally suited for reconnaissance. Kentland Farm, VA was chosen as the test site, for its ease of access and interesting geologic features such as river terraces and karstic landscape. Three independent methods of analyzing the 3-component data set each provided unique insights into the subsurface electrical structure through a complementary interpretation. Synthesis of log-normalized $\partial t\mathbf{B}_z$ pseudo-sections provided a first-order analysis of the lateral and vertical heterogeneities of the profile. A Zero-Crossing Moveout (ZCMO) analysis used a brute-force grid-search inversion to estimate the two-layer Earth model that best-fit the observed moveout times for a range of interface depths. By using the ZCMO result as an initial model, regularized 1D Occam inversions determined a 3-layer electrical structure consisting of a 3.5 m – 5 m thick resistive upper layer, over an 12.5 m – 15 m thick conductive layer, overlying a resistive half-space. From correlation of the inverse solutions with ZCMO derived conductivity models and prior resistivity information, the depth to the limestone bedrock was approximated to be 16 – 20 m. The delineation of the bedrock depth provided additional support for the fill-cut terrace formation model (Ward et al., 2005), as well as possible evidence of groundwater drainage on the 40 m terrace at Kentland Farm.

## Acknowledgements

First and Foremost, I would like to thank my advisor Chet Weiss. Thank you for taking a chance on an underachieving undergraduate and investing a painstaking amount of time, energy, and patience in guiding me through the Maxwell's complex universe. Your recognition of my strengths and an understanding of my weaknesses as a scientist instilled a desire for scientific knowledge and advancement that has lead to a discipline in which I am truly happy. I look forward to continuing our adventures in searching for the answers to future absurd claims about the Earth. I would also, like to thank my committee members, Maddy and Jim, for their patience and guidance through not only my thesis but also graduate life. Thank you to Ben Schwartz for his help in locating his field site and understanding of his work at Kentland Farm. Sincere
Thanks to Jake Beal for helping with anything that I needed, even non-seismological ones, especially keeping me sane throughout this process.

Thanks to Sam Fortson for teaching me how to program in Fortran and for development of the plot viewer which made my life a lot easier.
Thank you to the geosciences technical staff, especially Richard Godbee and Miles Gentry for their assistance in teaching me the ways of the UNIX. Thanks to Mark Lemon for various equipment issues particularly with 3104, as well as staying late as I frantically finished my posters. A special thanks to John Wooge and the staff at Kentland Farm for their assistance. Also, thanks to the geosciences administrative staff, especially Connie Lowe, for taking care all of the problems that I had and for getting on me when I needed it, even when the answer was in an e-mail that you had already sent that I missed.

Thank you to all of those who helped me in the arduous data collection process specifically: Kris Dix, Josh Whitney (Styx), Trevor Lee Johnson, Jesse Buckner, Cable Warren, and Doug Mckeown.

Thank you to all of the Geosciences faculty at Virginia Tech who have taught me over the years for their expertise in understanding a wide variety of Earth process. Also, thanks to all of the Geophysics grad students in 1070 and 1068 A for their friendship and conversation. Now its your turn to finish!

Heartfelt thanks to my mom and dad, Mariette and Peter, as well as my stepdad Wayne, for all of your encouragement and assistance in realizing my goals and ambitions. A special thanks to all of my brothers in TKPhi and all of my friends everywhere for their support throughout my 7 years in Blacksburg.

Finally, a very special thanks to Courtney Hook for her love and patience in putting up with all of the late nights and my grumpy demeanor throughout this final year.

# Table of Contents

## List of Figures

# Chapter 1: Introduction

## 1.1 Motivations and Purpose

Near surface geophysics has a broad spectrum of applications in shallow depths on the order of 10's of meters, as commonly seen in environmental/geotechnical applications, to depths on the order of 100's of meters for groundwater assessment and mining projects (Butler, 2005). With the high degree of heterogeneity that is characteristic of near surface environments, sufficient vertical and lateral resolution desired from geophysical experiments is often difficult to achieve. This difficulty makes the selection of the appropriate geophysical method and survey design critical. Even though there is not a "golden goose" geophysical method that works in every situation, there are techniques that are inherently more advantageous depending on the geological setting and ultimate goal of the study. The choice of technique is strongly dependent on the contrast in physical properties between the target and the background, target depth, and the composition and thickness of the overburden (Sharma, 1997). Additionally, an analysis of the survey parameters which optimizes resolution of the target while minimizing the overall cost is essential. In summary, a broad understanding of the target of interest is a neccesity for the planning and execution of a successful geophysical survey.

One geologic environment in particular creates a wide range of geophysical imaging problems. Karst, found in predominately carbonate (limestone, dolomite) regions, accounts for approximately 20% of the Earth's land surface and 40% of the land surface in the eastern U.S (White et al., 1995). Extensive dissolution creates an irregular carbonate bedrock surface with features such as sinkholes and pinnacles, and promotes a conduit-drainage system that has the potential to route all surface drainage rapidly into the aquifer without sufficient filtration time (White et al., 1995). This rapid recharge of the aquifer coupled with the complexity and difficulty of delineating the discharge basin leads to water quality issues especially in areas of high agricultural activity. Soil-piping (sediment transport and removal through dissolution fractures) leads to the creation of voids in the soil matrix with an overlying arch that is prone to collapse when becoming too large to support the weight of the overlying soil (White et al., 1995). This process creates sinkholes that may endanger agricultural and urban infrastructure.

The use of geophysical methods such as ground penetrating radar (GPR), seismic methods, and DC resistivity are widely accepted for the evaluation of shallow karstic terrains (Butler, 2005); however, deeper karstic environments pose certain restrictions on these geophysical techniques. For example, thick conductive soil layers attenuate GPR signals limiting the resolution depth. Also, strong variability in acoustic impedance from a highly weathered, non-stratified bedrock surface coupled with near-surface inhomogeneities that may scatter signal pose difficulties for seismic imaging (Sumanovac & Weisser, 2001). EM methods however are sensitive to the variations in subsurface conductivity structure caused by pore fluids and geologic factors such as porosity, lithology, clay content, and fractures. Hence, EM methods are inherently sensitive to the increased secondary porosity of the weather limestone interface as well as the soil piping feature described earlier. This sensitivity coupled with the relative low cost of near surface EM measurements, makes the technique inherently well-suited for geologic mapping in karstic areas. Specifically, time domain electromagnetics (TDEM) is a broadband approach allowing for the investigation of the subsurface for a range of depths while ignoring the true earth conductivity as we are guaranteed some frequency band in the range of DC to MHz that samples the depths of interest. Hence, the goal of this project is to devise an optimal time domain electromagnetic survey design that maximizes the methods potential to detect vertical and lateral conductivity variations by incorporating a multi-analysis approach of a three-component data set, which samples the induced magnetic field in all three directions accommodating for the 3D Earth in which we measure.

### 1.2 Previous Studies into Optimal Experiment Design

The quality of any geophysical derived Earth model is dependent on the information content of the data set that is being used. Hence, we must strive to find an optimal experimental design that yields the maximum amount of subsurface information possible. In electromagnetic exploration, the signature in the observed responses is a function of the acquisition parameters outlined in the survey design such as the location of the transmitter (TX) and receiver (RX) with respect to the target of interest and various instrumentation considerations such as source characteristics, receiver sensitivity, and in situ processing. Previous studies have taken a numerical approach in defining the optimal survey design, employing techniques based on a

known target or range of targets. Rath el al. (1999) used 3D forward modeling to locate the optimal depth for a subsurface radio magnetic sounding device (RMS) to reduce the effect of the borehole itself. Sensitivity analyses involving the use of Fréchet derivatives (Boerner & West, 1989) can be performed to test the penetration depth of various experimental designs (Gomez-Trovino & Edwards, 1983; Chave, 1984). Taking a statistical approach, Maurer & Boerner (1998) employ global optimization theory, specifically genetic algorithms and linearized inversion, to develop an optimal experimental design that produces sufficient model resolution with minimal acquisition costs. Maurer et al. (2000) revisited the forward modeling, Fréchet derivative, data importance, and statistical approaches to experimental design, applying them to three defined earth models using direct-current (DC) resistivity and frequency domain electromagnetic methods and outlining the benefits and pitfalls of each. In addition, they solve a nonlinear optimization problem that quantifies the goodness of a singular experimental design to a range of earth models. Although statistical experimental designs yield high quality and cost effective array configurations, their dependence on *a priori* information serves to limit their application to mainly follow-up surveys where additional subsurface characterization is necessary, particularly for economic gain. For survey areas where the conductivity structure is undefined, the statistical experimental design approach may however result in inadequate survey parameters.

The successful geophysical experiment is dependent upon a design that accommodates the likely range of subsurface geometries and material properties. For reconnaissance work, it can be difficult to provide such bounds in places that are unexplored or potentially very complicated. Hence, we are drawn to exploring concepts in experiment design, which admit the greatest latitude in potential subsurface structure without compromising interpretation fidelity. Our approach to experimental design attempts to take into account these unknown parameters such as conductivity and geologic structure. By acquiring a robust data set that incorporates a variety of TX and RX configurations we can accommodate a wide range of earth models through multiple analysis techniques.

### 1.3 Multi-Fold TDEM Induction Offset Profiling

The goal of any transient electromagnetic survey is to first detect changes in the electrical conductivity in the underlying medium, and second, relate those changes to the geology or geologic processes of interest. The specific layout of TX and RX antennas imposes a strong bias on the region of the subsurface that most strongly affects the measurement. Although there exists a wide variety of TDEM array configurations, we will limit the discussion to three typical array configurations used in land-based, near surface applications (figure 1.1). A description of additional array configurations such as one-loop, coincident loop, dual loop, drill hole, and airborne can be found in Nabighian & Macnae (1991). Traditionally, the central loop (or in-loop) configuration is the most commonly used method with numerous examples seen in the literature (Hoekstra & Blohm, 1990; Meju et al., 2000; McNeill, 1994). In a central loop configuration, as the name implies, a large TX loop is laid out and RX measurements are made in the center (figure 1.1a). Central loop profiling is usually carried out either by making adjacent or overlapped measurements along the traverse. For fixed TX – RX offset profiling (Slingram configuration), the TX and RX are moved at a fixed separation along the survey line based on the desired exploration depth (figure 1.1b), estimated to be approximately one and a half to two times the depth of the target (Eaton & Hohmann, 1987). In fixed TX roving RX configuration (figure 1.1c), the TX is initially set in a fixed position and successive RX measurements are then made along the traverse at the user-defined interval. Traditionally, the roving RX method is used in prospect mining applications, where large TX loops (~200 m to 800 m's) are positioned with respect to the target and multiple receiver measurements are made at far distances (Ogilvy, 1986). Typically, loop sizes used in central loop sounding ( ≥ 40 m x 40 m) are large and require significant set up time resulting in very time consuming profiling. Fixed TX – RX offset configurations, however, employ much smaller loops resulting in much less cumbersome profiling making it an ideal configuration for reconnaissance. The ability for efficient profiling by using small, lightweight induction coil receivers is a principle that was taken under careful consideration in the designing of the surveying techniques used in this study. Multi-fold TDEM is a novel experimental design approach intended to yield a robust, multi-dimensional data set by implicitly incorporating a range of TX-RX configurations. Figure 1.2 shows the array set up for the survey conducted in this study; however, different set-up parameters such as TX loop size

and RX measurement interval may be changed based on site-specific properties (i.e. highly conductive/resistive environments, shallow/deep targets, etc). The three-component RX antenna is initially set at ± 20 m offset, L, from the TX antenna, and subsequent measurements are taken at 10 m intervals symmetric about the TX (a). The TX antenna is then moved 10 m down the survey line (b) and the split-spread survey in (a) is done again. This procedure is then repeated for TX increments of 10 m (c), (d), and (e) until the full-fold data set is complete. Fold in seismic methods is defined as the number of times a common midpoint is sampled in a survey (Sheriff & Geldart, 1995). The fold number varies depending on the separations desired for interpretation purposes. Consider the profile length of 180 m used in this study for example: the response from a 180 m TX – RX separation would sample the midpoint of our survey once resulting in single-fold geometry. If additional responses from TX – RX separations of 60 m and 120 m where included, the maximum fold would increase to three. Therefore, the fold number depends on the TX – RX separations desired for interpretation; hence, we refer to the experimental design as multi-fold. Because of the large number of measurements required for a multi-fold experiment, equipment considerations must be made. Set-up and relocation of a large (≥ 40 m x 40 m) TX loop are time consuming and impractical for rapid data acquisition. Therefore, a TX loop that is easily moved is essential. If the target depth of interest is limited to the upper ten meters a smaller single coil TX (5 m x 5 m or 10 m x 10 m) may be used. If the target depth is on the order of tens of meter a flexible "multi-turn" TX loop that increases the depth of exploration through the addition of multiple TX wire turns. Additional details on the detectability of various survey configurations will be given in chapter 3.

When dealing with an area absent of *a priori* information, deciding on the right survey parameters is not a trivial exercise. The benefits of this survey design lie in its inherent ability to interrogate the subsurface using a variety of survey configurations. Firstly, the initial fixed TX roving RX profiling allows for direct analysis of the eddy current diffusion characteristics for multiple positions along the traverse. Secondly, profiles for a range of fixed TX – RX offsets can be assembled accommodating for the unknown target depth. At short offsets (20 m), an interpretation similar to a central loop configuration can be made as outlined in McNeill (1994) with a 10 m x 10 m transmitter at a 15 m offset. Additionally, the interpretation of profiles for multiple offsets allows for the delineation of an ensemble of smaller conductive bodies from a single massive conductor. Finally, the ability to conduct data quality tests such as symmetry

tests, in which we can measure the transient response on either side of the transmitter for a given, offset are inherently present. Overall, the ability to analyze the transient responses in a variety of manners, outlined in chapter 4, is the primary benefit of this multi-fold experiment design.

### 1.4 Geologic Setting and Previous Work at Kentland Farm

Located in the Valley and Ridge geologic province, Kentland Farm (Figure 1.3) is home to extensive river terraces deposited by the New River. The six sets of unpaired, laterally discontinuous river terraces are located at approximately 10 m, 20 m, 40 m, 50 m, 80 m, and 128 m above modern river level (AMRL), respectively; these deposits contain interbedded cobble and gravel horizons in a dark red-brown soil matrix (Schultz and Bartholomew, 2009; Ward et al., 2005). The terrace deposits overly heavily karstified Cambrian Elbrook interbedded limestones and dolostones, which are prone to dissolution features shown in the form of extensive karst plains on the 20 m and 50 m river terrace. Our field site (outlined in black on Figure 1.3) was chosen for its access as part of the Virginia Tech College Farm Operation and because of the interesting geologic questions associated with geological features such as the river terraces and karst plains.

In spite of these interesting geologic features and the close proximity to the Virginia Tech campus (~ 10 mi), Kentland Farm (Figure 1.3) has been the focus of a limited number of prior studies. Harris et al. (1980) first noted that changes in soil mineralogy and degree of weathering of the terraces varied with elevation. A statistical analysis of the distribution of terrace deposits as they relate to elevation was performed by Mills & Wagner (1985), in which a broader description of the soil weathering characteristics of the individual terraces was used to correlate terrace ages. Ward et al. (2005) expanded on earlier cosmogenic radionuclide exposure dating (CRN) of cave deposits along the New River (Granger et al., 1997) and further constrained the river's episodic aggradation and incision history. CRN results yielded age constraints on the terrace abandonment ages for the three lower terraces at Kentland Farm (10 m, 20 m, and 50 m), correlating potentially to variations in sediment supply caused by climatic change (Ward et al., 2005).

A joint analysis of 2D electrical resistivity imaging (ERI) and time domain reflectometry

performed at two sinkholes on the 20 m and 50 m terrace by Schwartz et al. (2008) resulted in the first known soil moisture profiles derived from geophysical data in the area. The two ERI profiles on the 50 m terrace reveal fairly low conductivity values for the upper 20 m, ranging from 0.00051 S/m to 0.00787 S/m with the electrical trend being that of a resistor over conductor over resistor. The 20 m terrace was shown to have a similar electrical structure as the 50 m profiles, although with higher conductivity values ranging from 0.00152 S/m to 0.0125 S/m. In addition, the depth to the limestone bedrock interface was located from augured wells on the lower terrace and varies from 3.4 m to 7.6 m depth. A comparison of an ERI profile to gross soils groupings based on soil color and texture on a 50 m terrace revealed fairly resistive soil units with the most resistive unit being correlated to very hard, dark red soils (Schwartz et al., 2008). The depth to the bedrock interface on the 50 m terrace was not resolved and was interpreted to >15 m. Knowledge of the depth and characteristics such as topography and dip of the bedrock interface could provide additional constraints on the river's aggradation and incision history as well as assist in a further understanding of the hydrologic framework of the terraces.

Depending on the geologic setting (hydrologic and tectonic) and physical/chemical processes (weathering, faulting, and dissolution), conductivity values can vary by several orders of magnitude. Conductivity ranges for common geologic materials typical of the Kentland Farm area are shown in Figure 1.4 (Angenheister, 1982). The minerals that compose rocks are generally resistive, making the associated conductivity an indicator of factors such as porosity, clay content, fluid type, fluid saturation, etc. (Knight & Endres, 2005). Because conductivity increases with the fluid saturation, salinity, and clay content, by increasing the porosity, additional space is made available for fluids and clays to occupy. This in turn increases the conductivity of the medium. For example, limestones and dolostones are resistive especially if mineral cements have decreased their porosity, however, processes including weathering, faulting, and dissolution increases porosity resulting in higher conductivities. Further details on what EM responses measure is found in chapter 2. Surface soils classified at the Kentland Farm field site are Guernsey silt loam (silt loam, silty clay loam, and clay) and Unison and Braddock cobbly soils (Cobbly loam, clay, clay loam, and very gravely sandy clay loam) (USDA-NRCS, 2010), which are similar to those observed by Schwartz et al. (2008). As discussed previously, the ERI derived soil model (Schwartz et al. 2008) revealed very resistive soil even in the presence of clays. This could possibly be caused by the compact weathered soils having a lower

porosity and, in turn, lower fluid saturation. In addition, the clays contained increasing amounts of kaolonite with depth (Harris et al., 1980), which is a less conductive clay with a lower porosity (Santamarina et al., 2005). Because depth of penetration of electromagnetic fields is $\propto \sqrt{1/\sigma f}$, the presence of conductive clays does pose a problem; however with the resistive nature of the soils observed at Kentland Farm as well as the broad frequency spectrum inherent of TDEM, depth of penetration will unlikely be an issue for EM characterization of the upper few 10's of meters below the surface.

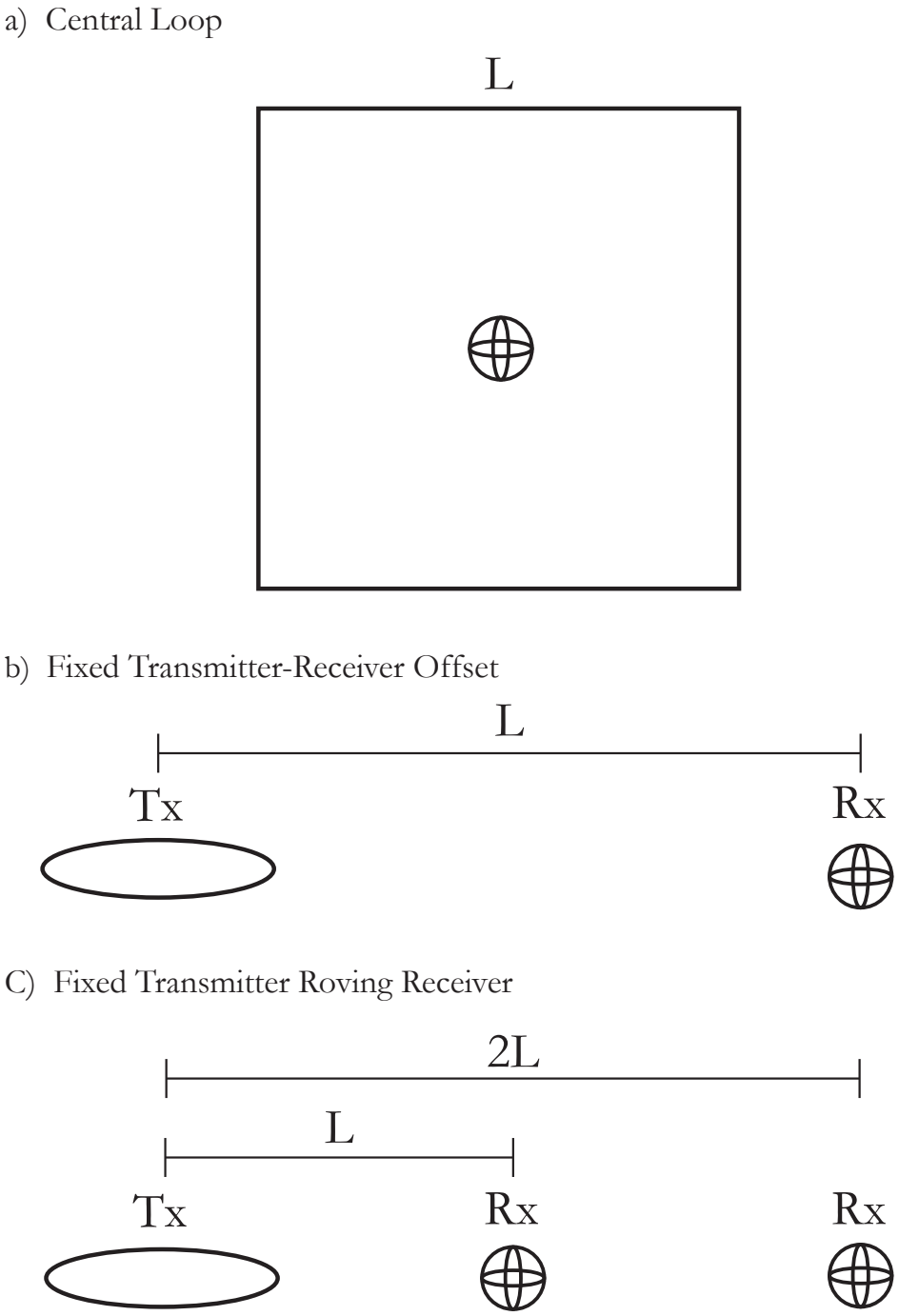


**Figure 1.1a-c.** Traditional TDEM survey configurations include: Central loop (a), fixed TX-RX offset (b), and fixed TX roving RX (c).

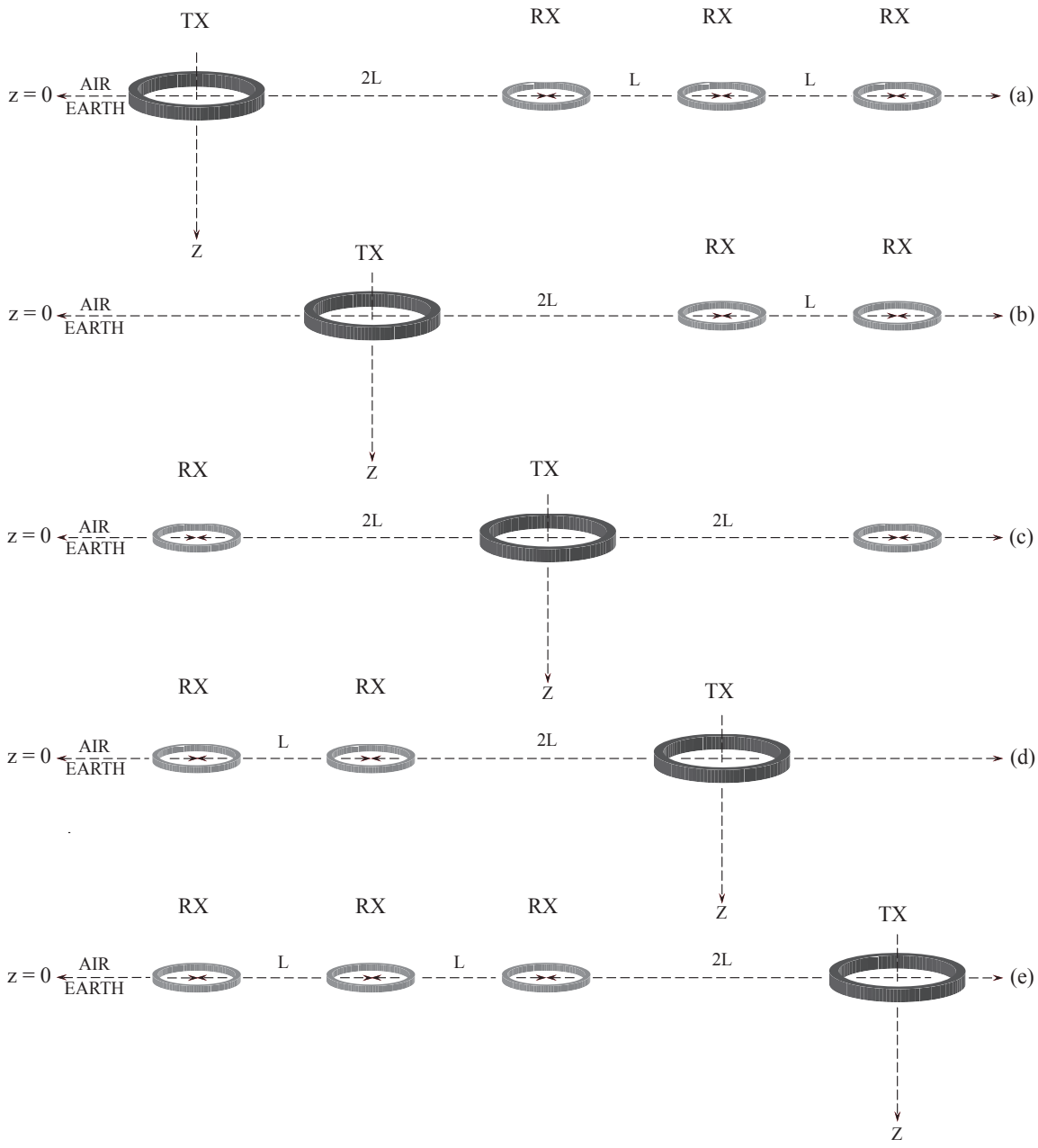


**Figure 1.2.** Schematic diagram of the Multi-Fold TDEM survey design

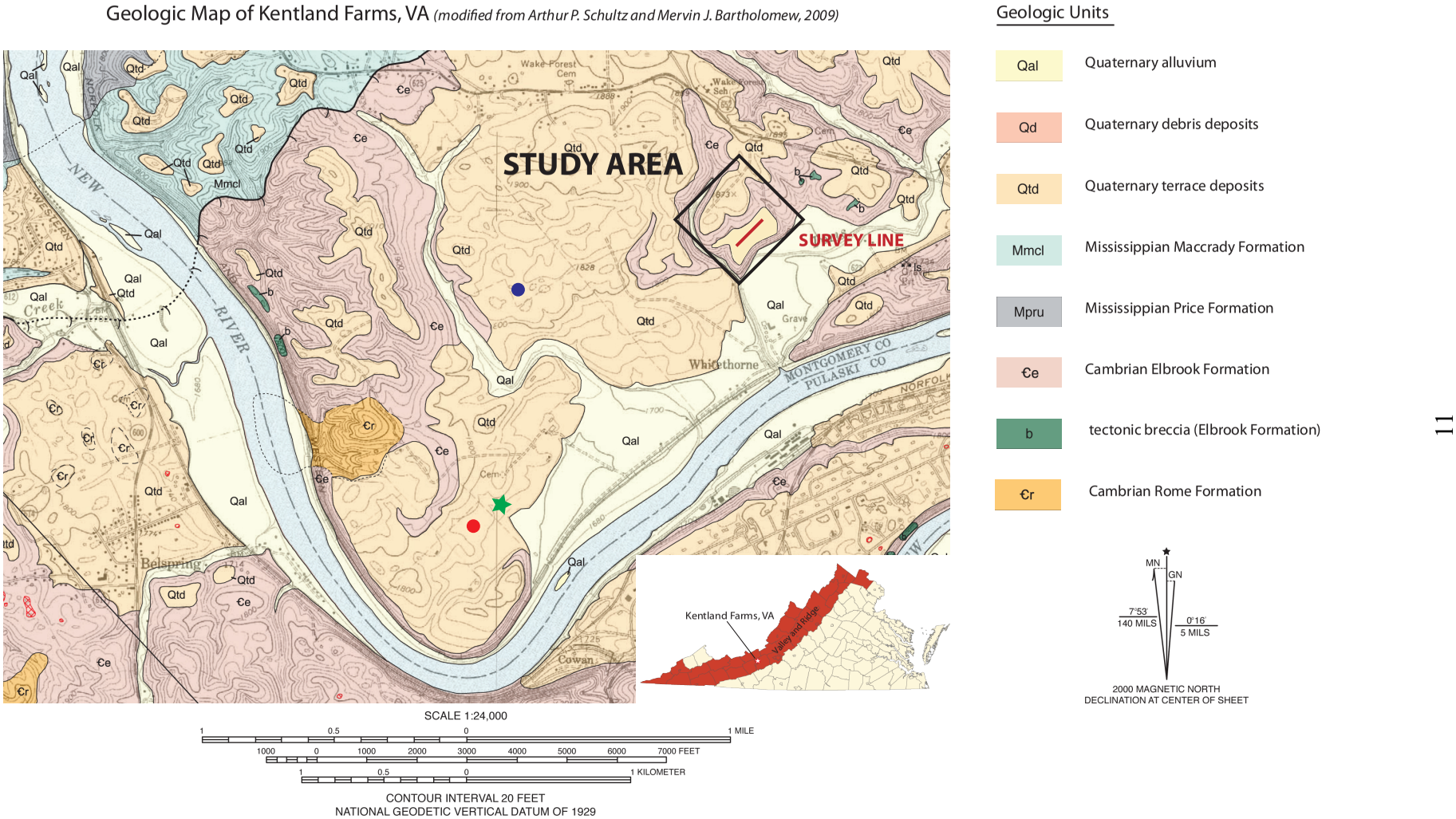


**Figure 1.3.** Geologic map of Kentland Farm, VA (modified from Schultz and Bartholomew (2009), www.dmme.virginia.gov). The field site is outlined in black with the 40 m profile line shown in red. The green star represents the additional survey location on the 20 m terrace. For reference, approximate locations for the 50 m (blue dot) and 20 m (red dot) terrace field sites used in Schwartz et al. (2008) are shown.

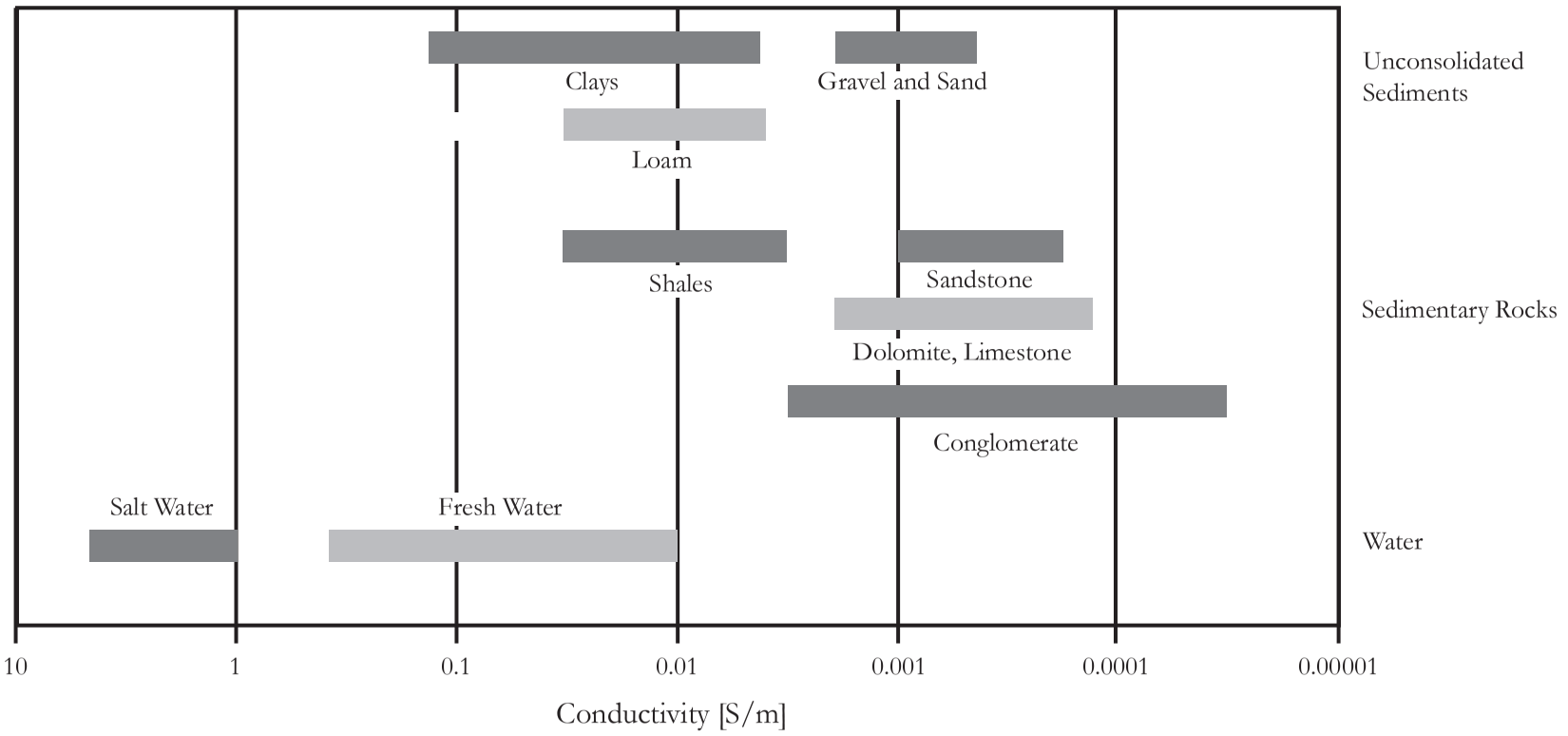


**Figure 1.5.** Electrical conductivity ranges for various Earth materials (Conductivity ranges taken from Angenheister (1982))

# Chapter 2: Principles of Time Domain EM Induction

## 2.1 What do EM responses measure?

Electromagnetic induction responses are a measure of subsurface bulk conductivity distribution $\sigma(\mathbf{r})$ or, in general, the Earth's ability to conduct electrical current. In turn, the conductivity of geologic material is dependent on factors such as porosity, clay content, fluid type, and fluid saturation. (Knight & Endres, 2005). The conventional wisdom is that bulk electrical conductivity is some sort of "average" for a given length scale, where the effect of smaller heterogeneities is "smoothed out" (e.g. Archie, 1942). However, a growing body of observational evidence suggests that such assumptions may not clearly hold. For example, lattice-preferred orientation of olivine grains in the lithosphere results in a bulk electrical anisotropy (Karato, 1990), as do thin laminations in sedimentary rocks. Hashim & Stirickmann (1962) demonstrates theoretically how the connectivity – not simply the volume fraction – of heterogeneous binary systems affects bulk conductivity. This result has been used to infer the presence of conductive graphite films deep in the crust (Wei et al., 2001). Furthermore, recent work on random and topological hierarchical resistor networks goes further in questioning the validity of the simple volume averaging approach. Such work has motivated the investigation of non-classical diffusion as a more reasonable model for subsurface transport of charge (Everett & Weiss, 2002; Weiss & Everett, 2007). As a demonstration exercise, Everett (2005) recently demonstrated the role of connectivity of the conductive phase. In his experiment, the transient response of buried intact and severed copper loops were compared. The tests revealed that only the intact copper loop demonstrated a response other than that of the background even though the same amount of metal was present in both. Furthermore, Everett (2005) points out that natural geologic features, such as dikes and faults, can also interrupt the electrical continuity causing possible misinterpretations of EM responses. By studying the characteristics of electromagnetic diffusion, we hope to gain further insight into the subsurface's charge transport mechanisms.

Controlled source electromagnetics methods, in which the electromagnetic field transmitted into the Earth is known, have a broad scope of application, from environmental to economic (Everett & Meju, 2005). Traditionally, TDEM was used in mining applications

specifically for the detection of massive sulfide deposits (Nabighian & Macnae, 1991). With the advent of easily acquirable, low cost equipment, the method has expanded into a host of near-surface applications. The ability to distinguish between conductive and resistive bodies, particularly between types of fluid, lends the EM methods to a range of applications including but not limited to: Development of groundwater flow models for contaminant zones (Buseli et al., 1990), delineation of the extent of salt water infiltration into fresh water system in coastal settings (Nielsen et al., 2007; Hoekstra & Blohm, 1990), geologic mapping of aquifer geometry (Danielsen et al., 2003), and fracture orientation analyses (Collins et al., 2006). In this project, I will apply multi-fold TDEM to map the bedrock surface in an effort to provide additional constraints in understanding the hydrological framework and geomorphological history of the river terraces at Kentland Farm, VA.

**2.2 Physics of the EM problem**

The physics of all classical electromagnetic phenomena are fully captured by Maxwell's equations:

$$\nabla \cdot \mathbf{D} = q \tag{2.1}$$

$$\nabla \cdot \mathbf{B} = 0 \tag{2.2}$$

$$\nabla \times \mathbf{H} = \mathbf{J} + \frac{\partial \mathbf{D}}{\partial t} \tag{2.3}$$

$$\nabla \times \mathbf{E} = -\frac{\partial \mathbf{B}}{\partial t} \tag{2.4}$$

where

$$\mathbf{J} = \mathbf{J}_s + \mathbf{J}_{ind} \tag{2.5}$$

In the equations above, $\mathbf{H}$ and $\mathbf{E}$ are the magnetic and electric field intensity vectors respectively, $\mathbf{B}$ is the magnetic induction, $\mathbf{D}$ is the electrical displacement, and $q$ is the charge density. $\mathbf{J}$ is the total current density resultant from the summation of the source currents $\mathbf{J}_s$ and the induced currents $\mathbf{J}_{ind}$. Equations (2.1) – (2.4) fully describe all classical electromagnetic phenomena. Ampère's law (2.3) states that magnetic fields arise from currents. Faraday's law (2.4) states that a *time varying* magnetic field generates an electric field. The following

constitutive relationships describe the relationship between the magnetic and electric field intensity vectors and the induced current density, magnetic induction, and current displacement vectors:

$$\mathbf{D} = \varepsilon\mathbf{E} \tag{2.6}$$

$$\mathbf{B} = \mu_0\mathbf{H} \tag{2.7}$$

$$\mathbf{J}_{ind} = \sigma\mathbf{E} \text{ (Ohm's Law)} \tag{2.8}$$

where ε is the dielectric permittivity, μ is the magnetic susceptibility, and σ is the electrical conductivity. The quantities ε, μ, and σ constitute the electrical properties of the geologic medium at the macroscopic or "bulk average" scale. When operating in generally non-magnetic regions we can safely ignore variations in μ and use the magnetic susceptibility of free space constant $\mu_0 = 4.7 \times 10^{-7}$ H/m. For low frequencies, where $\sigma >> \omega\varepsilon$, the quasi-static assumption states that the governing propagation mechanism is diffusion rather than wave propagation (Everett & Meju, 2005; Fitterman & Labson, 2005). That is, Maxwell's displacement current $\partial_t\mathbf{D}$ is dominated by the Ohmic currents $\sigma\mathbf{E}$. We now combine these constitutive relationships with the previously outlined Maxwell's equations under the quasi-static assumption:

$$\nabla \times \nabla \times \mathbf{E} + \mu_0\sigma\partial_t\mathbf{E} = -\mu_0\mathbf{J}_\mathbf{s}(\mathbf{r})\partial_t S(t) \tag{2.8}$$

where $\mathbf{J}_\mathbf{s}(\mathbf{r})S(t)$ is the source current density as a function of both time $t$ and position $\mathbf{r}$. Therefore, assuming a non-magnetic, quasi-stationary environment, electrical conductivity has the primary influence on electromagnetic diffusion. Notice that although the problem has been cast in terms of $\mathbf{E}$, the first term on the left hand side of the partial differential equation involves second order space derivatives, whereas the second term contains first order time derivatives. Hence, the equation has a structural similarity to the simple scalar diffusion equation – a similarity that's made more explicitly for problems with certain spatial symmetries.

### 2.3 Simplifications for a Loop over a Layered Earth

With the underlying principles in hand, the electromagnetic response of a TX loop over a horizontally layered conducting earth can now be computed. The solution here follows the

known solutions from Ryu (1970), Spies & Frishknecht (1991), and Weiss (2010). In doing this, we take advantage of the circular nature of our source (TX loop) by simplifying equation (2.8) into a scalar differential equation in cylindrical coordinates $(\rho,\phi,z)$ and using integral transform techniques (Weiss, 2010). If we approximate the loop source as a singular current filament $I$ we can define the spatial distribution of $\mathbf{J_s}(\mathbf{r})$ using Dirac's delta functions $\delta$. By integrating the volumetric current density over the circular loop where $\phi \in (0,2\pi)$, we get:

$$\mathbf{J_s}(\mathbf{r}) = \hat{\phi}\frac{Ia}{\rho}\delta(z+h)\delta(\rho-a) \tag{2.9}$$

where $a$ is the TX loop radius and $h$ is the TX loop height (Weiss, 2010). Assuming a purely azimuthal electrical field $E_\phi(\rho,z,t)$, equation 2.8 now simplifies into the differential equation (Weiss, 2010):

$$\frac{\partial}{\partial\rho}\left(\frac{1}{\rho}\frac{\partial}{\partial\rho}(\rho E_\phi)\right) + \frac{\partial^2 E_\phi}{\partial z^2} - \mu_0\sigma\frac{\partial E_\phi}{\partial t} = \frac{\mu_0 Ia}{\rho}\delta(z+h)\delta(\rho-a)\frac{dS}{dt} \tag{2.10}$$

In order to further simplify the differential equation, equation 2.10 is Fourier transformed $\Im$ to eliminate the time derivatives:

$$\left(\frac{\partial^2 u}{\partial\rho^2} + \frac{1}{\rho}\frac{\partial u}{\partial\rho} - \frac{u}{\rho^2}\right) + \frac{\partial^2 u}{\partial z^2} + \alpha^2 u = \frac{i\omega\mu_0 Ia}{\rho}\delta(z+h)\delta(\rho-a) \tag{2.11}$$

where $\Im\{E_\phi(\rho,z;t)\} = e_\phi(\rho,z;\omega) = u(\rho,z;\omega)$ and $\alpha^2 = -i\omega\mu_0\sigma$. By applying a first order Hankel transform $\mathcal{H}_1$, the first term on the left side of equation 2.11 can be simplified further into a mixed-domain, ordinary differential equation (Weiss, 2010):

$$\frac{\partial^2\overline{u}}{\partial z^2} + (\alpha^2 - \lambda^2)\overline{u} = i\omega\mu_0 Ia J_1(\lambda a)\delta(z+h) \tag{2.12}$$

where $\mathcal{H}_1\{u(\rho,z,\omega)\} = \overline{u}(\lambda,z,\omega)$ and $J_1$ is a first order Bessel function of the first kind. This can now be rearranged into the governing equations for the electric field in the non-conductive Air region and source free Earth region (Weiss, 2010):

$$\text{AIR: } \frac{\partial^2 \overline{u}}{\partial z^2} - \lambda^2 \overline{u} = i\omega\mu_0 I a J_1(\lambda a)\delta(z+h); \text{ where } z < 0 \tag{2.13a}$$

$$\text{EARTH: } \frac{\partial^2 \overline{u}}{\partial z^2} + (\alpha^2 - \lambda^2)\overline{u} = 0; \text{ where } z \geq 0 \tag{2.13b}$$

The homogeneous solutions to these equations are straightforward: $e^{\pm\lambda}$ where $z > 0$ and $e^{\pm(\lambda^2+\alpha^2)}$ where $z \geq 0$. These solutions introduce two unknown coefficients for model layer, which are found by imposing boundary conditions (BC). First, the radiation boundary condition requires that the electric and magnetic fields must decay to zero at infinite limits. The second BC, according to Faraday's law, is that the tangential electric fields must be continuous across conductivity boundaries. Therefore $\overline{u}$ must continuous across all boundaries. Additionally, the induced radial magnetic fields must also be continuous. Hence, our final BC states that $\partial\overline{u}/\partial z$ must also be continuous across all conductivity boundaries. Imposing the boundary conditions leads to a system of 2N linear equations with 2N unknowns. The unknowns are efficiently computed using recursion relation instead of the general Gauss elimination. The frequency response is then Fourier transformed to recover the transient electromagnetic response.

To understand qualitatively what is expressed by equations (2.1) – (2.13b) we describe the physical diffusion of induced eddy currents. In transient electromagnetic methods, a rapid, linear turn off of the TX current induces an electromotive force (emf) proportional time rate of change of the primary magnetic field. The emf drives geologically constrained eddy currents that decay via Ohmic loss following the termination of the source current. (Nabighian & Macnae, 1991). These induced eddy currents generate their own secondary magnetic field that opposes changes to the original magnetic field. The RX coil measures the magnitude of the induced voltage created by the secondary magnetic field. In a 1D Earth, this field has $\hat{\rho}$ and $\hat{z}$ components while the eddy currents diffuse downward and outward from the TX loop. The diffusion process can then be thought of as analogous to the behavior of a smoke ring being "blown" by the transmitter, as the two phenomenon share a mathematical description (Lamb, 1945; Nabighian, 1979). Figure 2.1 shows an example of eddy current diffusion for a TDEM offset-loop sounding. For a given TX – RX separation, the eddy currents are to the TX side immediately following the termination of the source current ramp resulting in a negative $\mathbf{B}_z(t)$. At later times, the measured magnetic field undergoes a polarity reversal exhibiting a positive

$\mathbf{B}_z(t)$. The time $\tau$ at which $\mathbf{B}_z(t) = 0$ is known as the magnetic zero-crossing time, and it occurs when the eddy currents locus of maximum intensity is roughly below the receiver (Nabighian, 1979; Hoversten & Morrison, 1982; Everett & Meju, 2005; Weiss & Everett, 2007). Although the magnetic zero-crossing time occurs before the eddy current maximum is directly below the RX (Hoversten & Morrison, 1982), magnetic zero-crossing time is an identifiable quantity that can be used as a proxy for the eddy current moveout time (Weiss & Everett, 2007).

## 2.4 Characteristic TDEM Earth Responses

### *2.4.1 $\partial t\mathbf{B}_z$ vs. time for a half-space and layered Earth*

We know that in a quasi-stationary, non-magnetic region that the locus of maximum current at a fixed time diffuses to a depth of $d = \sqrt{2t/\mu_0\sigma}$, at a velocity of $v = 1/\sqrt{2\sigma\mu_0 t}$, as a function of the subsurface conductivity $\sigma$. From these relationships we can infer that as conductivity increases, the velocity and depths to which eddy currents diffuse for a given time decreases. An example of this eddy current behavior can be see in the comparison of the central loop responses (TX radius = 20 m) for a conductive half-space, a resistive half-space, a 25 m thick conductive layer over resistive half-space, and 25 m thick resistive layer over a conductive half-space (figure 2.2). Note that the conductivity values used for the conductors and resistors are $\sigma$ = 0.1 S/m and $\sigma$ = 0.001 S/m, respectively. As shown, when a resistor is present the initial amplitude of the measured response is large with the field intensity decaying rapidly. Conversely, when a conductor is present, the initial amplitude of the measured response is smaller than observed in a resistor and the field decays much slower, validating our previous assumption on diffusion velocity. For the layered Earth models, the early response is entirely due to the overburden's conductivity. At later times, dissipation is controlled by the half-space conductivity, decreasing/increasing until the late stage response ($t^{-5/2}$) for the half-space is achieved. An example of a measured response for multiple loop-loop sounding with varying offsets is shown in figure 2.3. For a uniform conductive half-space ($\sigma$ = 0.1 S/m) with a fixed conductivity, we observe that $\tau$ increases as a function of L and can lead to a direct measurement of the diffusion velocity of the eddy currents.

*2.4.2 Zero – Crossing Moveout (ZCMO) for a half-space and layered Earth*

As previously disscused, the time derivative of the vertical magnetic field, $\partial t\mathbf{B}_z$, undergoes a sign reversal as the induced eddy currents diffuse down and outward, roughly when the eddy currents are below the RX. In classical eddy current diffusion, the zero crossing time scales with the squared of the offsets, $\tau \propto L^2$, resulting in a linear relationship with slope $\beta = 1$. A linear ZCMO with $\beta \neq 1$ however cannot be explained by classical diffusion but, rather by the anomalous diffusion of EM eddy currents in a 1D stationary fractal medium which exhibits a $\tau \propto L^{2/\alpha}$ scaling behavior where $0 < \alpha < 1$ (Weiss and Everett, 2007). A previous study conducted in the Brazos River floodplain done by Weiss and Everett (2007) shows an example of anomalous eddy current behavior, specifically, sub diffusion, in which the ZCMO displayed a slope of $\beta = 1.204$ and $\beta = 1.263$. In contrast to linear moveout behavior, nonlinear eddy current moveout behavior cannot be explained by either classical or anomalous diffusion, but rather is representative of a medium with laterally or vertically varying conductivity. ZCMO curves for a 1D layered earth model of variable thickness over uniform half-space are shown in figure 2.4 and 2.5 for two cases: a conductor over a resistive half-space (figure 2.4) and a resistor over a conductive half-space (figure 2.5). In both cases, the conductor value used is 0.1 S/m and the resistor value used is 0.001 S/m (represented by the black curves in each figures), and the TX – RX offset distances range from 30 m to 300 m. For the conductor over resistor model, at relatively small layer thicknesses, the moveout response is dominated by the resistive half-space with a delay in zero-crossing time proportional to the thickness of the overlying conductor. As the conductive layer's thickness increases, the response becomes increasingly representative of the conductor at short offsets with the resistive layer manifesting itself at far offsets. For the resistor over conductive half-space model, a response pattern similar to that seen in figure 2.4 is observed however with a far more pronounced effect resulting from the layer transition. Recall that eddy currents diffuse faster with decreasing resistivity; therefore, for layer thickness < 15 m, the presence of the resistive layer is minimal as the eddy currents diffuse rapidly through the thin layer. At larger thicknesses, however, a notable transition from classical resistive moveout to classical conductive moveout can be seen. For both cases, the observed ZCMO would eventually return to a classical moveout with $\beta = 1$ if the offsets were allowed to increase indefinitely. Note that with a small offset aperture, non-linear moveout curves may resemble

that of linear anomalous moveout resulting from the limited aperture represented; therefore, careful interpretation of ZCMO results must be made.

*2.4.3 Log-normalized $\partial t\mathbf{B}_z$ pseudo-sections*

Recall that the rate of eddy currents dissipation depends on the conductivity of the medium in which the currents flow, decaying more rapidly as conductivity increases. Hence, variations in the observed $\partial t\mathbf{B}_z$ along a profile can serve as possible indicators of changes in lateral and vertical electrical structure. Log-normalized $\partial t\mathbf{B}_z$ pseudo-sections, which display the lateral variations in common-offset responses through contouring, have been previously used for normalized common-offset profiles of multi-transient electromagnetic data over a gas reservoir (Ziolkowski et al., 2007). Results from synthetic log-normalized $\partial t\mathbf{B}_z$ pseudo-sections involving 3-layer sinkhole example (figure 2.6), chosen to reflect the general electrical structure observed at Kentland Farm, for TX – RX separations of 40 m, 60 m, 80 m, and 100 m are shown in figure 2.7a-d. In the model, a semi-resistive, 1m thick top layer ($\sigma$ = 0.002 S/m) overlies a variably thick conductive unit ($\sigma$ = 0.02 S/m) which caps a highly resistive bedrock ($\sigma$ = 0.0002 S/m). The thickness of the clay unit varies depending on position, from 5 m on the outside of the sinkhole to 10 m at the center of the sinkhole. Because the contours represent changes in normalized $\partial t\mathbf{B}_z$ as a function of time over a profile, as the medium's conductivity increases, eddy current dissipation rate decreases resulting in thicker contours intervals for increasingly more conductive environments. As you can see, the increasingly conductive sinkhole is observed on all four plots reaffirming the ability of log-normalized $\partial t\mathbf{B}_z$ pseudo-sections to detect lateral changes in electrical structure. Additionally, the degree in which the sinkhole was detected varied depending on the TX – RX separation distance, becoming increasingly more pronounced with increasing separation. We can therefore conclude that with increasing offset, structures at deeper depths can be resolved.

**2.5 Description of the PROTEM 47D System**

In this study, we employ a Geonics Ltd. PROTEM 47 TDEM soundings system (www.geonics.com). Because of the variable target depth (estimated to be greater then 10 m and

less then 70 m) and presence of clay, the survey parameters were chosen to encompass a wide range of Earth models within our novel multi-fold experiment design. The manufacturers recommended TX – RX configuration for a profiling survey is shown in figure 2.8 with a flexible 8-turn TX loop being connected to a 3-component air cored multi-turn RX coil by reference cable. A half duty cycle square wave source current is passed through the TX loop at a repetition rate (frequency) defined by the user (figure 2.9a). The effects of different survey characteristics of the TX loop such as size and current magnitude will be discussed in the following chapter. The current is abruptly terminated and the current and resultant primary magnetic field returns to zero in a specified time interval known as the ramp time (McNeill, 1980). The reduction in current, according to Faraday's law, induces an emf (figure 2.9b), whose magnitude is proportional to the change in primary magnetic field (i.e. slope of the ramp), which generates its own secondary magnetic field as previously discussed. The time derivative of the secondary magnetic field (Figure 1c) is then sampled as a voltage at a series of logarithmically spaced time intervals or "gates" by a multi-turn receiver coil. In using the step off response, measurement of the weaker secondary magnetic field can be made in the absence of the stronger primary magnetic field. Notice in figure 1c that the measured voltage decays much faster at early times; hence, early gates are narrower then later gates where the decay is more gradual in order to reduce the distortion on early measurements (McNeill, 1994). The PROTEM 47D has two gate settings, 20 and 30 gate mode respectively, the choice of which to use is dependent on the target of interest. The 20 gate mode has narrower gates, which samples the decaying magnetic field more frequently at earlier times than the 30 gate mode, lending it self to environments in which characterization of the early response is the primary goal. In the 30 gate mode, measurements are made with larger time spacings that extend an order of magnitude further in time (20 gate mode $t_{max}$ = ~600 $\mu s$ and 30 gate mode $t_{max}$ = ~6000 $\mu s$), making it ideal for exploration in relatively uncharacterized settings. Additional means of signal amplification such as gain settings, in situ processing, and stacking increase the signal to noise ratio and will be described in further detail in the following chapter.

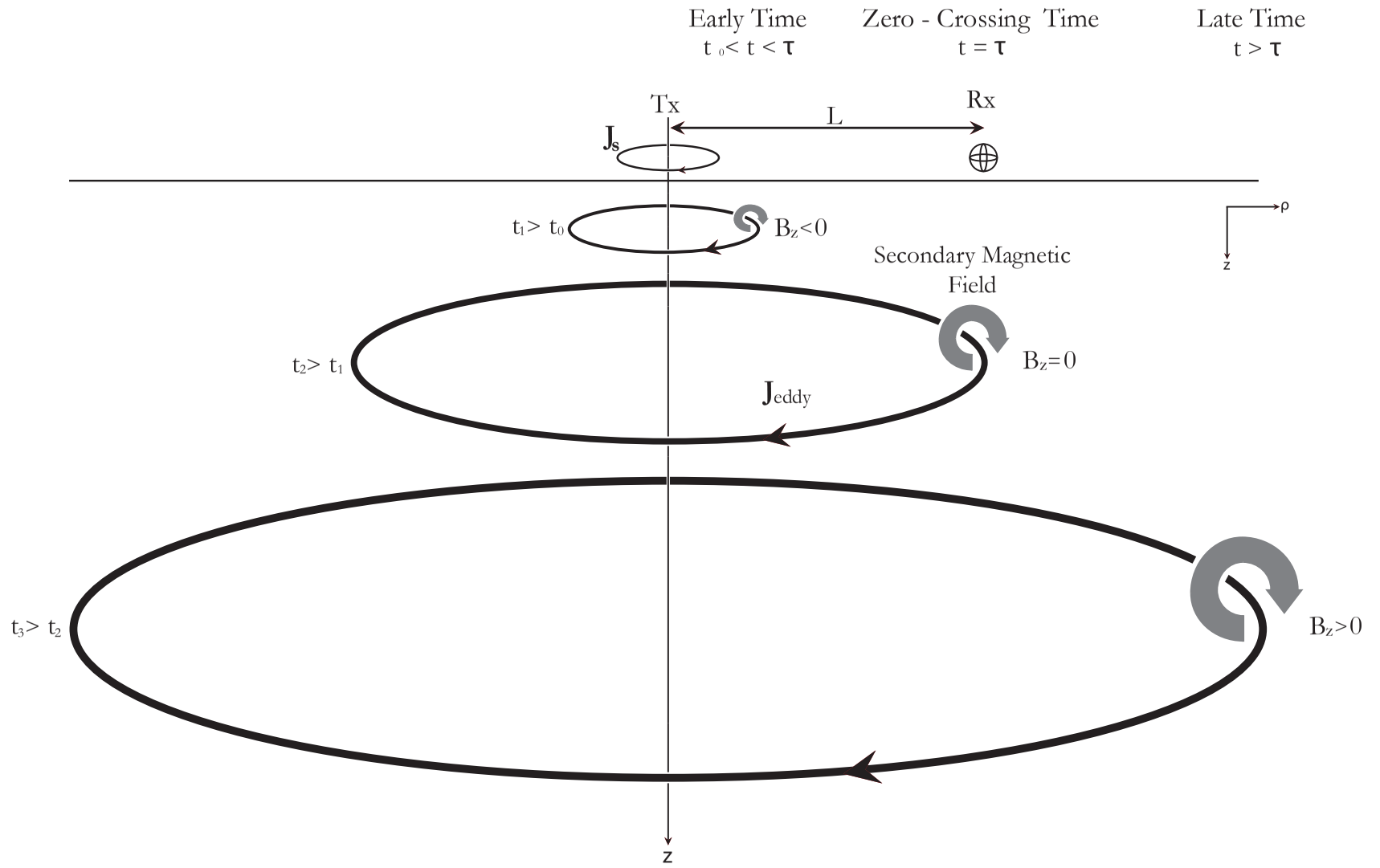


**Figure 2.1.** A diagram of eddy current moveout behavior for offset soundings. A step off source current induces eddy currents that mimic the shape of the transmitter which generate their own secondary magnetic field causing a down and outward diffusive propagation in the ρ and z directions. At early times the **B**(t) is negative while at late times the vertical magnetic **B**(t) is positive. Roughly at distance L, TX-RX offset, **B**(t) is zero. The time that corresponds to the polarity reversal is the zero-crossing time.

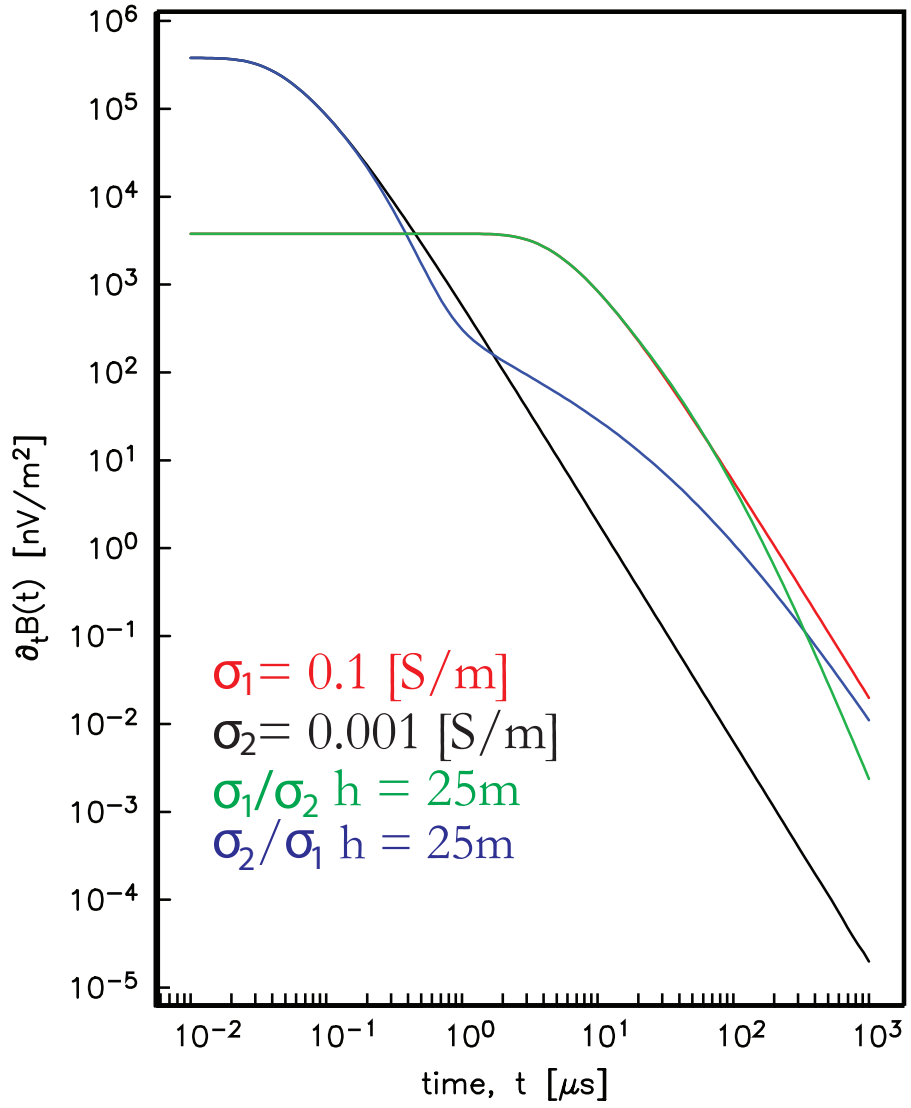


**Figure 2.2.** The theoretical central loop response is shown for the four cases: conductive half-space (red), resistive half-space (black), a 25 m thick resistive layer over conductive half-space (blue), and a 25 m thick conductive layer over resistive half-space (green).

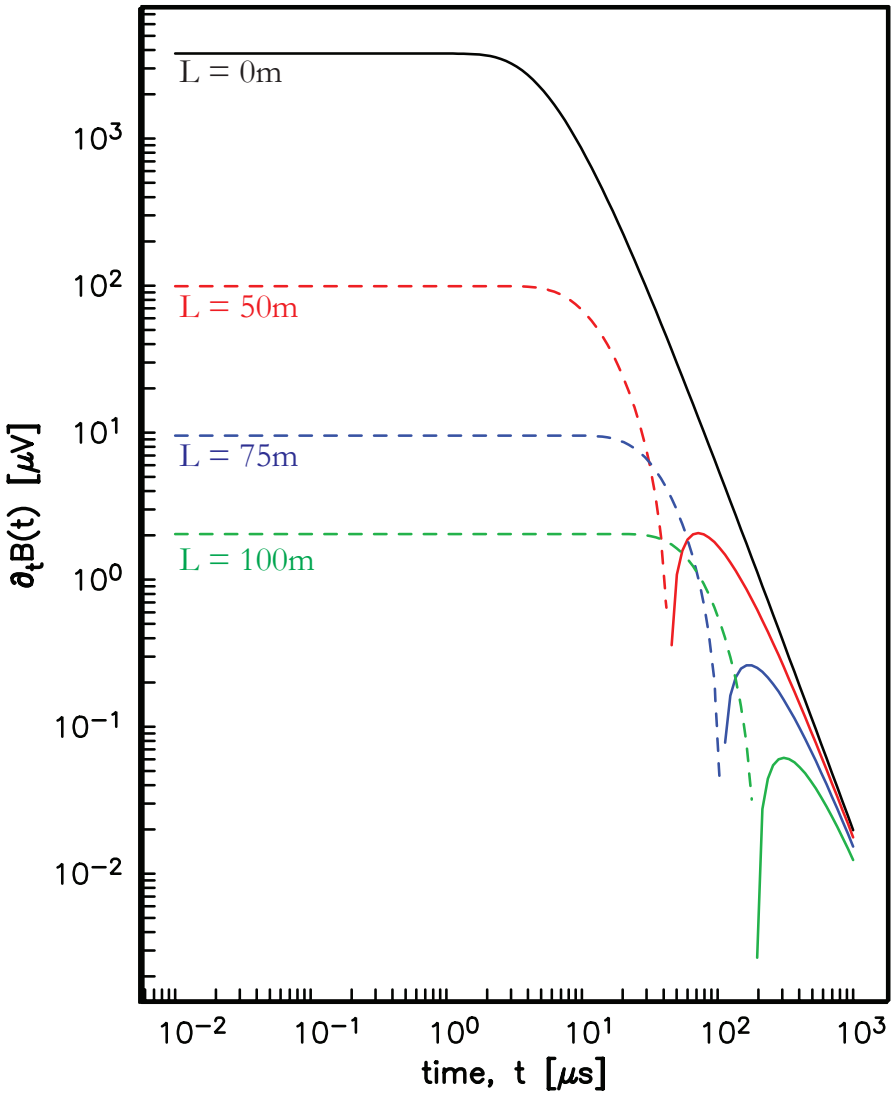


**Figure 2.3.** The theoretical transient response for a conductive uniform half-space ($\sigma$ = 0.1 S/m) for offsets at 0 m (black), 50 m (red), 75 m (blue), and 100 m (green) shows an increase in zero-crossing time with offset (L). The dashed lines represent negative flux values and the solid lines represent positive flux values.

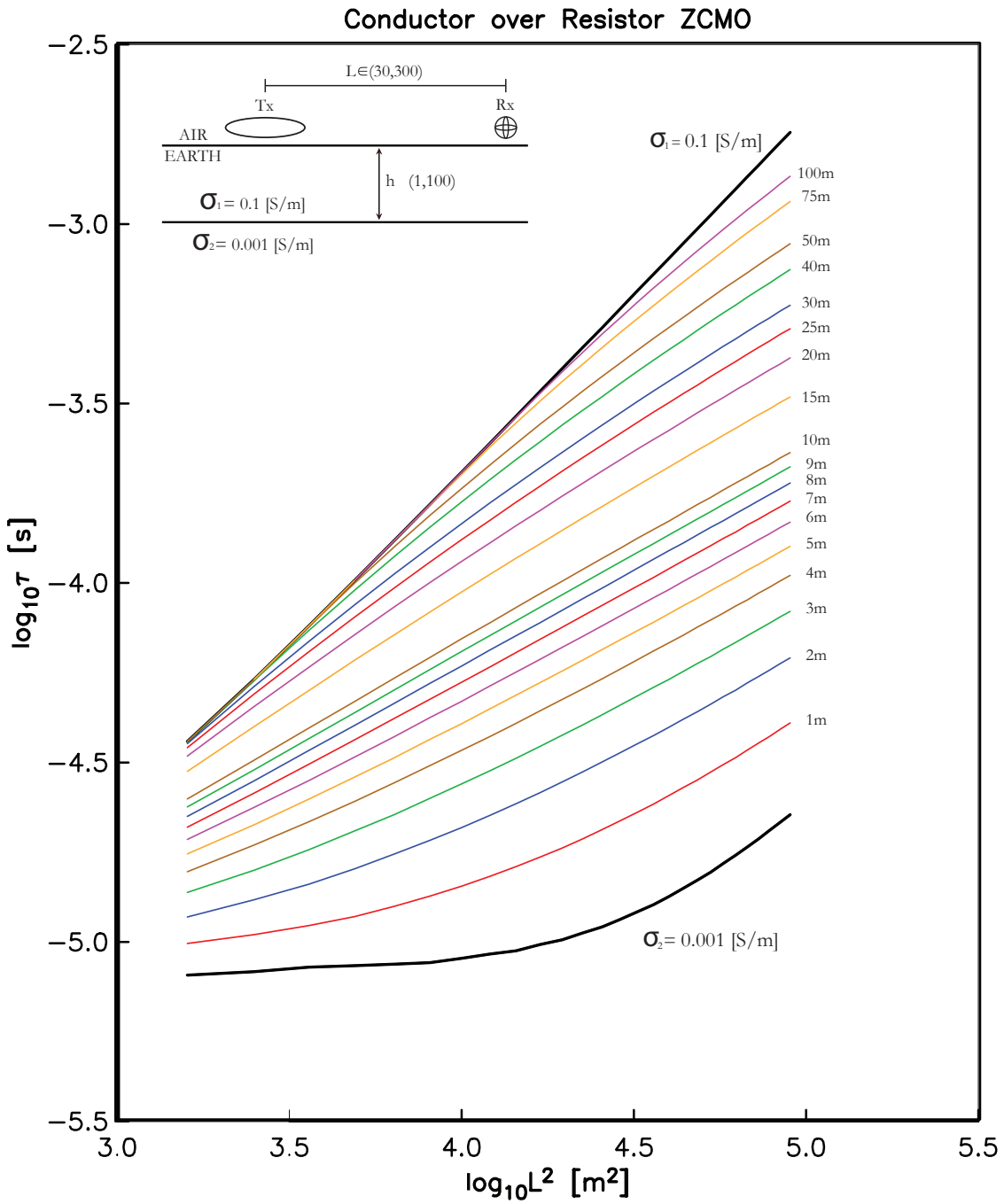


**Figure 2.4.** Theoretical ZCMO curves for a resistive half-space of σ = 0.001 S/m (lower black line), conductive half-space of σ = 0.1 S/m (upper black line), and a conductor layer over a resistive half-space for variable thicknesses as indicated by the labels (colored lines).

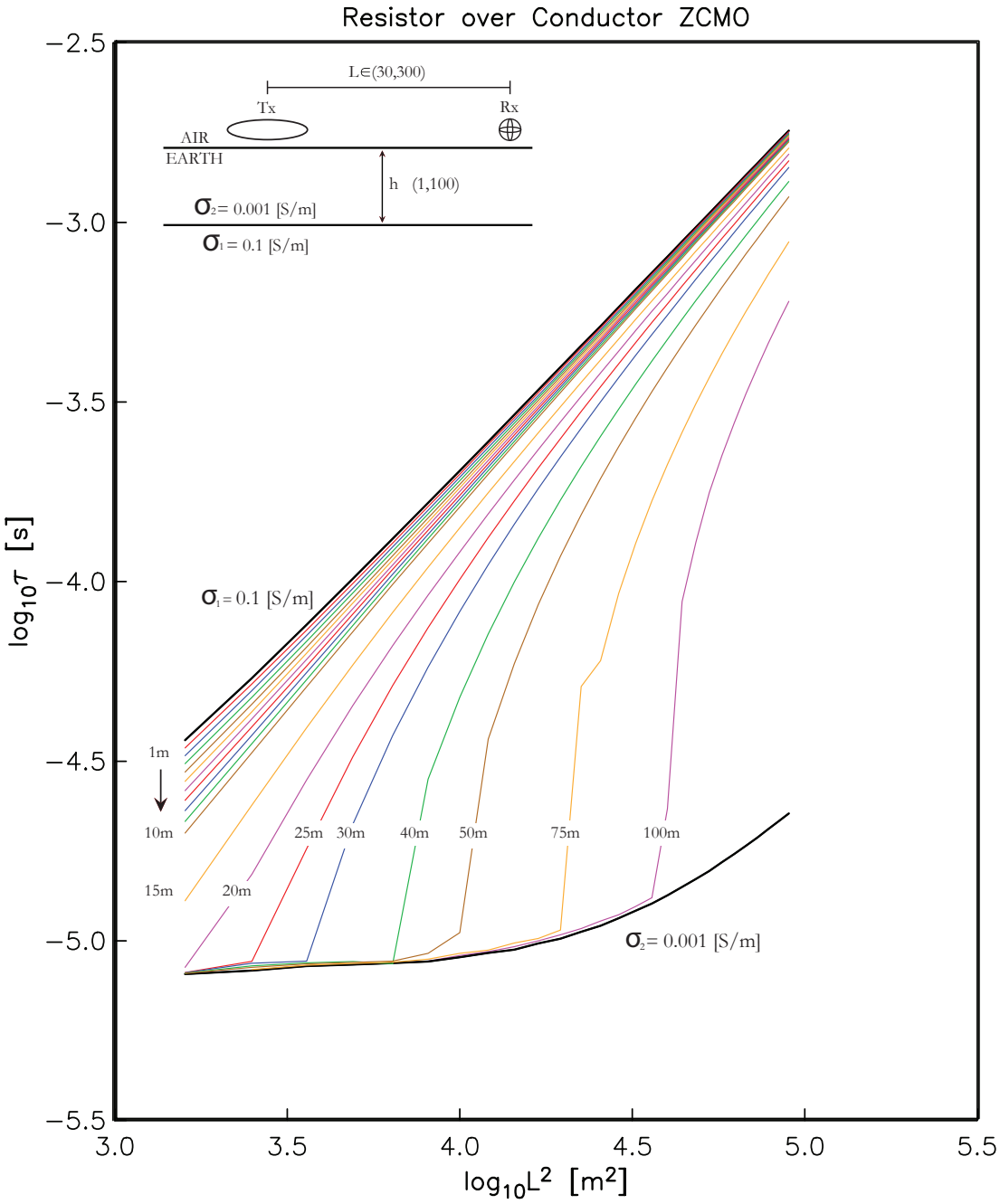


**Figure 2.5.** Theoretical ZCMO curves for a resistive half-space of σ = 0.001 S/m (lower black line), conductive half-space of σ = 0.1 S/m (upper black line), and a resistive layer over a conductive half-space for variable thicknesses as indicated by the labels (colored lines).

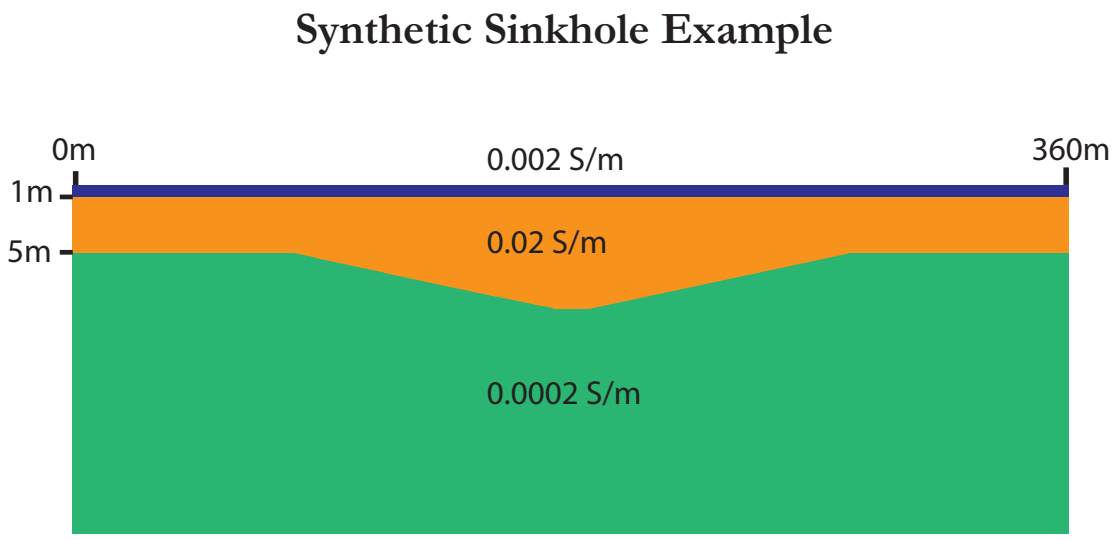


**Figure 2.6.** Diagram of the sinkhole example used in synthetic testing

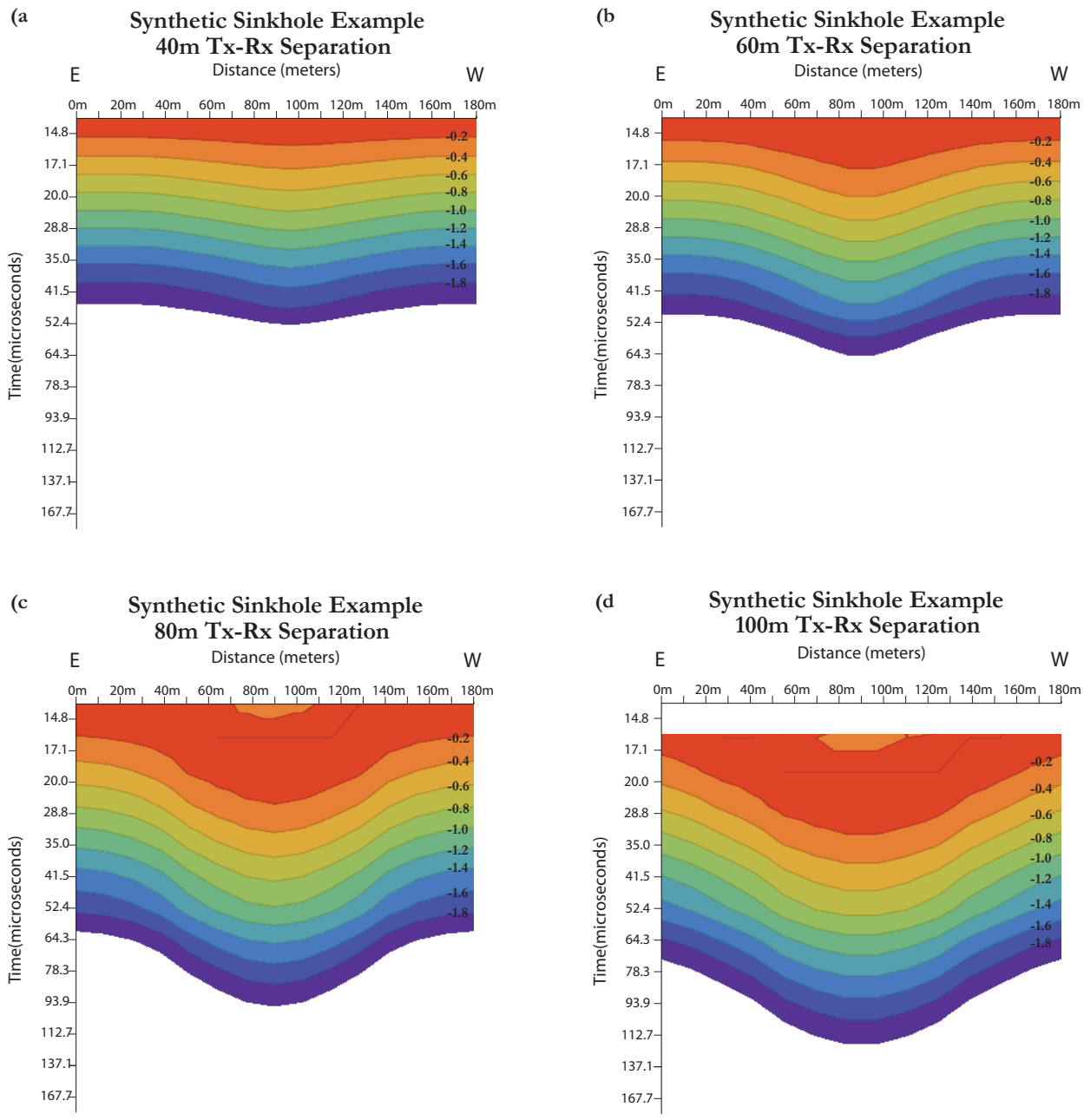


**Figure 2.7a-d.** Synthetic log-normalized $\partial t\mathbf{B}_z$ pseudo-sections for TX – RX separations of 40 m (a), 60 m (b), 80 m (c), and 100 m (d). The horizontal axis represents the distance along the traverse and the y axis represents the first 13 time gates chosen for their reliability above the noise threshold. The color scale represents log-normalized voltages contoured ranging from 0 to -2, contoured at a -0.2 interval.

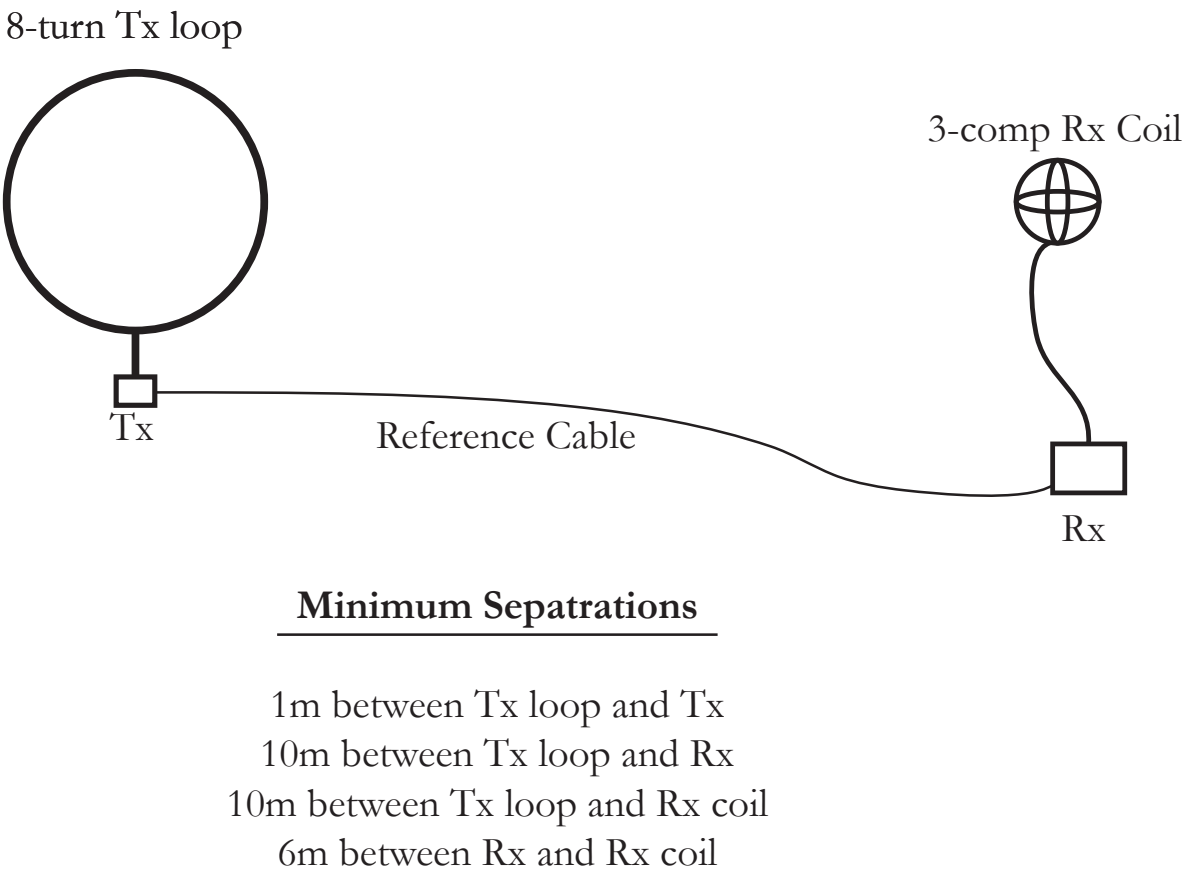


**Figure 2.8.** TX – RX array configuration diagram with the manufacturer's specified minimum separations between the TX loop and TX, TX loop and RX, TX loop and RX coil, and RX and RX coil shown.

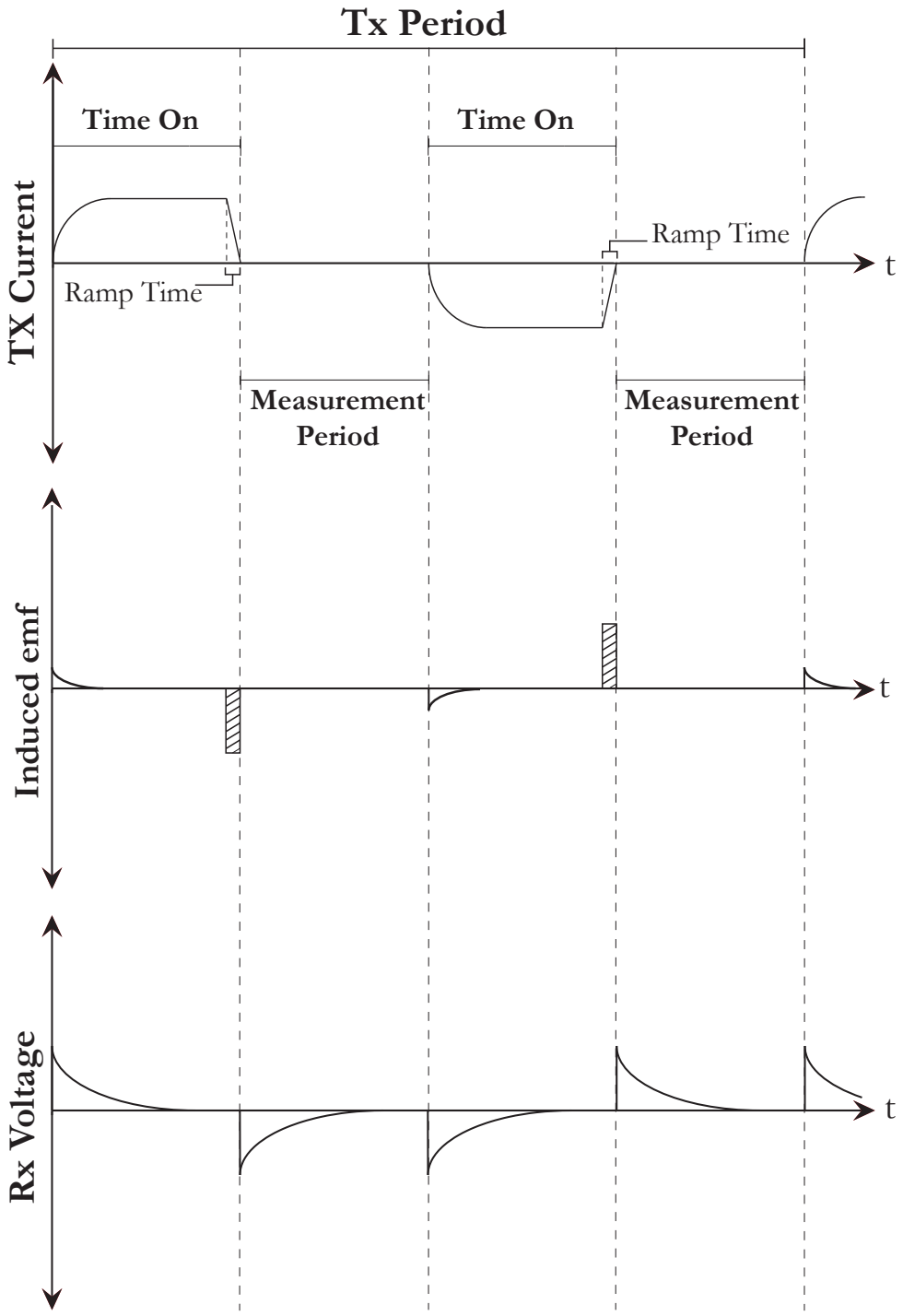


**Figure 2.9a-c.** System waveforms for TX current, induced emf, and RX voltage as a function of time (McNeill, 1980).

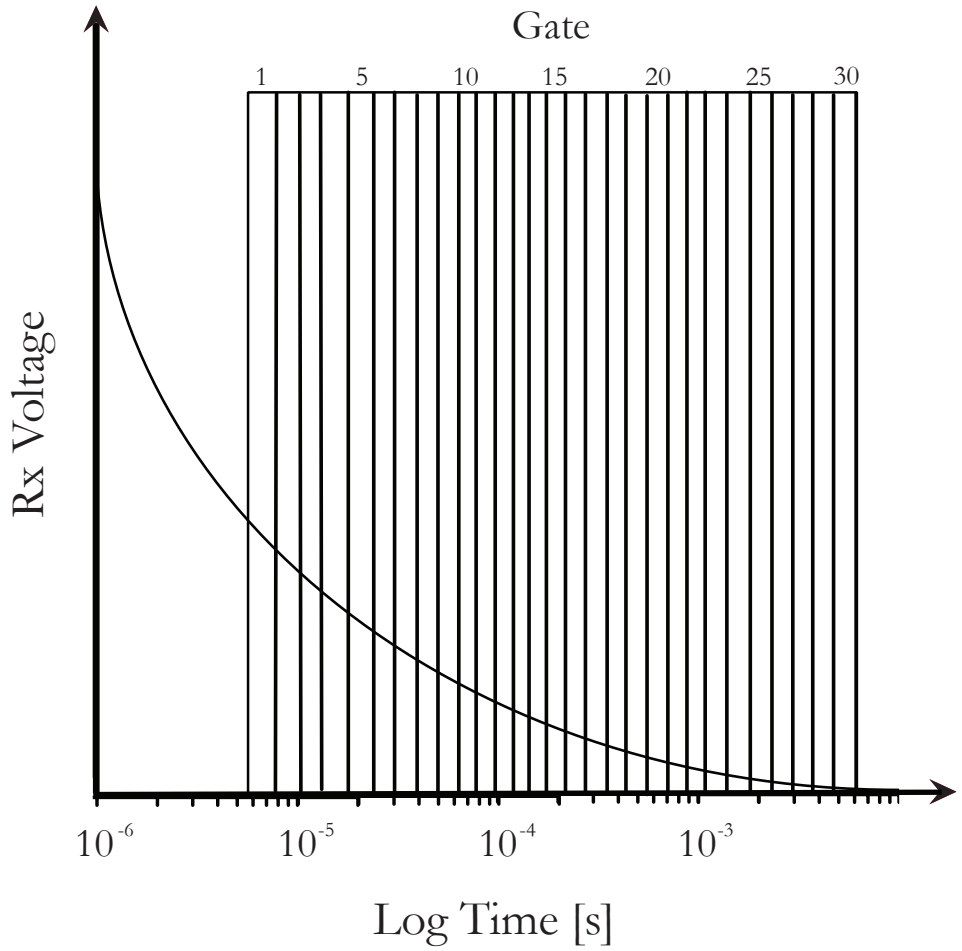


**Figure 2.10.** Schematic for the 30 gate mode showing the RX voltage as a function of log time. The 30 gates are logarithmically spaced resulting in narrower gates early in time where the RX voltage is rapidly changing and large late gates where the Rx voltage has stabilized.

# Chapter 3: Field Observations

## 3.1 Survey Design Detectability

Several considerations need to be made when designing a TDEM survey. First and foremost, an appropriate TX source must be decided upon that is suitable to the target of interest. The depth and resolution of detectable geologic features are dependent on a combination of geologic setting and the survey parameters. Depth of investigation $d$ is proportionally related to the TX moment $m = nIA$ according to :

$$d \approx 0.5\left(\frac{nIA}{\sigma_1 \eta_v}\right)^{1/5} \tag{2.1}$$

where $n$ is the number of turns in the TX loop, $I$ is the TX current, $A$ is the area of the TX, $\sigma_1$ is the overburden conductivity, and $\eta_v$ is the noise threshold that is commonly taken to be 0.5 $nVm^2$ (Spies, 1989). When the electrical conductivity of the underlying medium is held constant, the result of increasing the TX moment is a higher amplitude signal allowing for deep soundings. An increase in $m$ can be achieved one of three ways: By increasing the area of the TX, by increasing the current input, or by using a multi-turn TX. The use of larger TXs increases the depth of exploration capability, however it also consequently decreases resolution in the near surface. Hence, careful consideration of the target depth and/or size must be made. The RXs used in transient soundings range from large loops of comparable TX size to small induction coils; although, the use of modern multi-turn ferrite or air cored induction coils is common practice. The magnetic field component measured is dependent on the TX – RX geometry. For horizontally lain TXs, horizontal coplanar geometries (Figure 3.1a) measure the vertical magnetic field component, perpendicular geometries measure the radial component (Figure 3.1b), and null geometries measure azimuthal magnetic field component (Figure 3.1c). Although traditionally only the vertical magnetic field is used in interpretation there are several benefits in three component measurements. Horizontal field components have been used previously for improvement of the S/N ratio to predict noise in the vertical components (Spies, 1988) as well as in testing for lateral heterogeneities and anisotropy (Weiss & Everett, 2007). But most importantly, a 3D Earth generates a three-component response.

It is widely accepted that the depth of exploration is increased with increasing the offset (Collins et al., 2006). In figure 3.2 and figure 3.3 the transient response for a conductor over resister layered earth model with variable height (1m to 150 m), for a 50 m and a 100 m offset, respectively, are shown. Although the forward solutions are noise free, the noise threshold of 10 $nV/m^2$ used in this study is represented by the dashed line. Early and late time responses for soundings for each offset can be resolved sufficiently above the noise threshold; however, distinct advantages can be recognized in both. For the shorter 50 m offset soundings (Figure 3.2), the $\partial t\mathbf{B}_z$ polarity reversal (zero-crossing time), as expected, occurs earlier than for the larger 100 m offset (Figure 3.3). Increasing the overburden thickness requires eddy currents to diffuse longer through the electrically slower conductive layer. We know that the zero-crossing time ($\tau$) increases proportionally with loop separation, $L$; therefore, at larger offsets, the diffusion characteristics of the eddy currents at early times can be analyzed. For a 100 m loop separation (Figure 3.3), the difference in zero-crossing time between the first observable $\tau$ at 3m overburden thickness and last observable $\tau$ at a 150 m overburden thickness is approximately 184 $\mu s$. For the 50 m loop separation the zero-crossing time difference between the first and last measurable $\tau$ is approximately 39 $\mu s$, more than 4 times less than for the 100 m loop separation. This observational result implies that variations in overburden thickness are better resolved by measurements made at larger offsets.

Diffusion of the induced eddy currents in the underlying medium is heavily dependent on the electrical conductivity structure of that medium. Although electrical variations in both vertical and horizontal directions affect the measured response, the degree to which each component affects the response is not easily distinguishable. As illustrated in figure 3.4, regions bounded by eddy current diffusion are highly sensitive to vertical variations below the TX. This sensitivity decreases with the decaying field intensity but also widens laterally with the outward diffusion of the eddy currents. However, the question of how loop separations affects measurement sensitivity still remains. From the theorem of reciprocity we know that the TX and RX are interchangeable, as both are equally represented in the measured response. If we substitute the RX with an auxiliary TX it is easy to see that in addition to high sensitivity below the two loops, there is an area of intermediate sensitivity laterally as the diffusing eddy currents constructively interfere with each other (Figure 5b). Hördt (1998) verifies this principle by convolving the electrical field response for two offset TX's in the time domain. This

intermediate sensitivity to lateral variations seen in separate loop methods increases the ability to detect vertical conductive features such as fracture zones and dikes.

### 3.2 Noise Testing

In a perfect world, lack of noise renders limitless resolution depth. In practice, however, errors created from the presence of noise are inevitable when conducting a TDEM survey. Recognizing and taking proper action in dealing these noise related errors is essential for any successful survey. Noise can be divided into two main categories: Incoherent noise (natural/man-made); and, coherent noise (geometric, cultural, and geologic) (Everett & Meju, 2005). Incoherent environmental or electromagnetic noise is classified as any detected electrical or magnetic signal that interferes with a given measurement and includes both natural sources (geomagnetic, sferics) and man-made sources (power-lines, VLF radio). Natural noise sources are random and span a broad range of frequencies including low frequency ($10^{-2}$ – 1 Hz) geomagnetic noise and mid to high frequency (1 – $>10^4$ Hz) spheric noise (Palacky & West, 1991). Geomagnetic noise, mainly result of ionospheric and magnetospheric interactions with solar phenomena, exists at low enough frequencies not to significantly affect the measured response in near-surface applications. Spherics, the result of local and global lightning discharge, on the other hand, are the predominant source of random environmental noise in TDEM exploration and precautions much be taken into account to limit its effect, specifically avoiding surveying during periods of high electrical activity. Man made noise sources like power lines (50/60 Hz) and very low frequency radio transmissions (10 – 25 kHz) are periodic and operate at specific frequencies dependent on the source. Modern EM surveying systems, like the PROTEM47 system used in this survey, can correct for the presence of power lines with a notch filter and by shifting the repetition frequencies far enough way from the power line frequencies and any associated harmonics. Although incoherent noises sources do manifest themselves in TDEM measurements, their effect can be significantly reduced by the stacking of several transients over an integration period, which can be increased in areas of higher noise.

Coherent noise sources are the result of various interactions with the TX source current itself and are much more difficult to compensate for. Geometric effects, including misalignment of the RX, have a negligible effect in the time domain. Because TDEM measurements are taken

in during the TX's off-time, loop separation is not a big factor, however, when profiling careful attention must be made to RX orientations as to assure consistent sampling of the same component (Nabighian & Macnae, 1991). Cultural noise and geologic noise have a their own significant effects on the measured response that are not easily corrected. Cultural noise is the result of the mutual induction between the TX current and nearby man-made metallic objects such as pipes, fences, etc. As mentioned in section 1.4, the Kentland Farm field site is a cow pasture enclosed by an electric fence. The fence itself consisted of three electric wires with wooden posts, which should have a generally small effect (Spies & Frishknecht, 1991); however, testing for the presence of the electric fence was done at a nearby site to verify this. To test for the effect of an active and inactive electric fence, a series of 50 m offset loop measurements were conducted (Figure 3.5). Beginning with the electric fence on, measurements were made starting at 80 m offset from the fence and decreasing at 10 m intervals until the final distance of 20 m was reached. The electric fence was then turned off and the same series measurements were carried out again. A comparison between response for the electric fence being off and on for identical fence offsets are shown in Figure 3.6a-g. As we can see, there is virtually no early time noise difference between the two responses, with only subtle variations being observed near the noise threshold ($\eta_v = 10^{-8}$ V/m$^2$). Subtle variations in measurements at later gate times could be geologically or geometrically induced variations as the result of minor changes in TX loop positions between on and off measurements. In addition, very little effect from the fence itself with increasing proximity was observed in both cases where the electric fence was off (Figure 3.7a) and on (Figure 3.7b).

Geologic noise is the result of small-scale heterogeneities that distort the transient response making it difficult to fit the response to a 1D earth model. Unlike incoherent noise, geologic noise cannot be simply corrected for by stacking as it arises in the same manner as the target itself (Eaton & Hohmann, 1987). From the observations made in the cultural noise test and the stacking/integration capabilities we expect that 3D geologic complexities anticipated at this field site will be the primary contributor to the observed noise levels. To counteract the effect of geologic noise, various gain levels will be employed to maximize signal amplitude while maintaining a noise threshold of $10^{-8}$ V/m$^2$.

### 3.3 Data Collection

Surveying on the 40 m terrace at Kentland Farm, VA was conducted during a three-week span in the month of April 2009 with the Geonics PROTEM 47D unit (www.geonics.com). The requirement for array mobility led to the use a flexible 8-turn TX loop with ~ 1 amp current and a 3-component air cored multi-turn RX coil. The TX and RX were initially set according to the manufacturer's recommendation for a profiling configuration with the TX being initially set 10 m away from the TX. After array set-up was complete, fixed TX roving RX profiling was carried out for 18 TX positions along the 180 m transverse (figure 3.8). Refer to section 1.3 on Multi-fold TDEM Offset Profiling for a full description of the novel profiling technique employed.

A source current was passed through the TX loop at repetition rate of 30 Hz and the transient response was measured at a series of 30 logarithmically spaced time gates (30 gate mode) ranging from a $6.8\,\mu s$ center time at the first gate to $6134\,\mu s$ center time at the last gate. The first measurement time is shifted from end of the ramp by $6.8\,\mu s$ because it may take additional time after the ramp ends for the TX current to stabilize to zero. The 30 Hz repetition rate chosen as it was the highest available for the 30 gate mode allowing for the earliest time measurements. By comparison, the next highest repetition rate was 7.5 Hz with a first gate center time of $36\,\mu s$. A 30 second integration time was chosen because by then all of the data above the noise threshold had stabilized to a single value. After all three components were measured at a given RX position, the RX was moved to the next location and the measurement procedure was repeated. A sample of the data for all three components collected at the 130 m TX position with a 60 m offset is shown in Figure 3.9a-c. In the z-component sounding (Figure 3.9a), a very good S/N ratio was achieved with a gain of 5, with 12-13 usable measurements above the noise threshold. Although the noise threshold observed in the vertical component is fairly low, the azimuthal component (Figure 3.11c) and radial component (Figure 3.9b) have much higher noise thresholds, which is indicative of geologic noise from a largely laterally heterogeneous medium. The noise levels observed here are fairly representative of the observed noise levels for the entirety of the survey. Valuable first order interpretations can be made with initial observations of the $\partial t\mathbf{B}_z$ response. First, the zero-crossing time appears between the 2nd and 3rd gate ($9.1\,\mu s$ – $12.0\,\mu s$) indicative of a conductive medium at 60 m offsets. Secondly, the

transient's rapid decay represents a resistive environment. By marrying these first two observations, considering what we have seen before from prior two-layered models (see figure 3.2 and 3.3), we can conclude that our initial interpretation is that of a conductor over resistor.

To lend context to the transient response of the 40 m terrace, an additional ZCMO profile located on the 20 m terrace adjacent to the well-characterized, field location of sinkhole #5 (Schwartz et al, 2008) was acquired. The ZCMO survey was carried out in early June 2010 and consisted of a 200m line with RX measurement intervals of 3 m. With an anticipated overburden thickness of ≈ 5-7 m, the 20 gate mode was used with a repetition rate of 285 Hz and a TX current of 1.5 A generating a TX moment of ≈ 600. A sample transient for a 62 m TX – RX separation is shown in figure 3.10. The noise level is far lower than the previously defined noise threshold ($10^{-8}$ V/m$^2$). The observed zero-crossing seen between the gates 1 and 2 ($6.8\,\mu s$ – $8.9\,\mu s$) occurs earlier than the zero-crossing at a similar 60 m TX-RX separation on the 40 m terrace (figure 3.9a). This suggests that the 20 m terrace is a "generally" a more resistive environment, which is characteristic of transients for shallower bedrock depths as shown in conductor over resistor models (figure 3.2). It is important to recognize that this initial interpretation is just that, and further analysis will be the needed to further understand the electrical structure on the 40 m terrace.

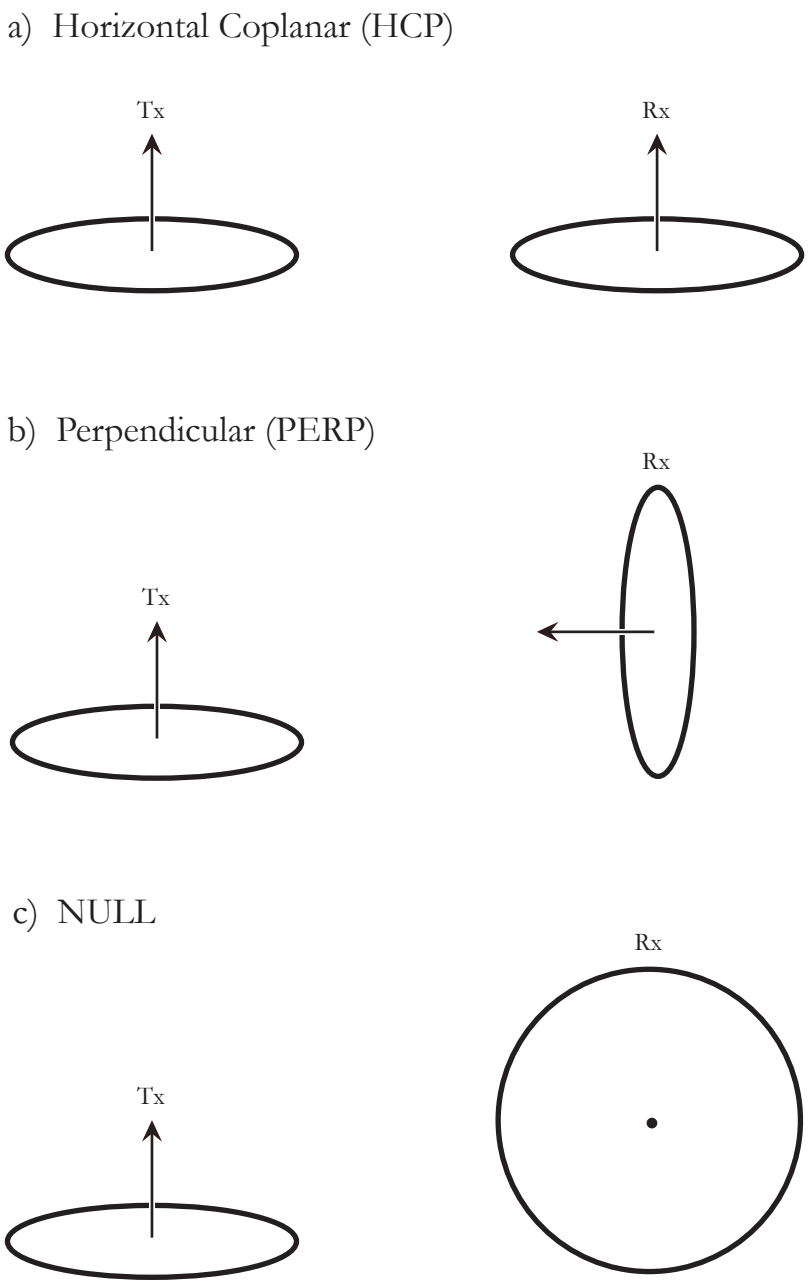


**Figure 3.1.** A diagram demonstrating a) horizontal coplanar, b) perpendicular, and c) null TX – RX geometries.

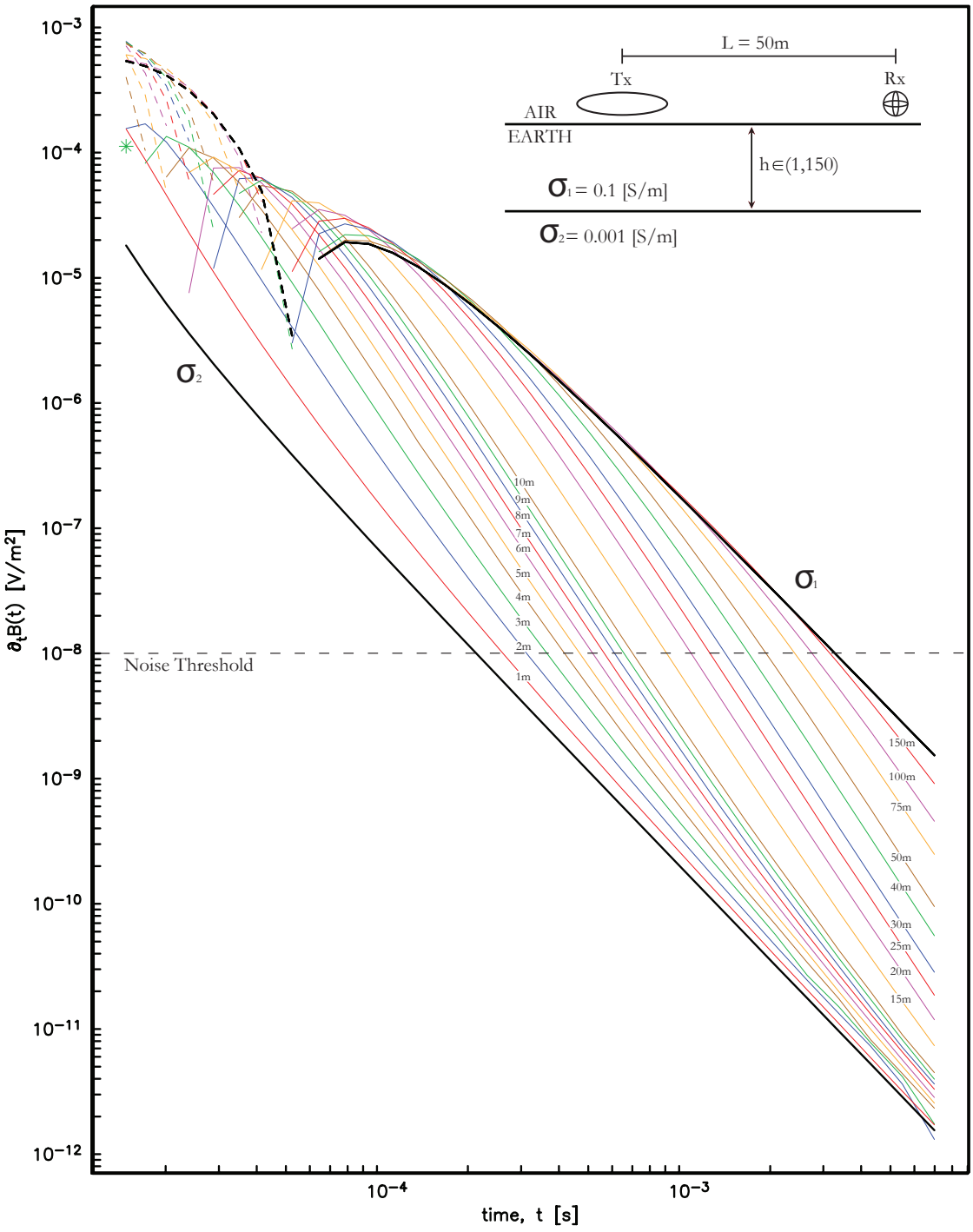


**Figure 3.2.** Theoretical 50 m offset sounding curves for a conductive half-space $\sigma_1$ = 0.1 S/m (upper black curve), resistive half-space $\sigma_2$ = 0.001 S/m (lower black curve), and conductor over a resistor $\sigma_1/\sigma_2$ (colored curves) for variable layer thicknesses ranging from 1m to 150 m as indicated by the labels. The dashed line represents the noise threshold of $10^{-8}$ V/m$^2$ used in this study

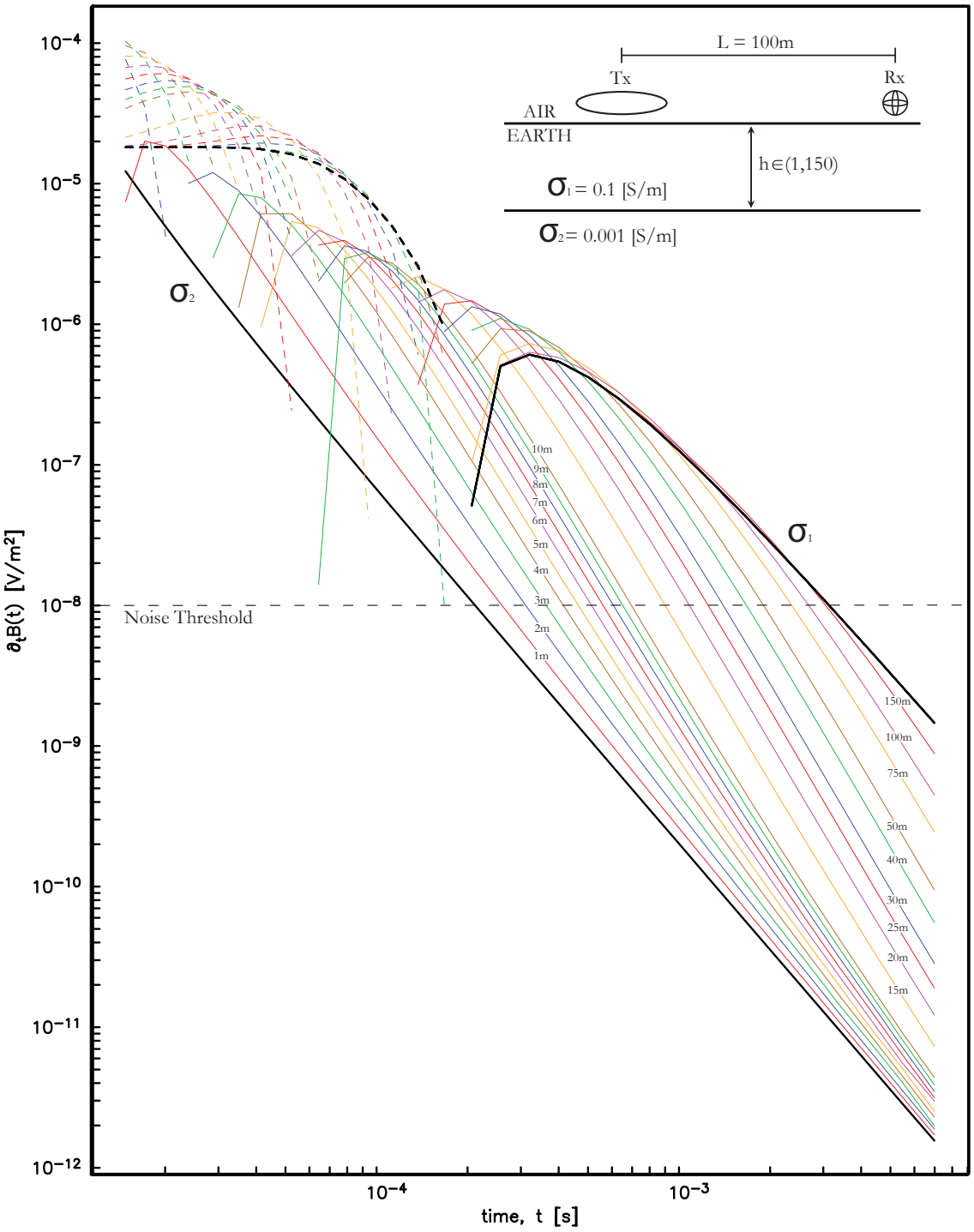


**Figure 3.3.** Theoretical 100 m offset sounding curves for a conductive half-space $\sigma_1$ = 0.1 S/m (upper black curve), resistive half-space $\sigma_2$ = 0.001 S/m (lower black curve), and conductor over a resistor $\sigma_1/\sigma_2$ (colored curves) for variable layer thicknesses ranging from 1m to 150 m as indicated by the labels. The dashed line represents the noise threshold of $10^{-8}$ V/m$^2$ used in this study

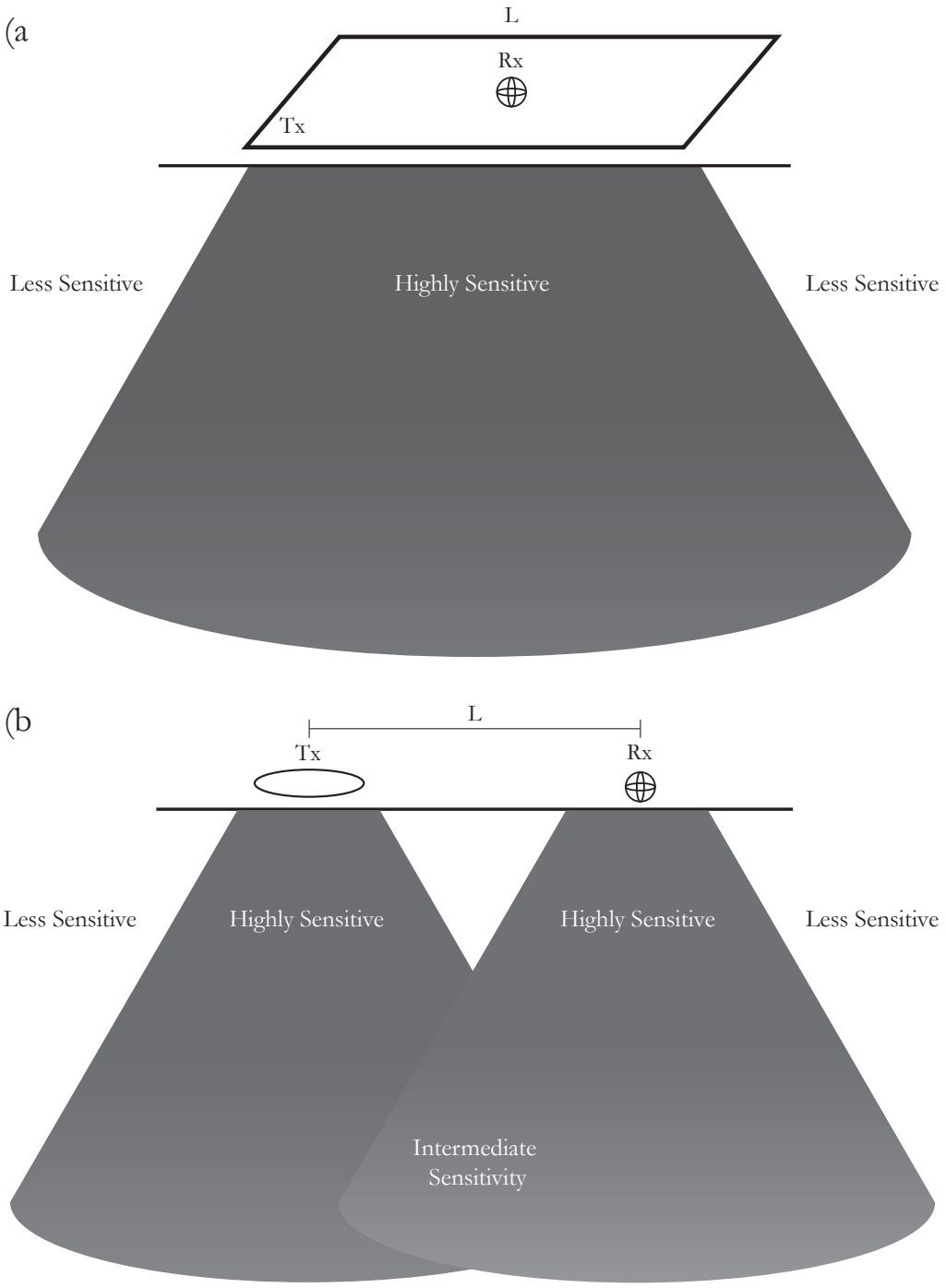


**Figure 3.4.** Diagrams of eddy current sensitivity for central loop soundings (a) and separate loop soundings (b)

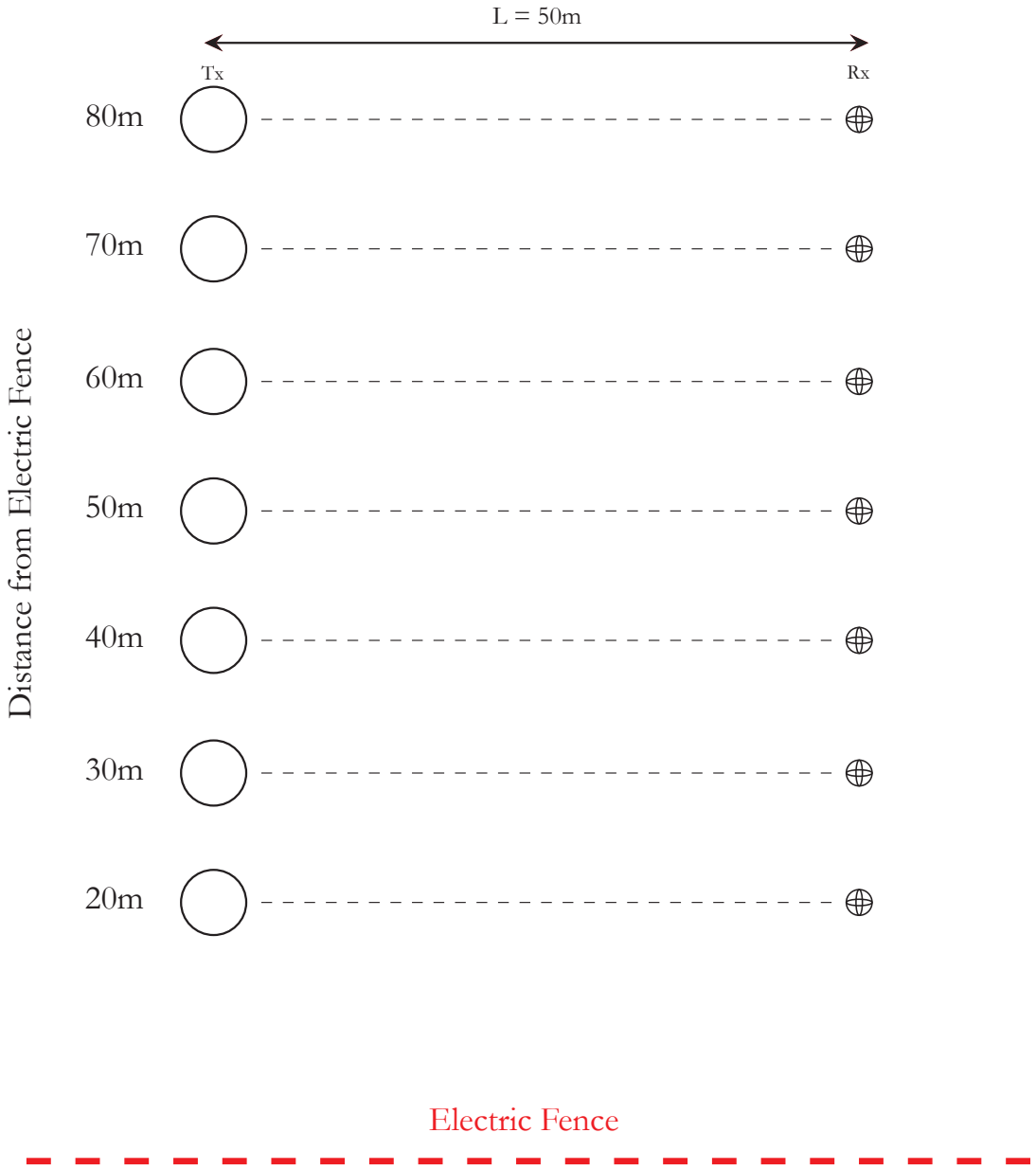


**Figure 3.5.** Electrical fence test configuration

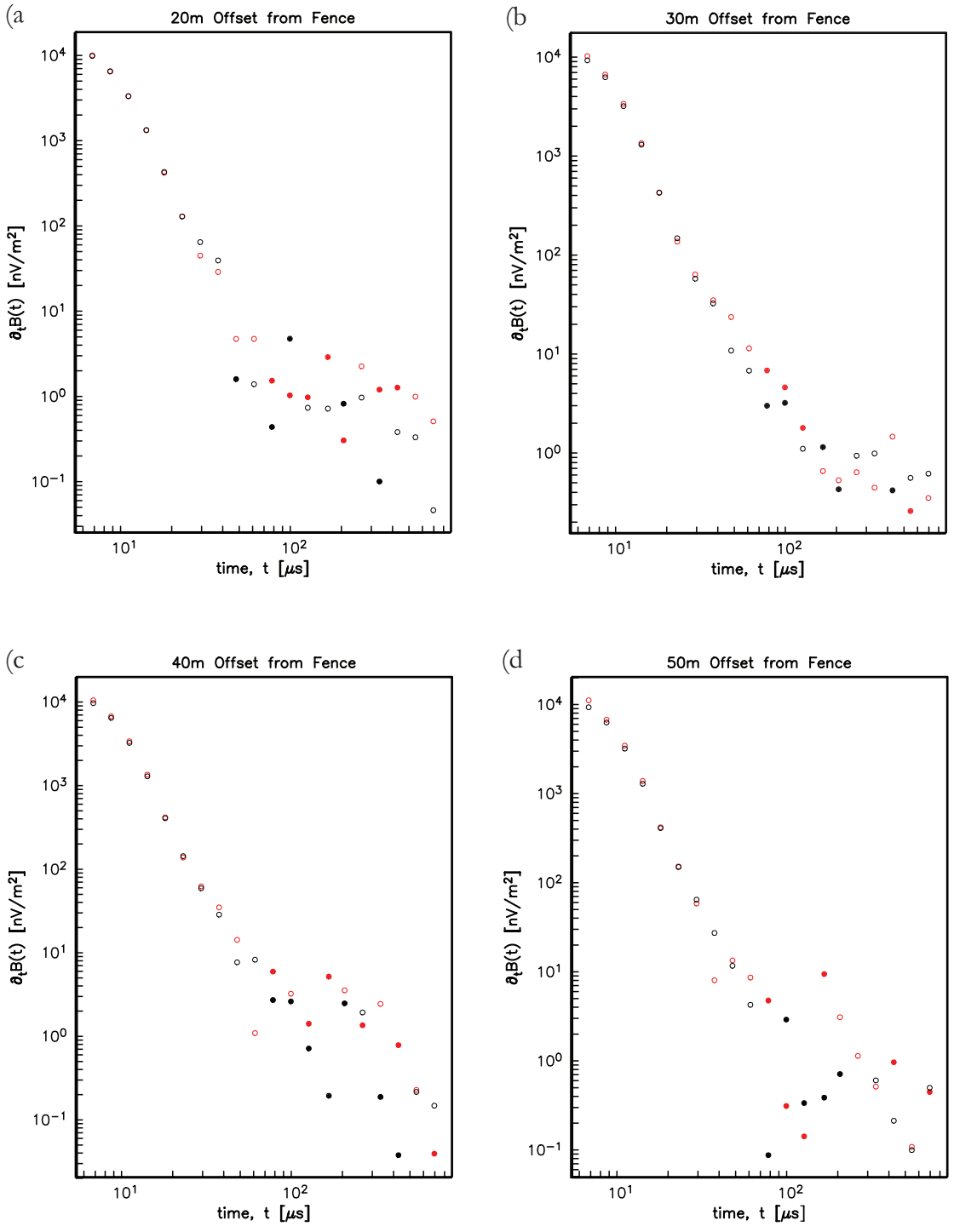


**Figure 3.6a-g.** Electrical fence test results comparing the measured response for 7 fence offset distances (80 m – 20 m) with the electrical fence on (red dots) and the electrical fence off (black dots). Open circles correspond to negative values and closed circles correspond to positive values.

(e

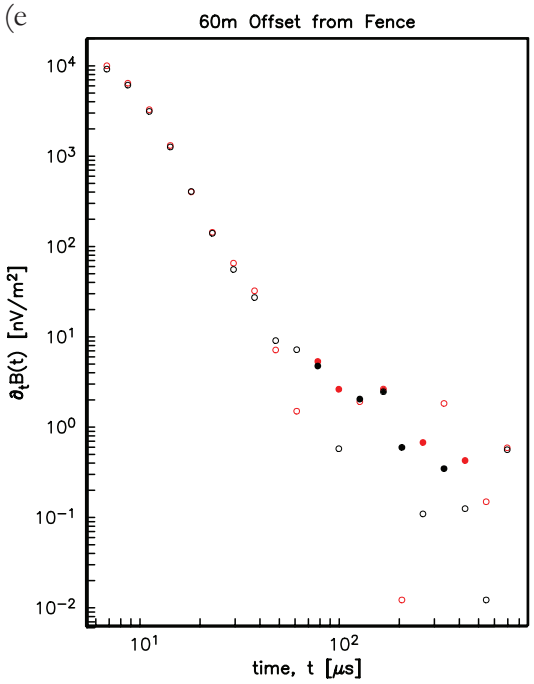
60m Offset from Fence
$\partial_t B(t)$ [nV/m$^2$]
time, t [$\mu$s]

(f

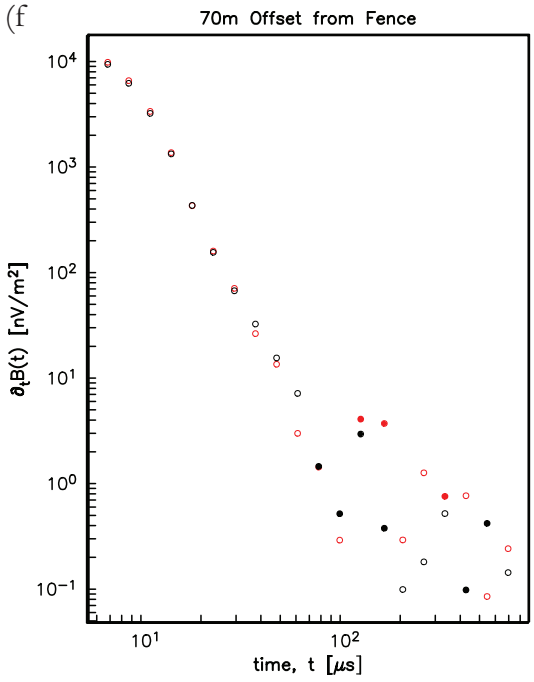
70m Offset from Fence
$\partial_t B(t)$ [nV/m$^2$]
time, t [$\mu$s]

(g

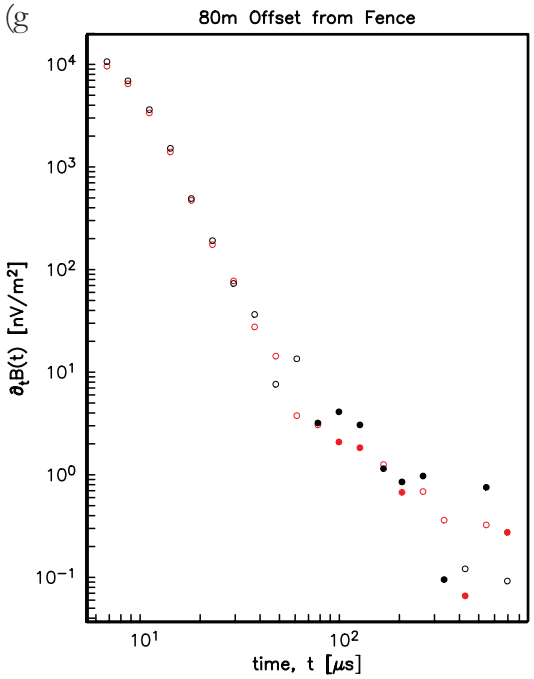
80m Offset from Fence
$\partial_t B(t)$ [nV/m$^2$]
time, t [$\mu$s]

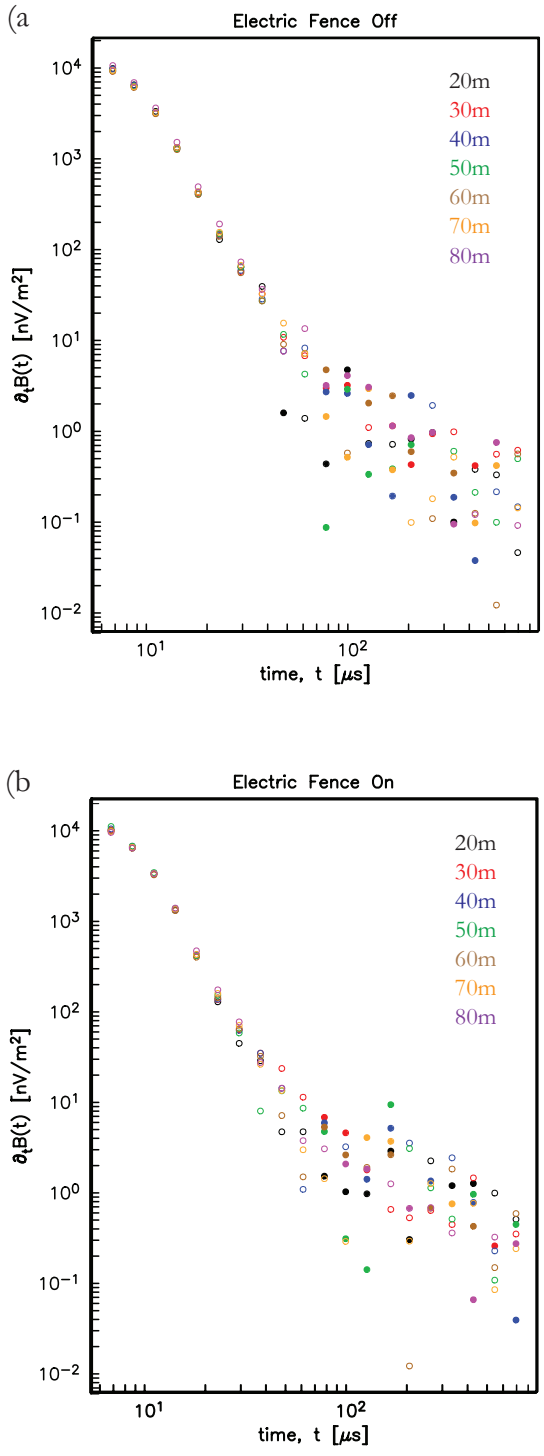


**Figure 3.7a-b.** Electrical fence test results comparing measured responses with increasing offset for the electrical fence turned on (a) and turned off (b). The color of the symbols corresponds to the offset of the same color. Open circles correspond to negative values and closed circles correspond to positive values.


**Figure 3.8.** Kentland Farm field site base map with the 180 m survey line shown in red (© 2009 **Google Earth**).

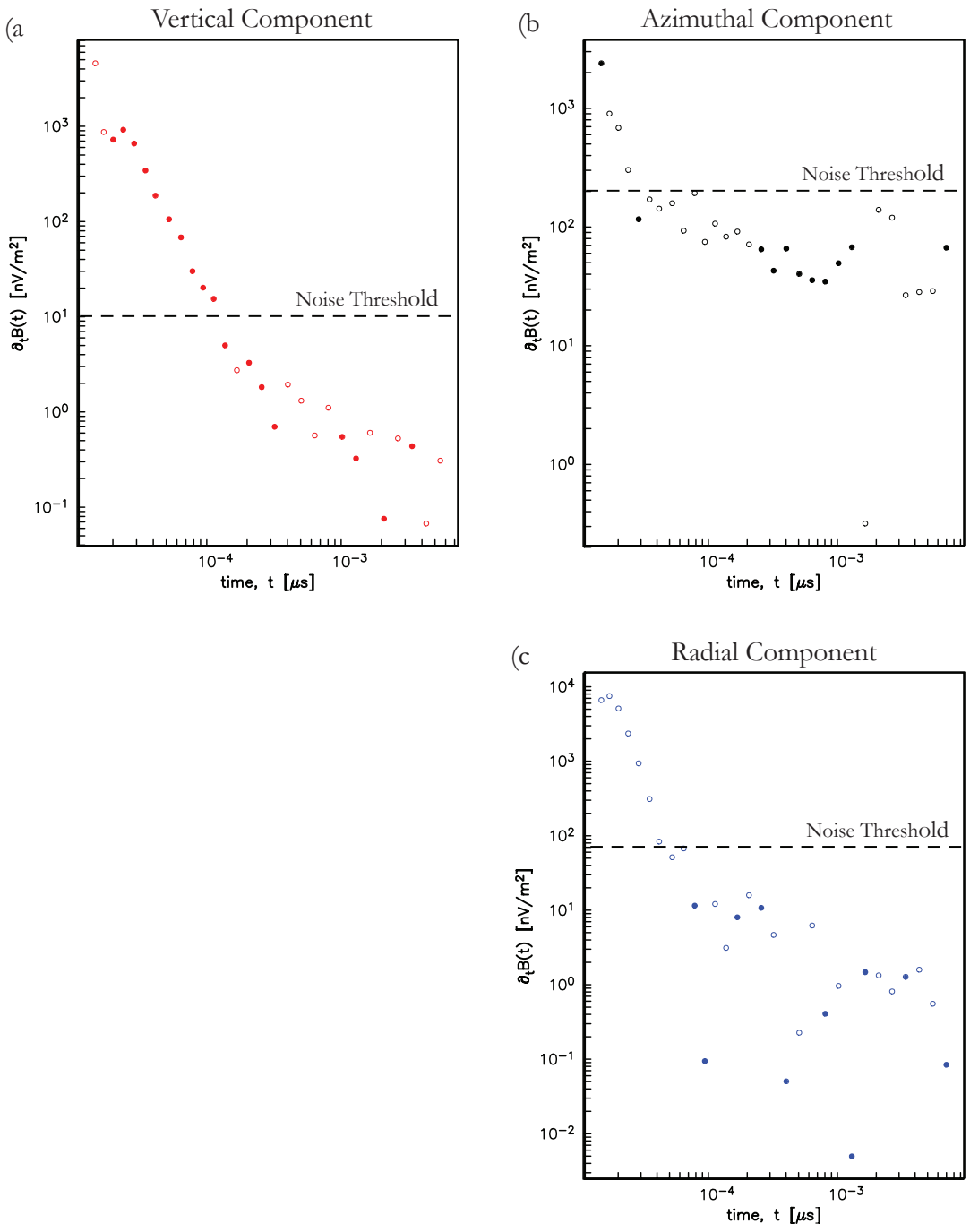


**Figure 3.9a-c.** Example measured response of the vertical component (a), azimuthal component (b), and radial component for a 60 m TX – RX on the 40 m terrace at Kentland Farm. Open circles correspond to negative values and closed circles correspond to positive values. The dashed lines on a, b, and c represents the noise threshold for each component respectively

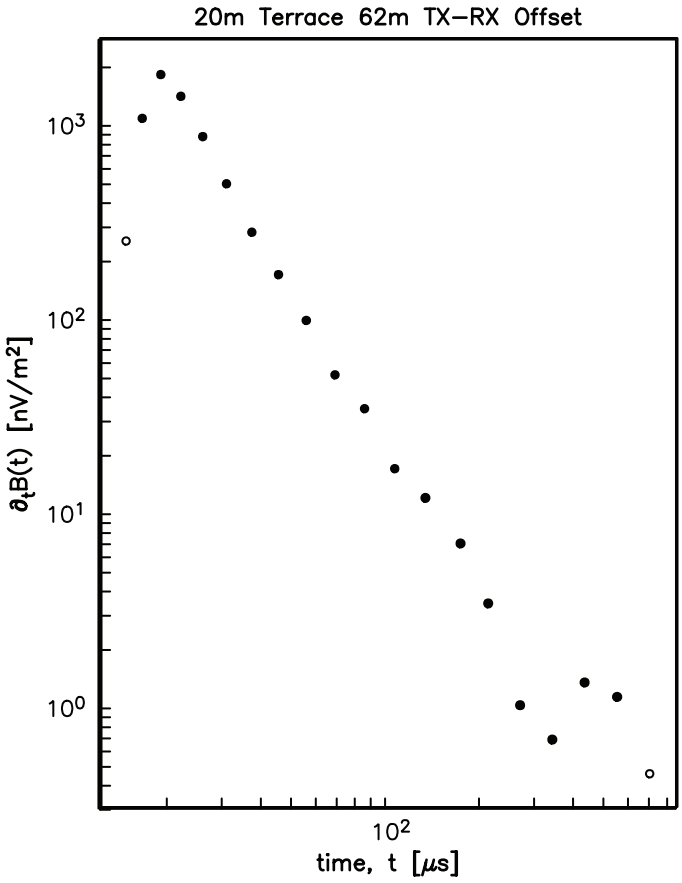


**Figure 3.10.** Example of the measured vertical component for a 62 m TX-RX separation on the 20 m terrace at Kentland Farm. Note, 20 gate mode with a 1.5 A TX current was used on the 20 m terrace profile. Open circles correspond to negative values and closed circles correspond to positive values.

# Chapter 4: Analysis

Although inversion is the "go-to" method for analyzing geophysical data, 3D full waveform inversion is computationally costly and requires specialized cluster-based software. Restricting the analysis to the less costly 1D and 2D domain eases the computational burden, but with the caveat that the data may not conform to such assumptions. Therefore, low-dimensional inversions can be troublesome, often exhibiting poor convergence (if any) and large data misfits. The data collected here will be analyzed by three independent methods: Log-normalized $\partial t\mathbf{B}_z$ pseudo-sections, zero-crossing moveout (ZCMO), and regularized 1D Occam inversion. These methods vary in their computational cost and collectively provide crosschecks for a self-consistent inference of subsurface properties.

## 4.1 Log-normalized $\partial t\mathbf{B}_z$ Pseudo-sections

Before embarking on inversion, a fast, first order estimation of the lateral and vertical conductivity variations was conducted by plotting pseudo-sections of the log-normalized time derivative of the vertical magnetic field component $\partial t\mathbf{B}_z$. Common offset pseudo-sections were assembled for TX – RX separations ranging from 30 m to 100 m (Figure 4.1a-h). In each plot, the x-axis represents the traverse distance from E to W, and the y-axis represents the first 13 gates of the time series with a center gate time interval of $14.8\,\mu s$ to $167.7\,\mu s$ (referenced from the beginning of TX turn-off). This time series was chosen for its reliability above the noise threshold. The color scale represents $\partial t\mathbf{B}_z$ values that were log-normalized by the maximum positive $\partial t\mathbf{B}_z$, allowing for a direct comparison between common offset transients and are contoured at an interval of 0.2 ranging from 0 to -2. The log-normalized limit of -2 was chosen for similar reasons as the limit on gate times, as the average quality signal level extended two orders of magnitude below the maximum $\partial t\mathbf{B}_z$ value. To simplify the pseudo-sections, early time gate measurements occurring before the zero crossing were not shown. If we examine each pseudo-section we notice large variations both vertically in time and laterally in space. Recall that synthetic tests involving a three-layered Earth model with a sinkhole (figure 2.7a-d) show

that lateral variations in the pseudo-sections corresponded to lateral changes in the electrical structure, with more conductive regions being represented by thicker contours in time. In addition, the pseudo-section was shown to be depth sensitive as a function of TX – RX separation. Therefore, we can infer that lateral variations for a common offset as well as vertical variations between a suite of offsets are indicative of variations in the conductivity structure along the traverse. For example, the 30 m constant TX – RX separation the pseudo-section (Figure 4.1a) shows increasing conductivity from East to West. Additionally, an observed change in lateral electrical structure is over the range of offsets is seen with a shift from E to W increasing conductivity at short offsets (≤ 40 m) to E to W decreasing conductivity at larger offsets (≥ 80 m). The small oscillations on the contours themselves are a product of the 3D structure observed at Kentland Farm. With minimal computational effort required, log-normalized $\partial t\mathbf{B}_z$ pseudo-sections provide a decent, qualitative first-order estimate of the lateral complexities on a field site.

### 4.2 Zero-Crossing Moveout Analysis

Due to the gently diffusive nature of eddy currents, there exists relatively few features in the time series that can be analyzed. One, however, is the Zero-Crossing Moveout (ZCMO). Recall from chapter 2 that for transient offset soundings, the time derivative of the vertical magnetic field $\partial t\mathbf{B}_z$ undergoes a polarity revesal as the induced eddy currents diffuse past the RX coil. That is, the time in which $\partial t\mathbf{B}_z$ is zero relates approximately to when the eddy currents are below the RX. The zero-crossing moveout time, as outlined in section 2.3, was captured by linearly interpolating the two gate times that bracket the observed polarity reversal for a given TX – RX pair. A compilation of zero-crossing moveout results from the 18 separate roving receiver profiles collected along the 40 m terrace survey line is shown in figure 4.2. The linear fits represent the average zero-crossing times for two sections of the ZCMO curve: the first linear approximation of the ZCMO curve is for TX – RX separations of 30 m to 70 m, and the second linear approximation of the ZCMO curve is for TX – RX seperations of 80 m to 180 ms. Initially, a rapid moveout is observed at short offsets (<80 m) with a slope of $\beta = 0.102 \pm 0.0034$. A noticeable inflection point lies at the 80 m TX – RX separation ($\log(L^2) = 3.8$) in which the

moveout rate for larger offsets increases with a slope of $\beta = 0.473 \pm 0.0087$. It is tempting to include a third possible change in slope at the far offsets (170 m and 180 m); however, such a speculation is poorly constrained by the data.

Theoretical ZCMO curves asymptote at short offsets to the turn-off ramp time. In order to accurately calculate a matching theoretical solution, the appropriate ramp time is necessary. Although a ramp time of $8\,\mu s$ is documented in the Geonics literature (PROTEM 47D OPERATING MANUAL for 20/30 Gate Model, 2006) for an 8-turn TX loop, oscilloscope measurements of the change in TX current showed a ramp time of approximately $13.5\,\mu s$ (figure 4.3). Figure 4.4 shows the theoretical ZCMO response curves for a uniform half-space ($\sigma$ = 0.001 S/m) for the assumed ramp of $8\,\mu s$ (red line) and the oscilloscope approximated ramp of $13.5\,\mu s$ (green line) as compared to the 40 m terrace zero crossing data. Clearly, the $13.5\,\mu s$ approximated ramp time corresponds to the ZCMO's asymptotic limit; therefore, it will be used for modeling purposes. The slower than expected ramp time could be potentially a result of either coupled, mutual impedance of the transmitter with the conductive near-surface resulting in a slower than anticipated TX turn off or the product of the instrumentation itself.

In order to estimate the physical parameters (conductivities and depth to bedrock) of the 40 m terrace, a novel, brute force two-layer modeling procedure (3 model parameters) was attempted. This process compares ZCMO curves to the observed data via a line search with the root mean square (rms) misfit quantifying the quality of fit. With the lack of *a priori* information available for the 40 m terrace, ZCMO results from a previously characterized field site located on the 20 m terrace – in which the depth to bedrock has been determined from auger holes to be roughly 5-7m (Schwarz et al., 2008) – were used to determine the ability of the modeling procedure to extract reasonable and valid Earth models. ZCMO moveout results (symbols) from a 56m to 176m section of the traverse is shown in Figure 4.5, with the small undulations in the observed response resulting from artifacts of the linear interpolation procedure used to locate the zero crossing times (Weiss & Everett, 2007). The accompanying best-fit model (red line) – result of the iterative procedure that tests for a broad range of layer conductivity pairs assuming a 5 m overburden thickness – represents a conductive upper layer of $\sigma = 0.009$ S/m over a more resistive half-space of $\sigma = 0.0024$ S/m with a rms misfit of 0.0064. This result approximately agrees with the average conductivities recovered in a previous nearby electrical investigations seen by Schwartz et al. (2008), which ranged from 0.0125 S/m to 0.0015 S/m for the overburden

and .00435 S/m to 0.0015 S/m for the limestone bedrock. Furthermore, theoretical transient responses produced from the best fit Earth model adequately fits the observed response (figure 4.6) given the simplicity of the model and the complexity of the environment. With the confirmed ability of our ZCMO modeling technique to produce a valid simple earth model (providing a known constraint), we extended the procedure to the 40 m terrace.

The ZCMO model estimation was carried out for a range of overburden thicknesses (2.5 m to 30 m). The grid-search algorithm tests all possible 2-layer conductivity models at a 0.1 interval for an overburden log conductivity range of -1.0 S/m to -2.5 S/m and half-space log conductivity range of -2.0 S/m to -3.5 S/m. Contour plots of the rms misfit surface in model space for increasing depths are shown in figure 4.7a-l, contoured at an interval of 0.1, with cooler colors representing increasingly smaller misfit values. A noticeable arc-trench feature of relatively small rms values (indicative of suitable conductivity models) is observed for each thickness, with the best-fit model typically located at the corner of the arc. At large overburden thickness (> 20 m), the half-space conductivity has less of an impact on the overall model allowing for a wide terminal conductivity range with a consistently observed overburden conductivity of ~ 0.001 S/m. A plot of the best-fit model for each overburden thickness in log conductivity model space is shown in figure 4.8 with the size of the circles corresponding to the rms misfit. A trend similar to the trend observed in the fixed thickness contour plots is also seen on the best-fit models plot. At shallow depths ($\leq$ 7.5 m), a highly variable top layer conductivity is observed with a consistent half-space conductivity. At larger depths ($\geq$ 27.5 m), the top layer conductivity is fairly stable; however, the half-space conductivity varies widely. Although there appears to be relatively no correlation of the size of the misfit as a function of layer thickness, the distribution of best-fit models however is interesting. If we remove the poorly constrained, large thickness outliers (h = 27.5 m and 30 m) as well as the shallow thickness models (<5 m), which would be unlikely given our knowledge of the other terraces (i.e. 20 m terrace h $\approx$ 5-7 m), a cluster of optimum models is observed. The best fitting model of these is a 17.5 m thick conductive layer of $\sigma$ = -0.02 S/m overlying a resistive half-space of $\sigma$ = -0.0025 S/m.

### 4.3 Regularized Occam Inversion

In order to find a defensibly complex earth model that better matches our data, our second analysis employed the use of a 1D Regularized Occam inversion. The goal of any inversion is to find a theoretical model whose data matches the observed field data within a specified tolerance. Although there exists a variety of different inversion techniques, an Occam style inversion (Constable et al., 1987) was chosen as it is designed to find the simplest, smoothest model that fits the data while avoiding the addition of any unnecessary structure. The following is a simple outline of the Occam inversion from Constable et al. (1987). For the non-linear problem, if we define **d** as our observed data vector and **F**[**m**] as the predicted data resulting from some model **m**, then the data misfit needed to be to be minimized is:

$$X^2 = \left\| \mathbf{Wd} - \mathbf{WF}[\mathbf{m}] \right\|^2 \tag{4.1}$$

where **W** is a diagonal matrix composed of the reciprocal of the data errors. **F**[**m**] is a forward solver that uses theoretical electromagnetic field solutions to calculate the predicted earth response from a series of model parameters including conductivities and layer basal depths. To ensure smoothness and simplicity, an Occam inversion employs a regularization procedure that penalizes a model for complexity or roughness and can also include constraints from additional geophysical, geological, or well log data. With the addition of the regularization $\left\| \partial \mathbf{m} \right\|^2$, a new objective function to be minimized is defined:

$$U = \left\| \partial \mathbf{m} \right\|^2 + \mu^{-1} \left\{ \left\| \mathbf{Wd} - \mathbf{F}[\mathbf{m}] \right\|^2 - X_*^2 \right\} \tag{4.2}$$

where $X_*^2$ is the user defined misfit tolerance and $\mu^{-1}$ is the Lagrange multiplier which helps force the minimization of the misfit. In order to solve the non-linear system, an iterative refinement procedure is then undertaken in which an initial starting model $\mathbf{m}_1$defined by the user is used to find successive models. By using a finite-differences approach we can discretely approximate the Frichét derivatives, which make up the Jacobian matrix $J_{ij} = {\partial F_i[\mathbf{m}]} \big/ {\partial \mathbf{m}_j}$, by introducing a small perturbation to the starting model $\mathbf{m}_1$. If we assume that the forward

solution is differentiable at the starting model with sufficiently small model differences, $\Delta = \mathbf{m}_1 - \mathbf{m}_2$, we get the following (Constable et al., 1987):

$$\mathbf{F}[\mathbf{m}_1 + \Delta] = \mathbf{F}[\mathbf{m}_1] + \mathbf{J}_1\Delta + \varepsilon \tag{4.3}$$

By substituting equation 4.3 into the objective functional, the system becomes linear and the unconstrained functional can now be solved with respect to the second model, $\mathbf{m}_2$, which minimizes $U$:

$$U = \left\|\partial \mathbf{m}_2\right\|^2 + \mu^{-1}\left\{\left\|\mathbf{W}(\mathbf{d} - \mathbf{F}[\mathbf{m}_1] + \mathbf{J}_1\mathbf{m}_1) - \mathbf{W}\mathbf{J}_1\mathbf{m}_2\right\|^2 - X_*^2\right\} \tag{4.4}$$

From here an iterative procedure can then be devised to find successive models until the specified misfit tolerance is achieved resulting in an independent final model. Because the objective of an Occam inversion is to find the simplest model that fits the data, the final model is chosen to be one that has both minimal roughness and misfit (figure 4.9). Dr. Chester J. Weiss wrote the Occam style inversion code used in this study with the forward solver following the theoretical solutions for the vertical magnetic induction field exterior to and at the center of a loop source (Ryu et al., 1970; Weiss, 2010).

The model space in which the inversion searches is an irregular surface that may exhibit numerous local minima that could potentially result in a convergent model that does not represent the global minimum. Non-linear inversion problems such as the Occam inversion employed here require an initial starting model (Constable et al., 1987). Therefore, the choice of starting model is vital to achieving a realistic earth model. Figure 4.10a-c show examples of converged inversion results using three different initial models with varying half-space conductivity: a) $\sigma$ = 0.032 S/m, b) $\sigma$ = 0.001 S/m, and c) $\sigma$ = 0.0032 S/m. For all of the inversion results presented, the left figure in each group of plots shows the measured transient response (symbols) and model response (lines) from the final Occam model assuming a 1D earth with only data above the noise threshold ($10^{-8}$ V/m$^2$) being inverted. The center panel shows the final recovered 1D Occam conductivity model as a function of depth. As shown, the choice of initial model parameters has a substantial effect on the final recovered model with only the $\sigma$ = 0.001 S/m half-space model (suggested from the ZCMO modeling results) yielding reasonable results. Therefore, achieving a reliable inversion result without a reasonable estimation of the

general conductivity of the survey area is very difficult. The ZCMO modeling procedure described above yielded approximates two-layer conductivity models for twelve overburden thickness on the 40 m terrace that could be potential candidates for use as a starting model. Inversions were conducted with the ZCMO derived conductivity models being used as an initial model (figure 4.11a-i). Conductivity models for overburden thickness of 2.5 m, 5 m, and 30 m did not yield sensible results and therefore were not included. Notice that all of the recovered conductivity models are very similar and therefore represent a "robust" solution. Also, the final models recovered using the two-layered initial model are relatively similar to the final model recovered when using a $\sigma = 0.001$ S/m half-space as the starting model. We can conclude that a general approximation of the bulk conductivity of the survey area is a valid initial model and can produce reasonable inversion results.

Inverse solutions of transient vertical magnetic induction field $\partial t\mathbf{B}_z$ along the survey line located on the 40 m terrace for six TX – RX separations (40 m, 50 m, 60 m, 70 m, 80 m, and 90 m) can be seen in figures 4.12a-g. Note, two inversion results were obtained for a 70 m TX – RX separation at different ends of the profile. An initial model consisting of 23 model parameters that represented a 10 m thick conductive overburden ($\sigma = 0.016$ S/m) overlying a resistive half-space ($\sigma = 0.0025$ S/m) was used for each inversion, with the model layer thicknesses discretized to increase as a function of depth. Although the recovered model does not completely match the observed response, the quality of fit is acceptable given the 3D complexity of the subsurface in this area and the single dimension restriction of the conductivity model.

Figure 4.13a-b shows the sensitivity (Jacobian) matrix for 70 m TX – RX offset sounding on at both East (figure 4.13a) and West (figure 4.13b) ends of the 40 m terrace profile. Each sensitivity plot is for the first 12 data points (horizontal axis) and the 22 model parameters (vertical axis) representing layer conductivities in the Earth model. The color scale shows how much a given datum (e.g. magnetic flux at some time gate) changes when an isolated part of the model is perturbed. In the plots, warm colors indicate high sensitivity of a given measurement to a particular model parameter, whilst cool colors indicate low sensitivity. As shown, the 70 m TX – RX separation inversion results at both ends of the 40 m terrace profile are sufficiently sensitive (as indicated by the warm colors) to changes in conductivity structure at all depths including the terminal half-space. In the Western model, the model is sensitive at all parameters for the first 9 data points with sensitivity decreasing for data points $\geq 10$. However, a lobe of

decreased sensitivity is observed at later data points (≥ 9) on the Eastern model, possibly resulting from the increased conductivity observed in the 70 m offset E model (figure 4.12d) serving to limit the sensitivity of deeper structure.

The recovered models represent both ends of the survey line with TX – RX separations of 40 m, 60 m, and 70 m located on the Eastern end and TX – RX separations of 50 m, 70 m, 80 m, and 90 m located on the Western end of the line. Notice that an inversion result on both ends of the profile for a single TX – RX separation only occurred once, which is a true testament of the non-1D Earth. For all models, a general trend of a thin resistive layer over a conductive layer over a more resistive half-space is observed of varying degree depending on profile location and TX – RX separation. The presence of an additional deep conductive layer seen in the conductivity models for the 60 m and 70 m separations is observed, however, it is not clear if it is an artifact of the inversion or required by the data. Further interpretation of the conductivity structure as a function of depth and discussion of inversion results as they pertain to the 40 m terrace will be presented in the following chapter.

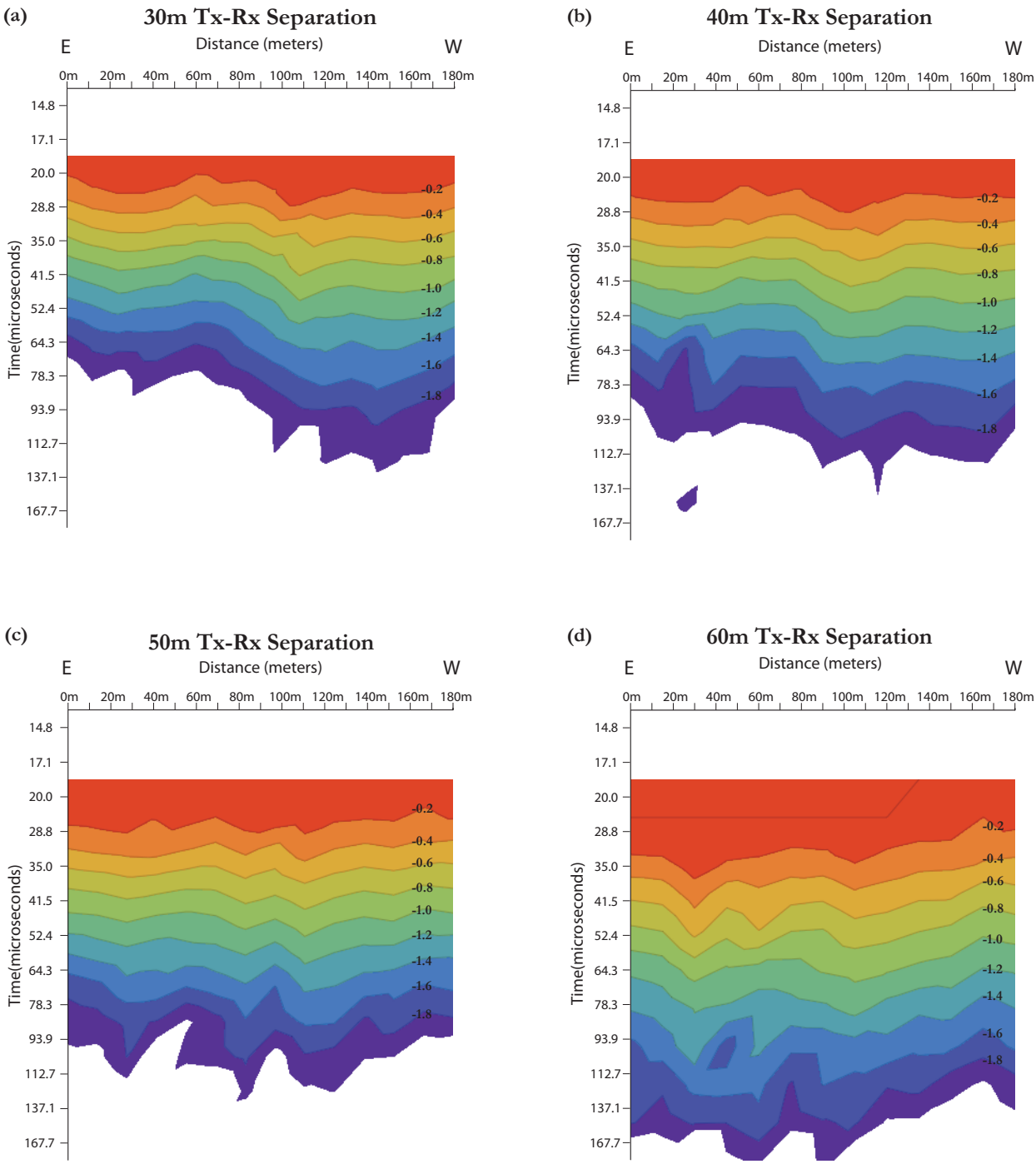


**Figure 4.1a-h.** Log-normalized $\partial t\mathbf{B}_z$ pseudo-sections for the 40 m terrace profile for TX – RX separations of: 30 m (a), 40 m (b), 50 m (c), 60 m (d), 70 m (e), 80 m (f), 90 m (g), and 100 m (h). The horizontal distance represents the distance along the traverse. The vertical axis shows the center times of the first 13 time gates used in this analysis. The color scale represents log-normalized voltages contoured ranging from 0 to -2, contoured at a -0.2 interval.

(e

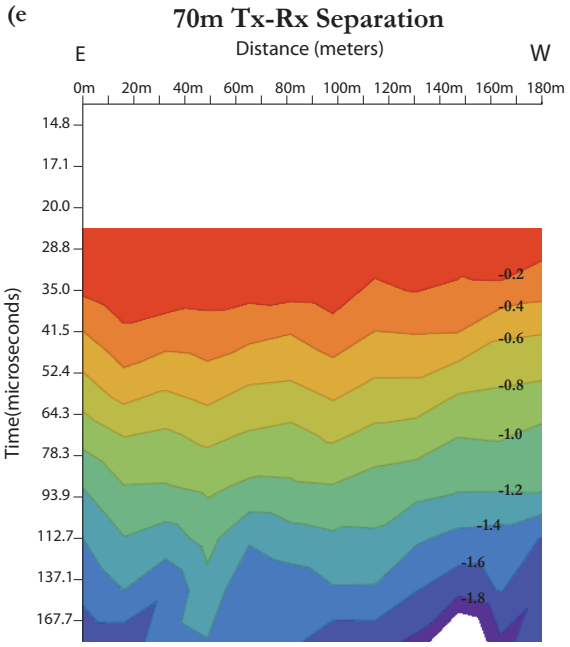
70m Tx-Rx Separation
E
Distance (meters)
W
0m 20m 40m 60m 80m 100m 120m 140m 160m 180m
Time(microseconds)
14.8 17.1 20.0 28.8 35.0 41.5 52.4 64.3 78.3 93.9 112.7 137.1 167.7
-0.2 -0.4 -0.6 -0.8 -1.0 -1.2 -1.4 -1.6 -1.8

(f

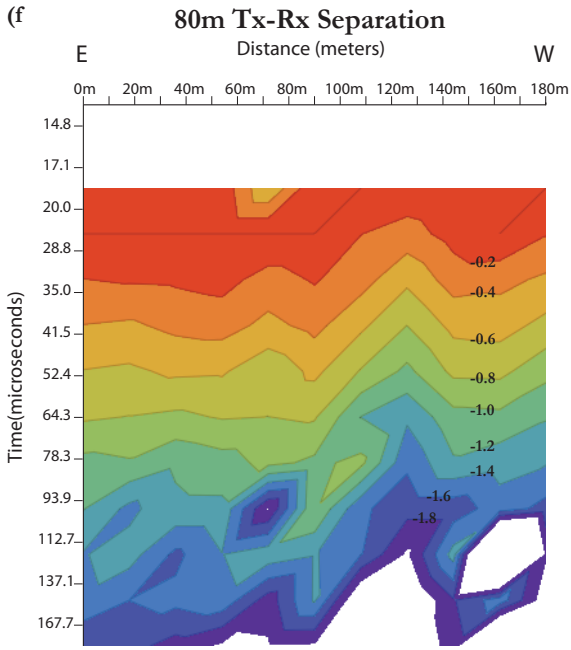
80m Tx-Rx Separation
E
Distance (meters)
W
0m 20m 40m 60m 80m 100m 120m 140m 160m 180m
Time(microseconds)
14.8 17.1 20.0 28.8 35.0 41.5 52.4 64.3 78.3 93.9 112.7 137.1 167.7
-0.2 -0.4 -0.6 -0.8 -1.0 -1.2 -1.4 -1.6 -1.8

(g

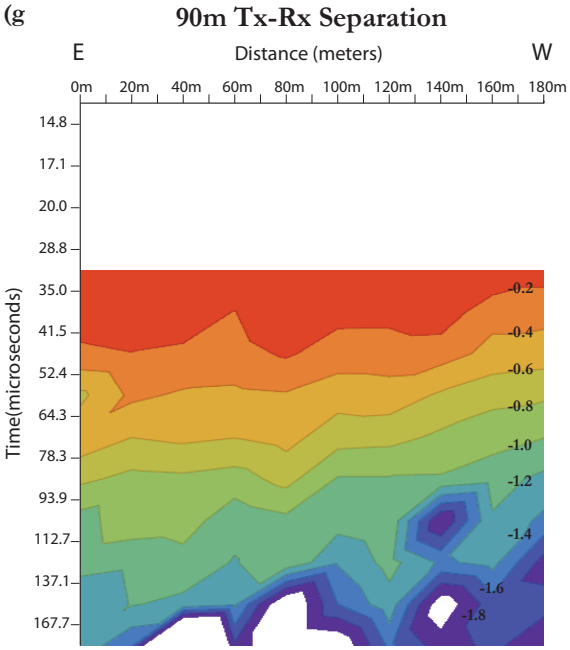
90m Tx-Rx Separation
E
Distance (meters)
W
0m 20m 40m 60m 80m 100m 120m 140m 160m 180m
Time(microseconds)
14.8 17.1 20.0 28.8 35.0 41.5 52.4 64.3 78.3 93.9 112.7 137.1 167.7
-0.2 -0.4 -0.6 -0.8 -1.0 -1.2 -1.4 -1.6 -1.8

(h

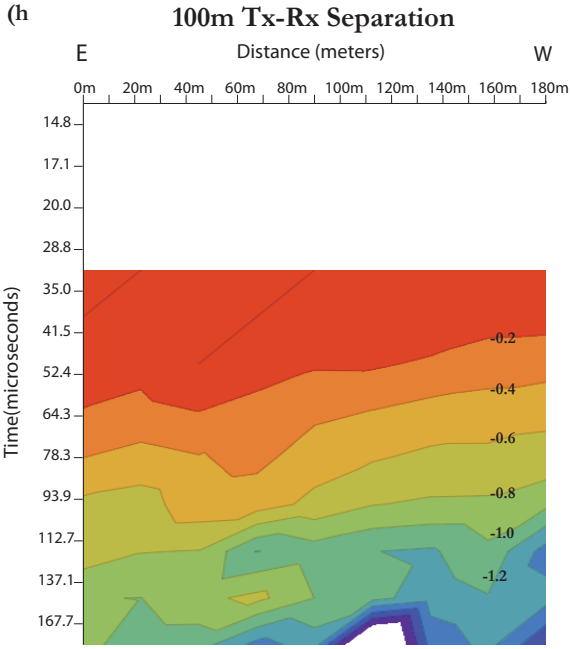
100m Tx-Rx Separation
E
Distance (meters)
W
0m 20m 40m 60m 80m 100m 120m 140m 160m 180m
Time(microseconds)
14.8 17.1 20.0 28.8 35.0 41.5 52.4 64.3 78.3 93.9 112.7 137.1 167.7
-0.2 -0.4 -0.6 -0.8 -1.0 -1.2

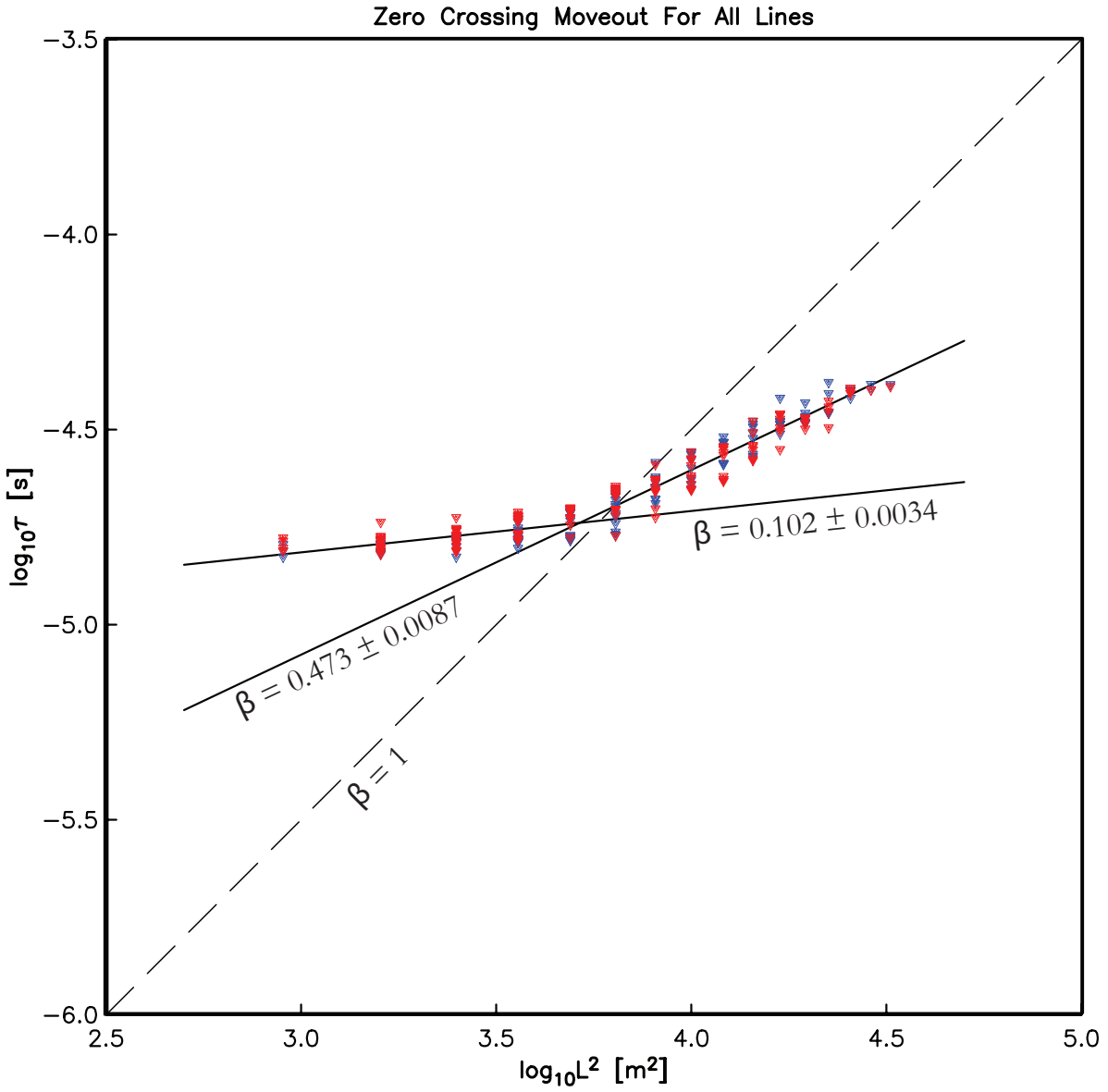


**Figure 4.2.** Assemblage of Zero-Crossing Moveout (ZCMO) results from 40 m terrace with TX – RX separations ranging from 30 m to 180 m. Red symbols represent measurements made with the RX to the East of the TX while blue symbols represent the measurements made with the RX to the West of the TX. An example of a classical moveout $\beta = 1$ (dashed line) is shown for reference.

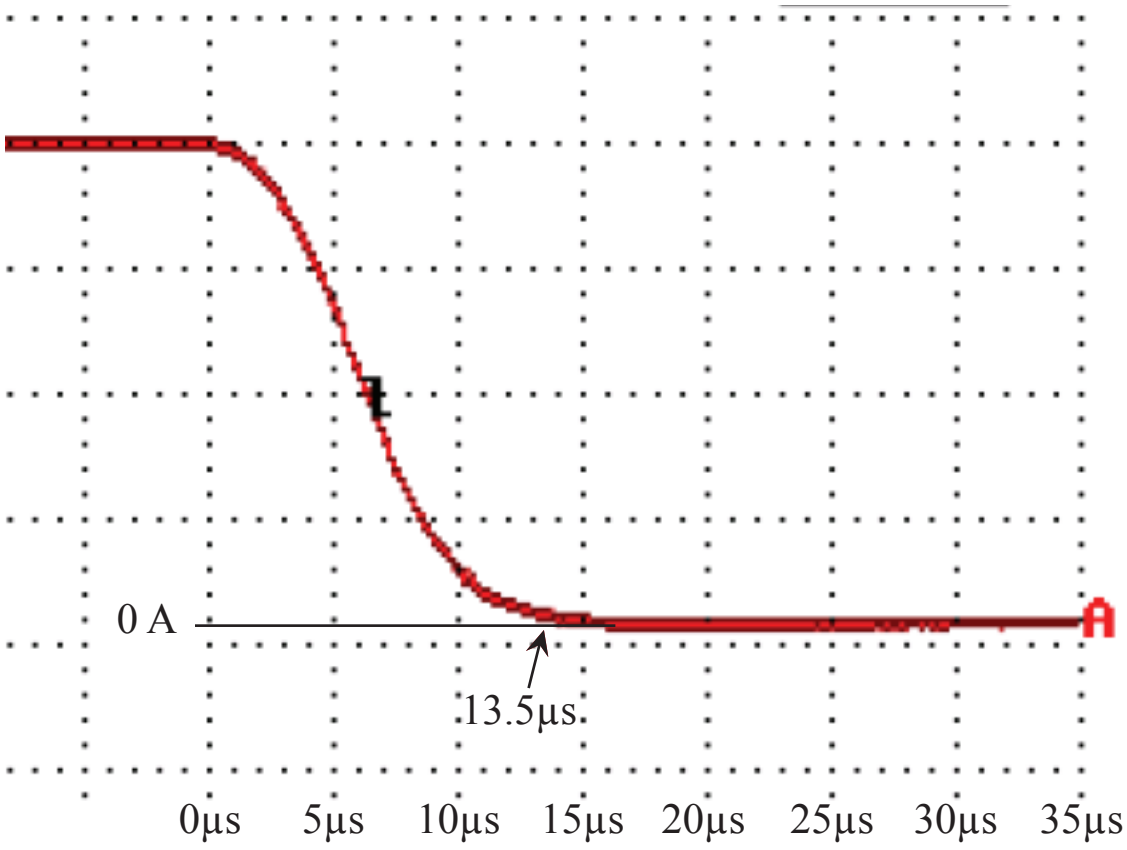


**Figure 4.3.** Oscilloscope measurement of the actual TX turn-off ramp. The vertical axis represents the measured current at 2A increments. The horizontal axis represents time (µs) with the labels indicating time elapsed from TX turn-off. As shown, 13.5 µs is an acceptable estimate for the ramp time.

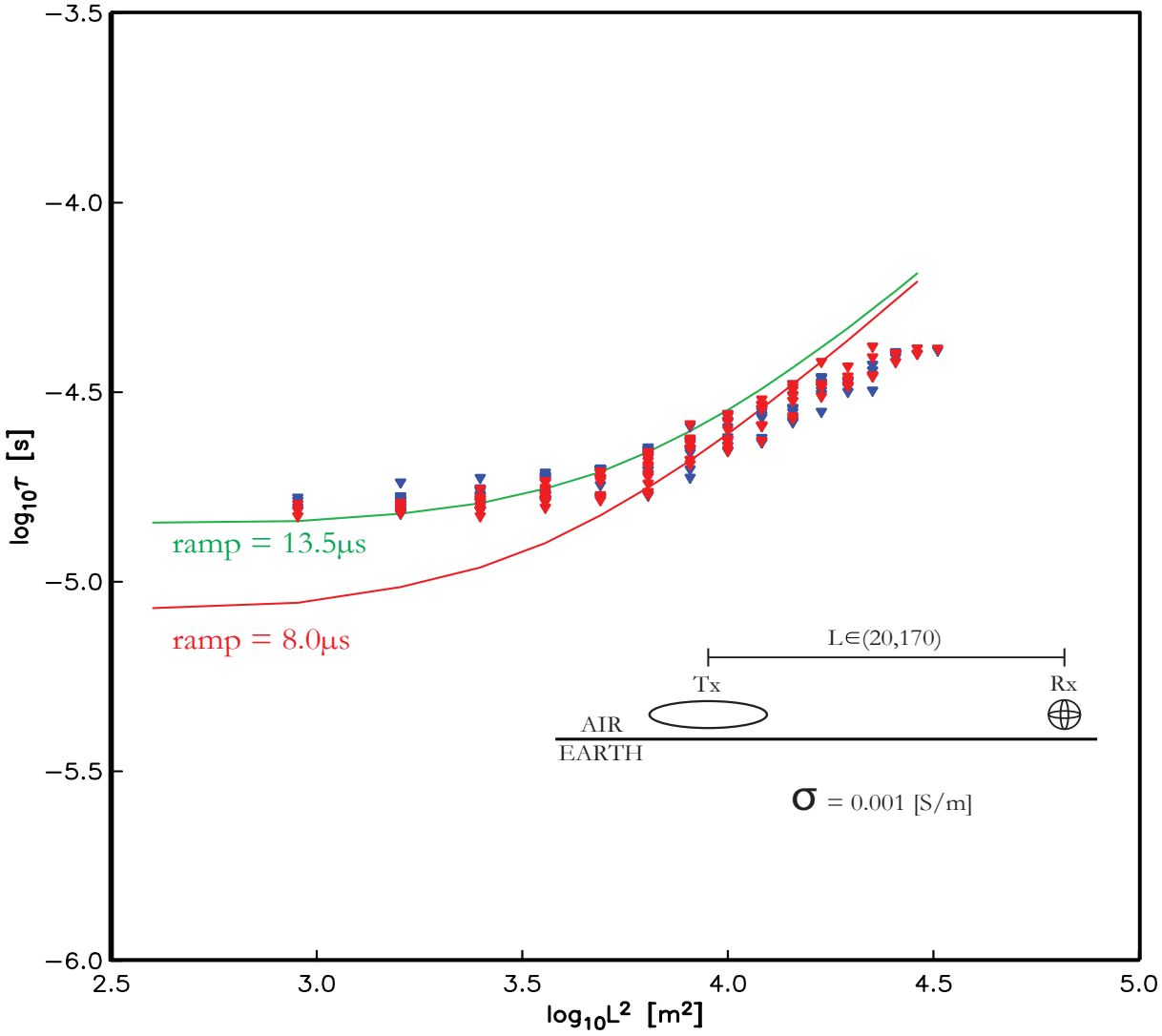


**Figure 4.4.** Comparison of observed ZCMO from the 40 m terrace (symbols) with ZCMO curves for a uniform half-space of σ = 0.001 S/m for the oscilloscope estimated 13.5 $\mu s$ ramp time (green line) and the manufacturers specified 8 $\mu s$ ramp time (red line).

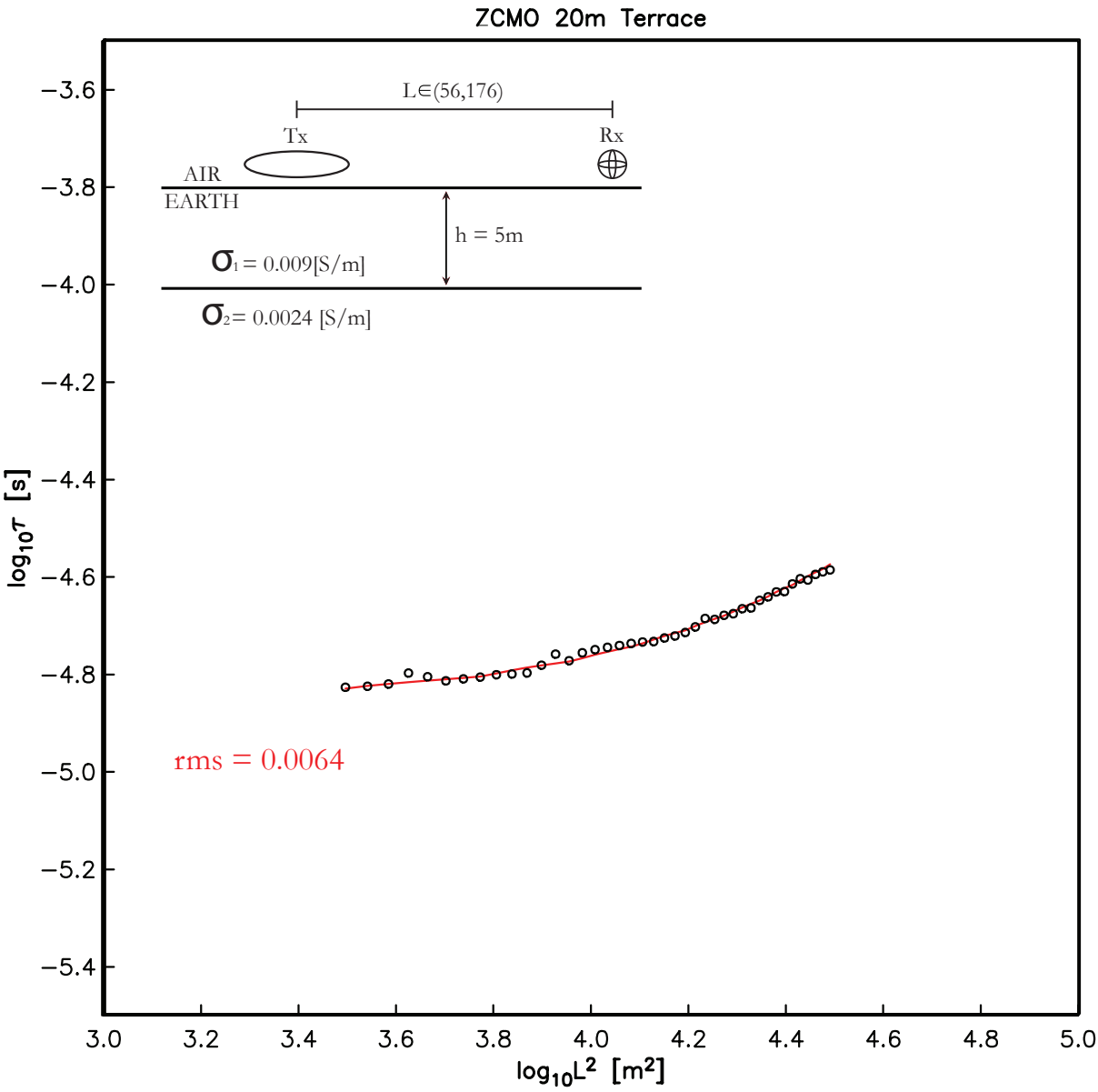


**Figure 4.5.** The final result of the ZCMO model estimation on the 20 m terrace at Kentland Farm, VA assuming a 5 m overburden thickness. The best-fit conductivity model (red line) of a conductive layer ($\sigma$ = 0.009 S/m) over resistive half-space ($\sigma$ = 0.0024 S/m) matched the observed moveout (black symbols) with an rms misfit of 0.0064 S/m.

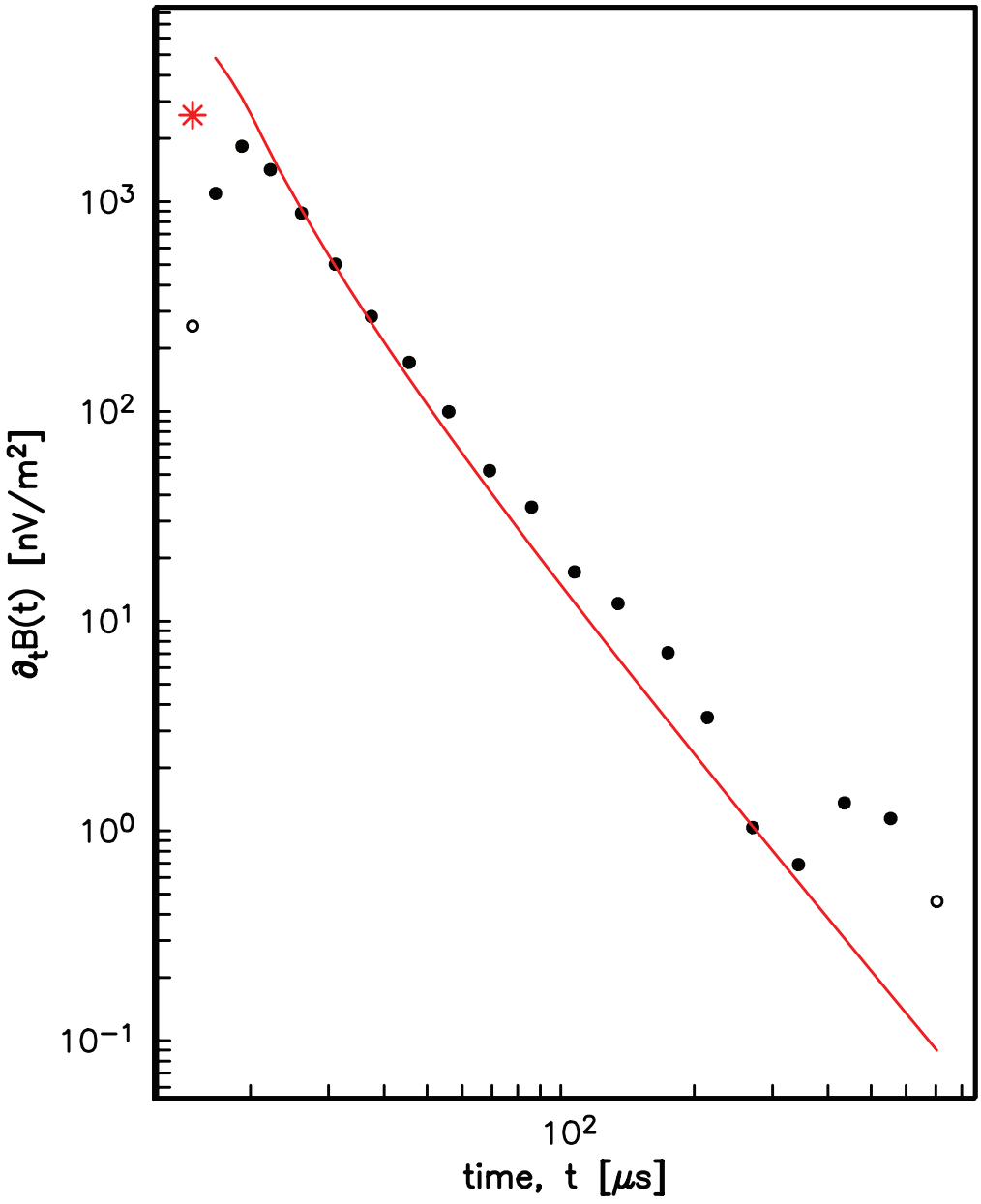


**Figure 4.6.** Comparison of the ZCMO derived best model (red line) and an observed transient response (black symbols) for a 62 m TX – RX separation on the 20 m terrace at Kentland Farm, VA. Open circles and the red asterisk correspond to negative values and closed circles and solid red line correspond to positive values.

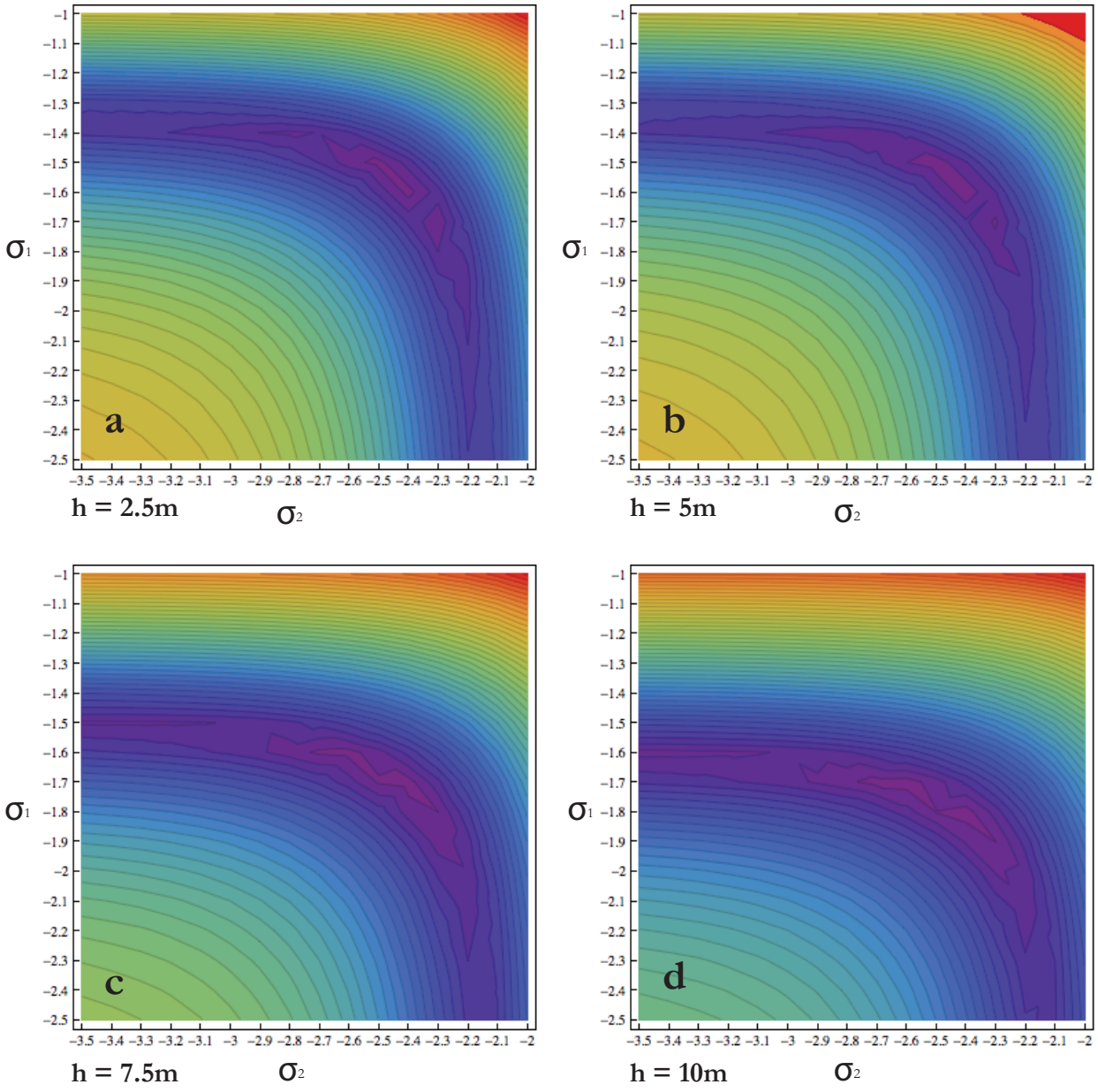


**Figure 4.7a-l.** Contour maps of the root mean squared (rms) misfit surface in log conductivity model space from the 40 m terrace for overburden thickness model ranging from 2.5 m to 30 m are shown in panels a-h, with cool colors representing areas of relatively decreasing rms misfit. Contours are at an rms misfit interval of 0.1.

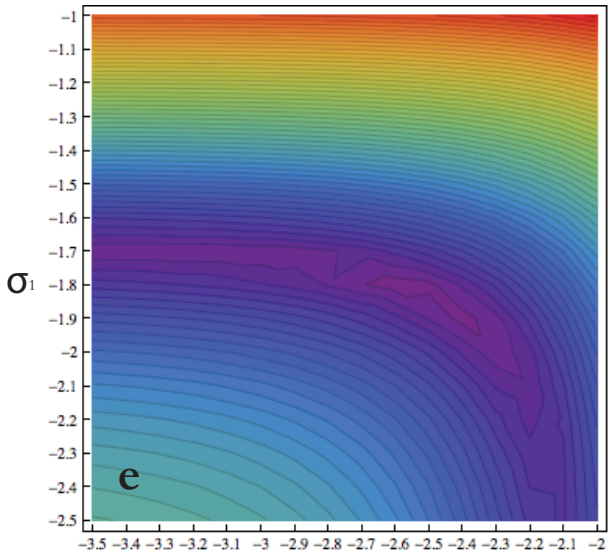


h = 12.5m

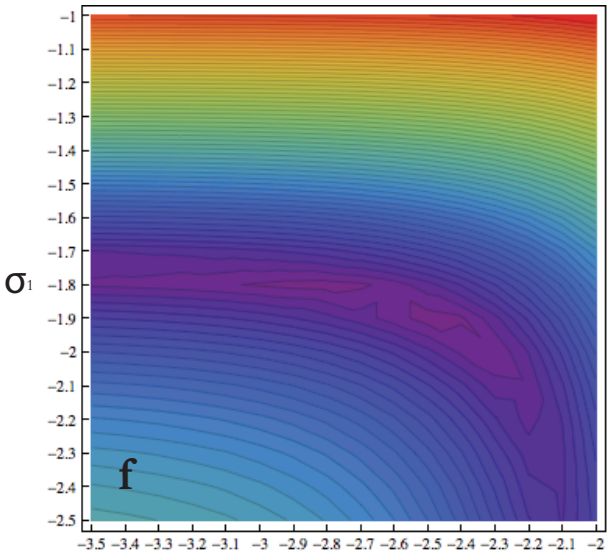


h = 15m

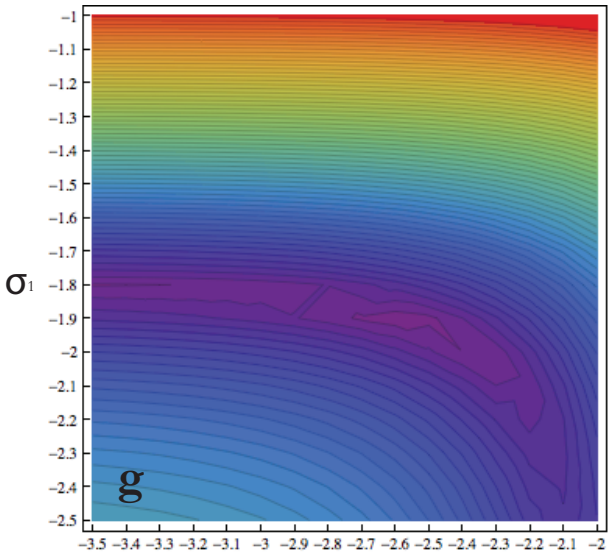


h = 17.5m

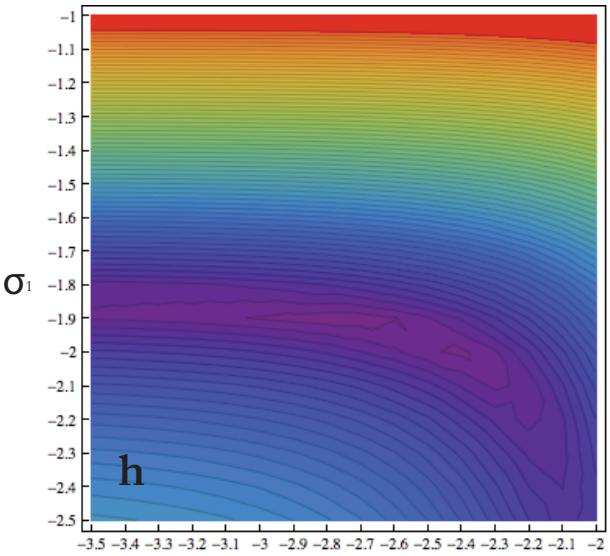


h = 20m

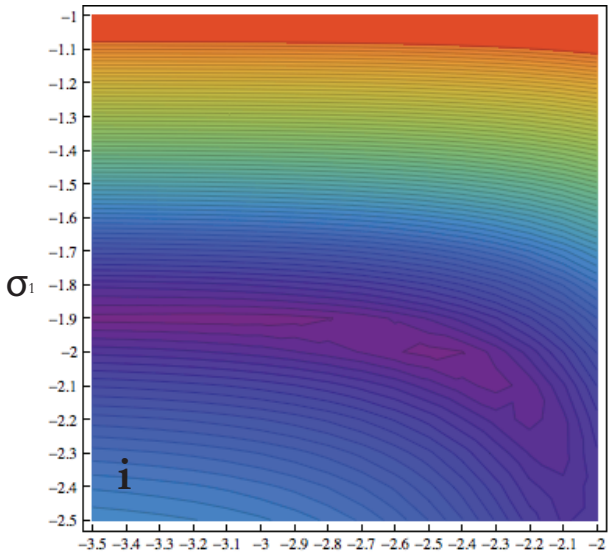
σ1
σ2
i
h = 22.5m

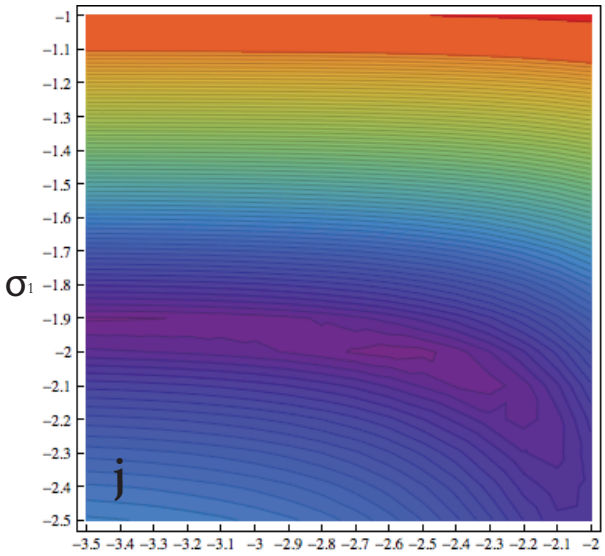
σ1
σ2
j
h = 25m

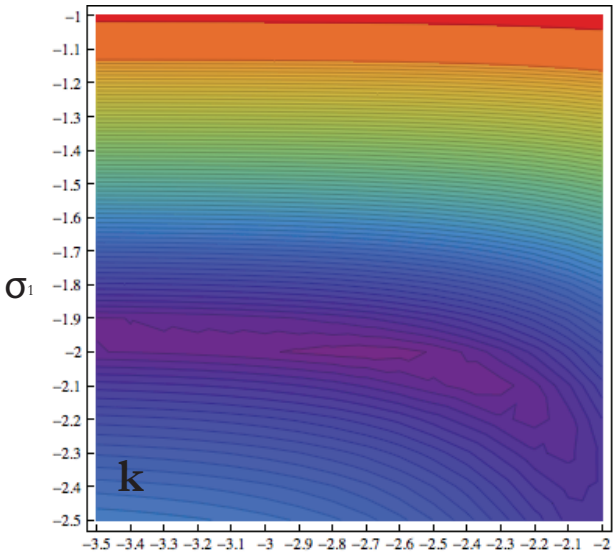
σ1
σ2
k
h = 27.5m

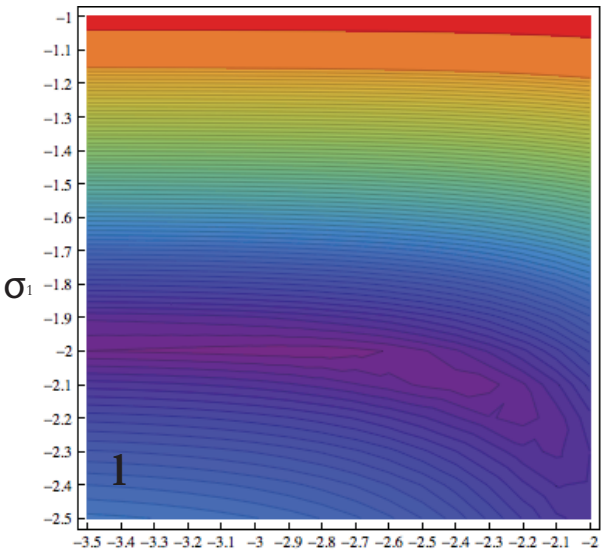
σ1
σ2
l
h = 30m

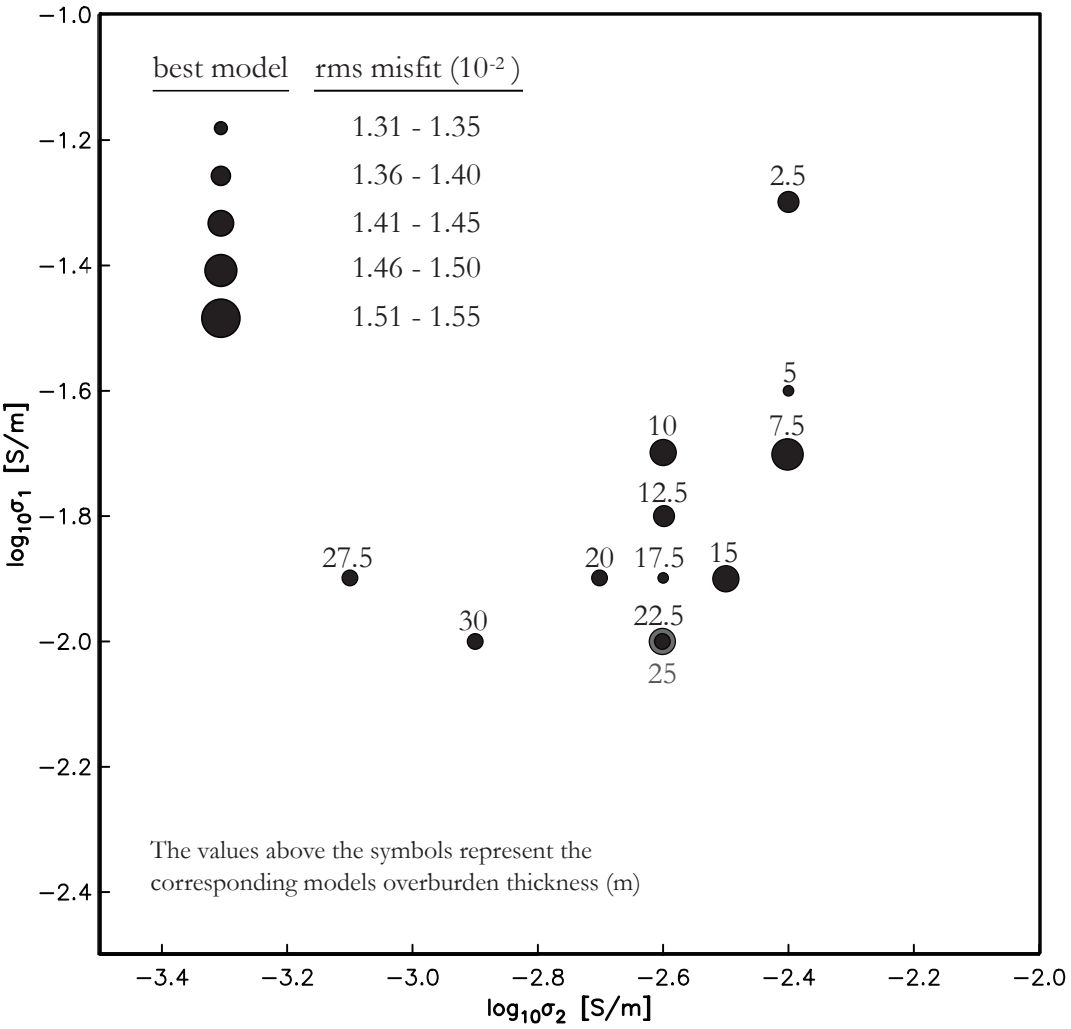


**Figure 4.8.** A plot of the optimum model (lowest rms misfit) for each of the 40 m terrace ZCMO model estimations in log conductivity model space where the size of the circles correspond to the relative size of the model rms values. The values above the symbols represents the corresponding best-fit models overburden thickness (m)

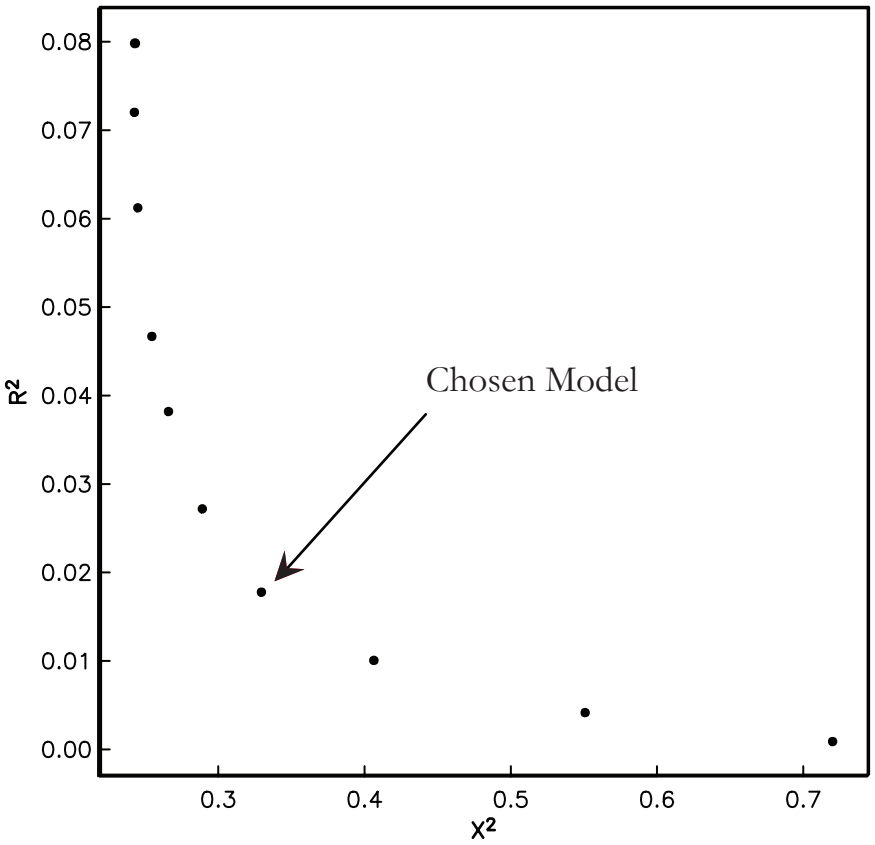


**Figure 4.9.** Example of the model roughness ($R^2$) vs. model misfit ($X^2$) plots used to choose the best model. The best model was defined to be one that maintained minimum misfit while remaining smooth and was chosen as the point that corresponded to the maximum curvature of the L curve. An example of a typical best model selection is indicated by the arrow.

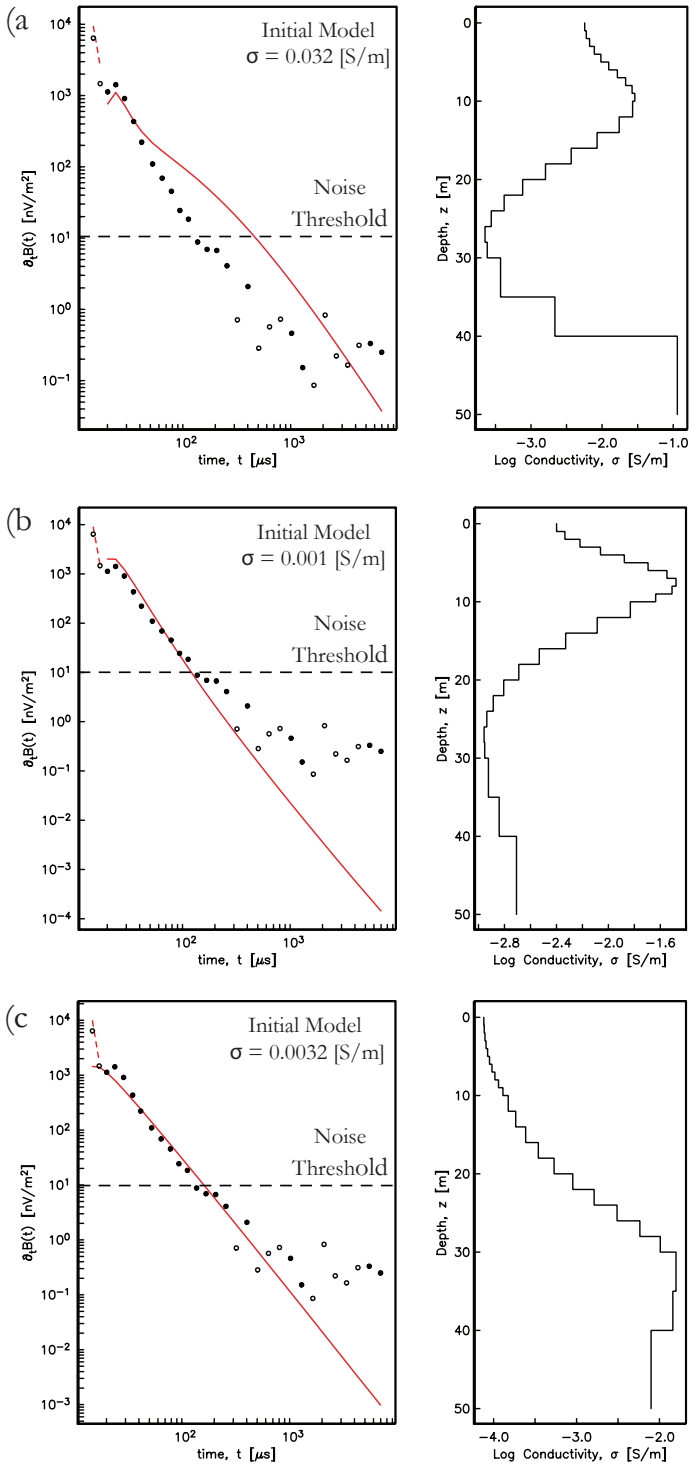


**Figure 4.10a-c.** Comparison of final Occam inversion results for three half-space initial conductivity models: a) σ = 0.032 S/m, b) σ = 0.001 S/m, and c) σ = 0.0032 S/m. The left panel shows a comparison between the observed data (symbols) and final model response (line) with only data above the $10^{-8}$ V/m$^2$ noise threshold being inverted for. The right panel shows the final Occam conductivity model as a function of depth with log conductivity on the x-axis and depth on the y-axis. Open circles correspond to negative values and closed circles correspond to positive values.

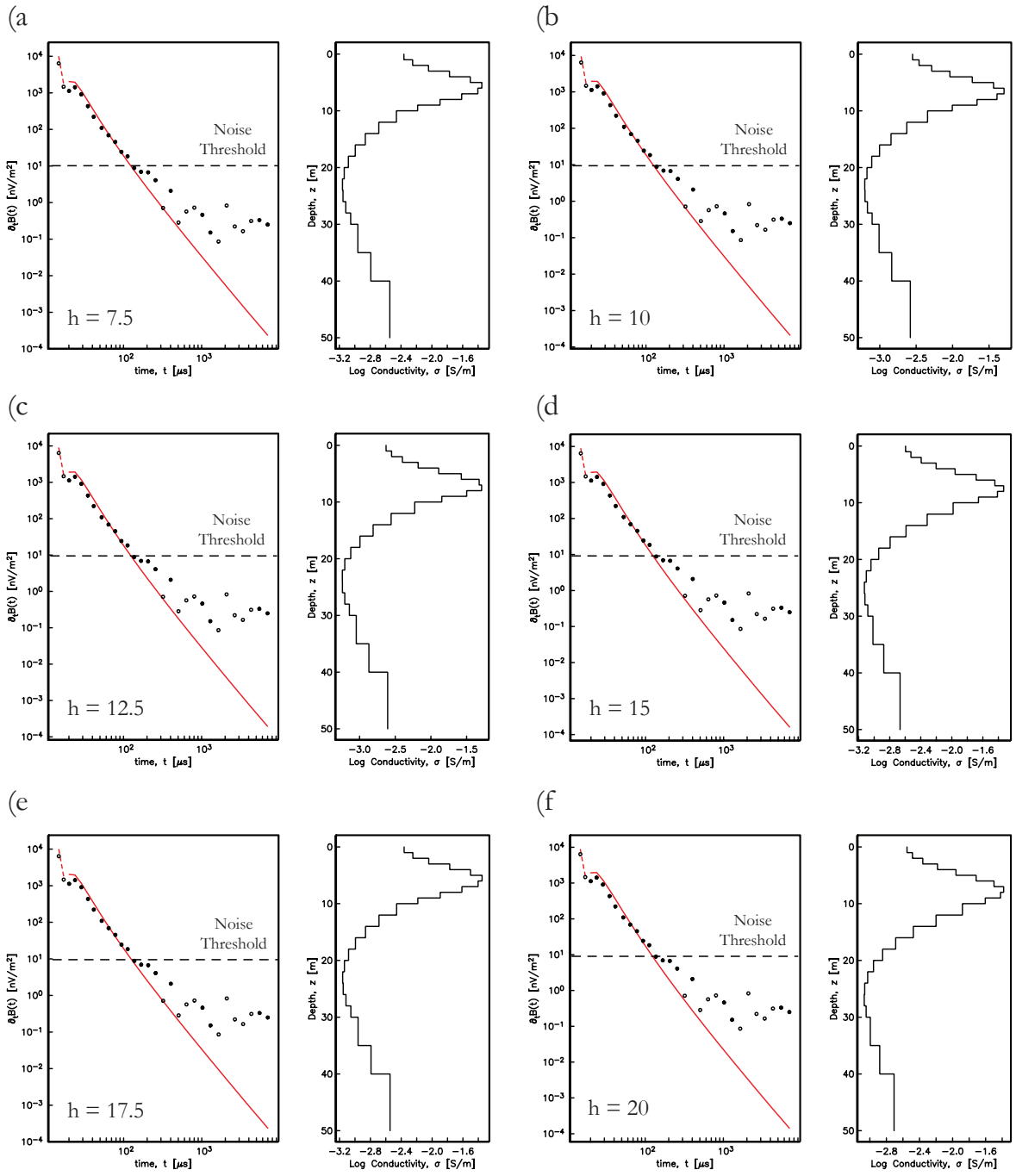


**Figure 4.11a-i.** Comparison of final Occam inversion results (a – i) and the corresponding best-fit model for layer thicknesses of 2.5 m – 30 m respectively derived by ZCMO modeling used as the inversion's starting model. The left panel shows a comparison between the observed data (symbols) and final model response (line) with only data above the $10^{-8}$ V/m$^2$ noise threshold being inverted for. The right panel shows the final Occam 1D conductivity model as a function of depth with log conductivity on the x-axis and depth on the y-axis. Open circles correspond to negative values and closed circles correspond to positive values.

(g

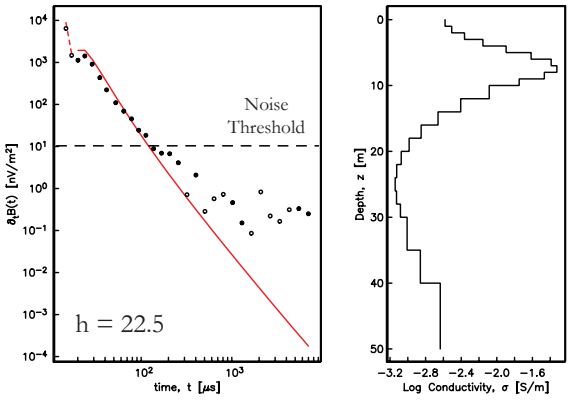
Noise
Threshold
h = 22.5
time, t [μs]
Depth, z [m]
Log Conductivity, σ [S/m]

(h

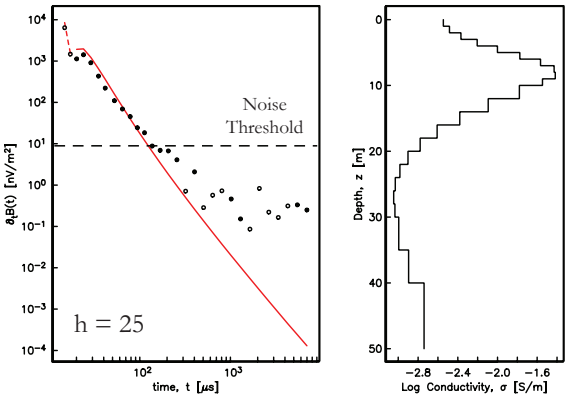
Noise
Threshold
h = 25
time, t [μs]
Depth, z [m]
Log Conductivity, σ [S/m]

(i

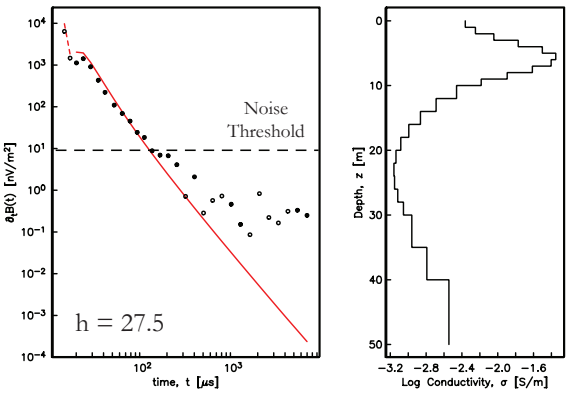
Noise
Threshold
h = 27.5
time, t [μs]
Depth, z [m]
Log Conductivity, σ [S/m]

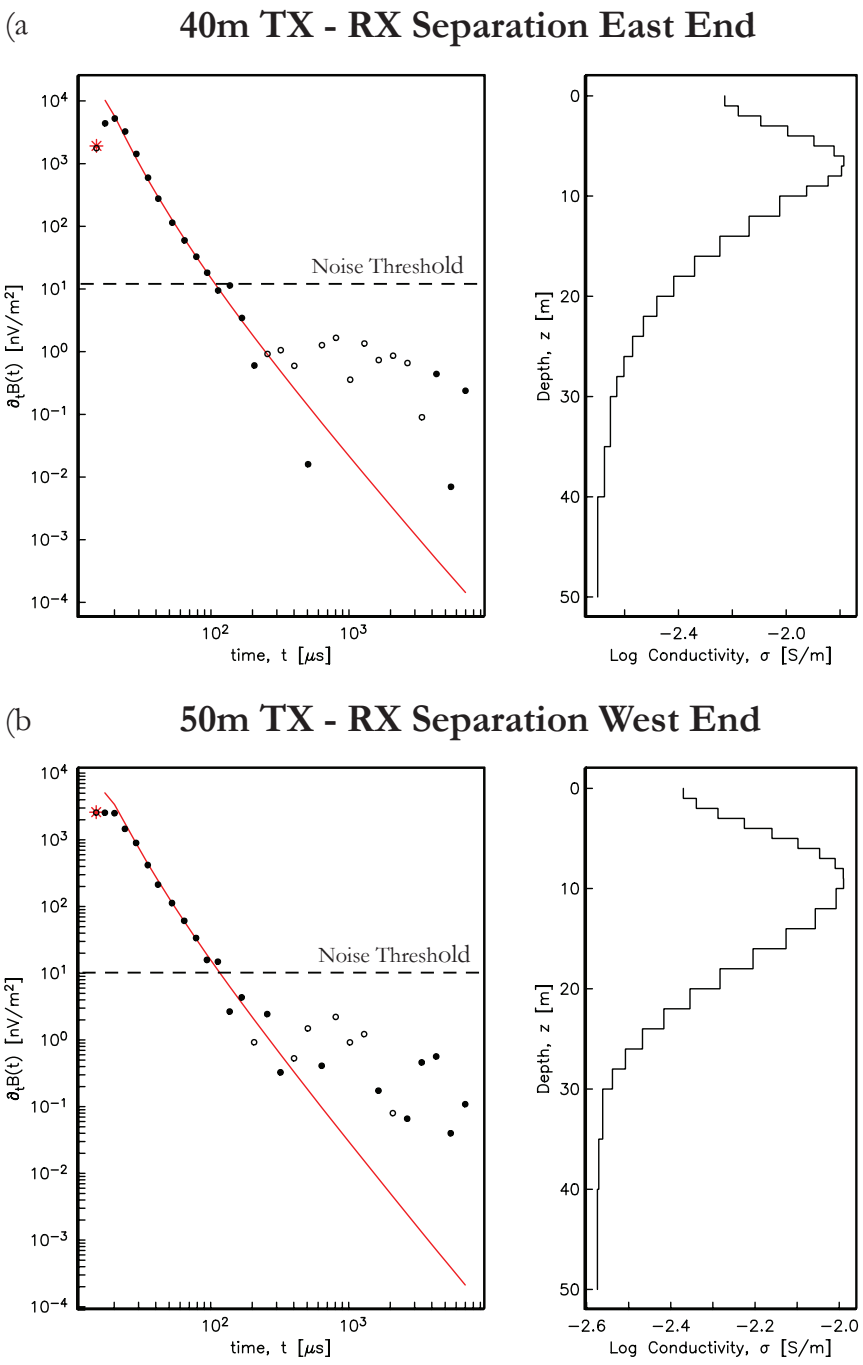


**Figure 4.12a-g.** Seven final Occam inversion results for TX – RX separations: a) 40 m, b) 50 m, c) 60 m, d) 70 m, e) 70 m, f) 80 m, and g) 90 m. Models a, c, and d represent soundings on the Eastern end of the survey line and models b, e, f, and g represent soundings on the Western end. The left panel shows a comparison between observed data (symbols) and final model response (line) with only data above the $10^{-8}$ V/m$^2$ noise threshold (dashed line) being inverted for. The right panel shows the final Occam conductivity model as a function of depth with log conductivity on the x-axis and depth on the y-axis. Open circles correspond to negative values and closed circles correspond to positive values.

(c

## 60m TX - RX Separation East End

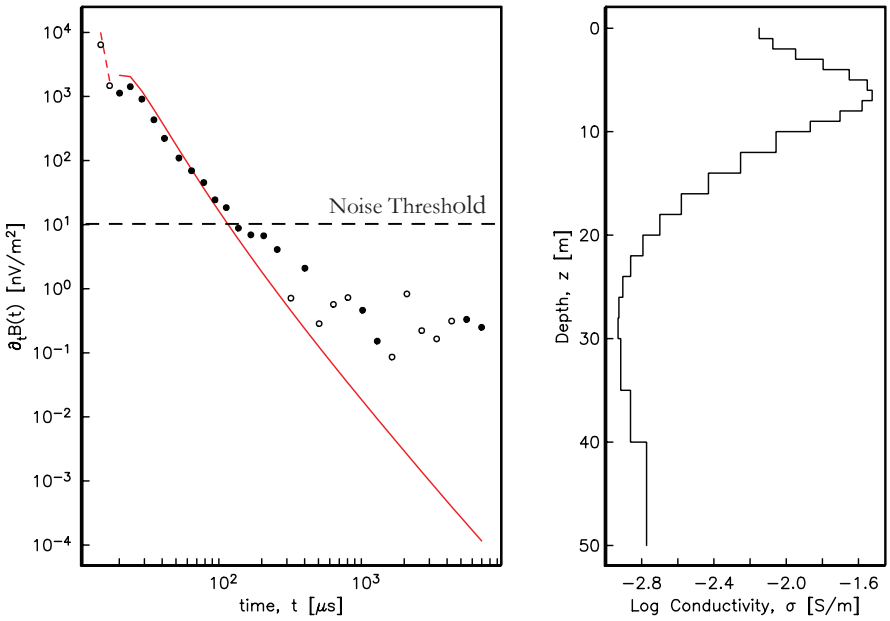


(d

## 70m TX - RX Separation East End

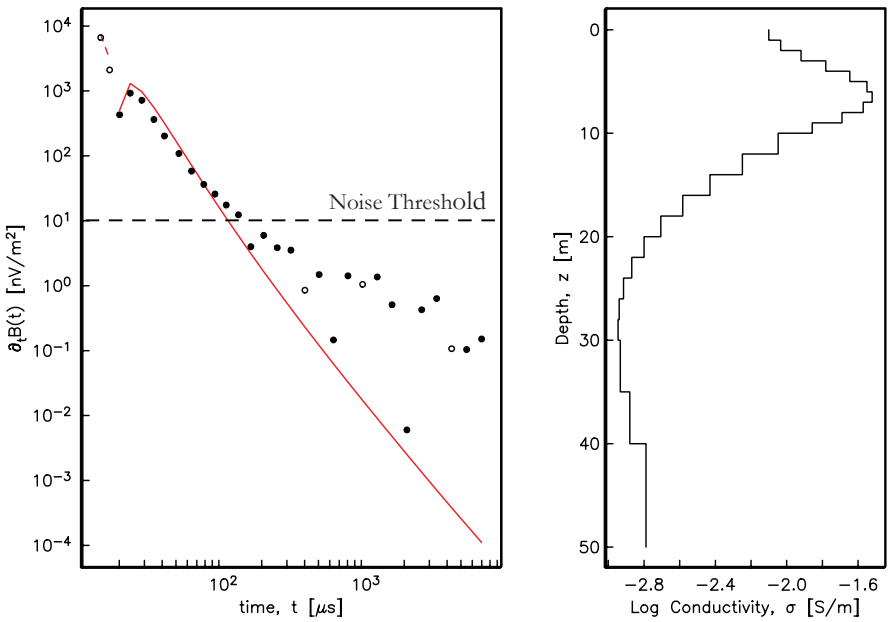

(e

## 70m TX - RX Separation West End

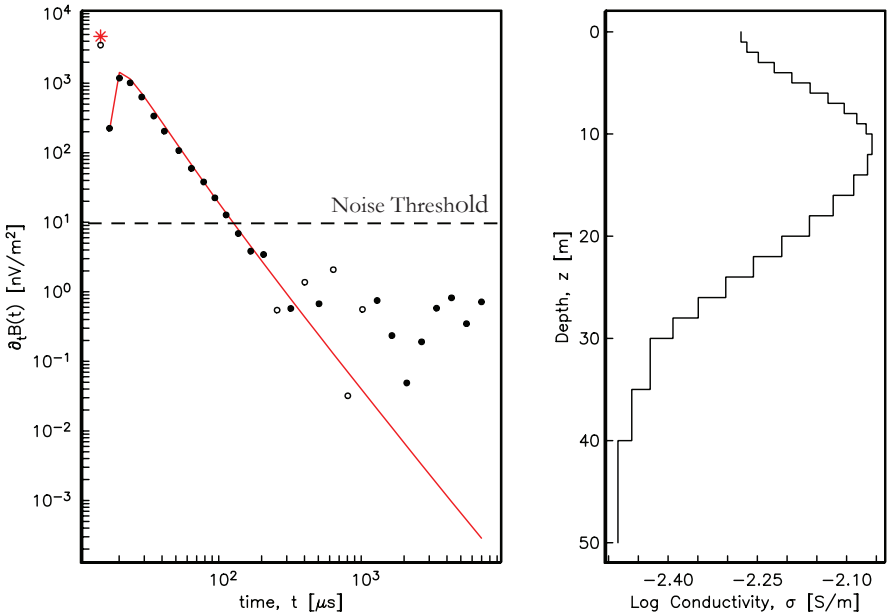


(f

## 80m TX - RX Separation West End

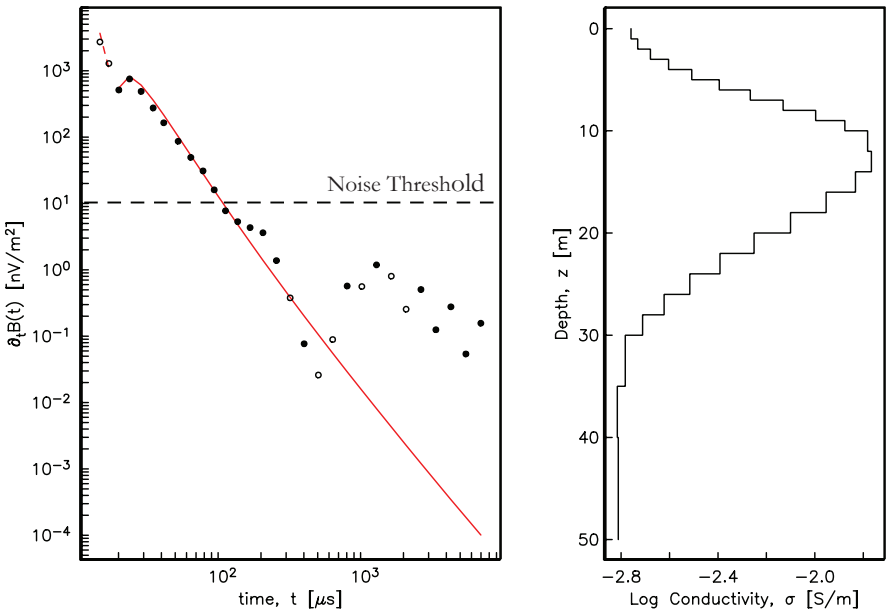

(g

## 90m TX - RX Separation West End

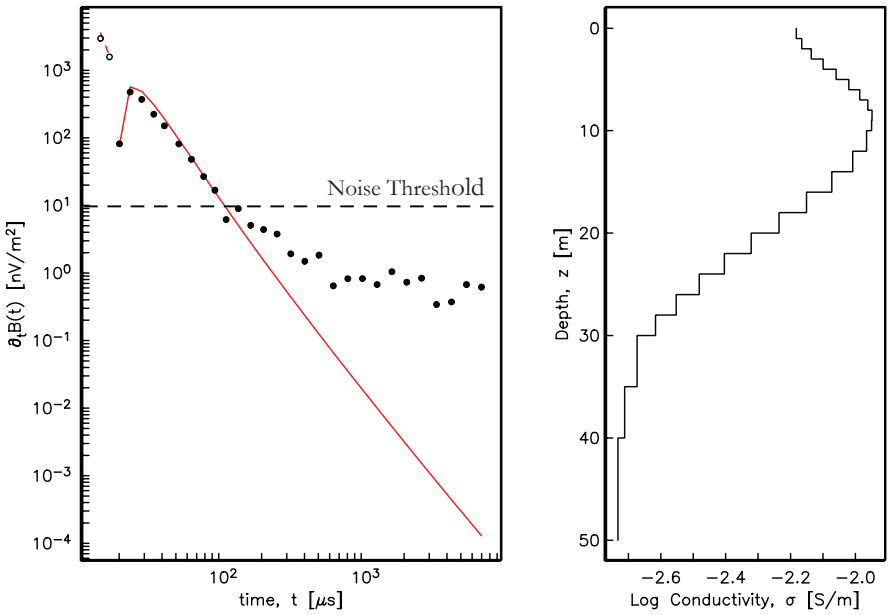

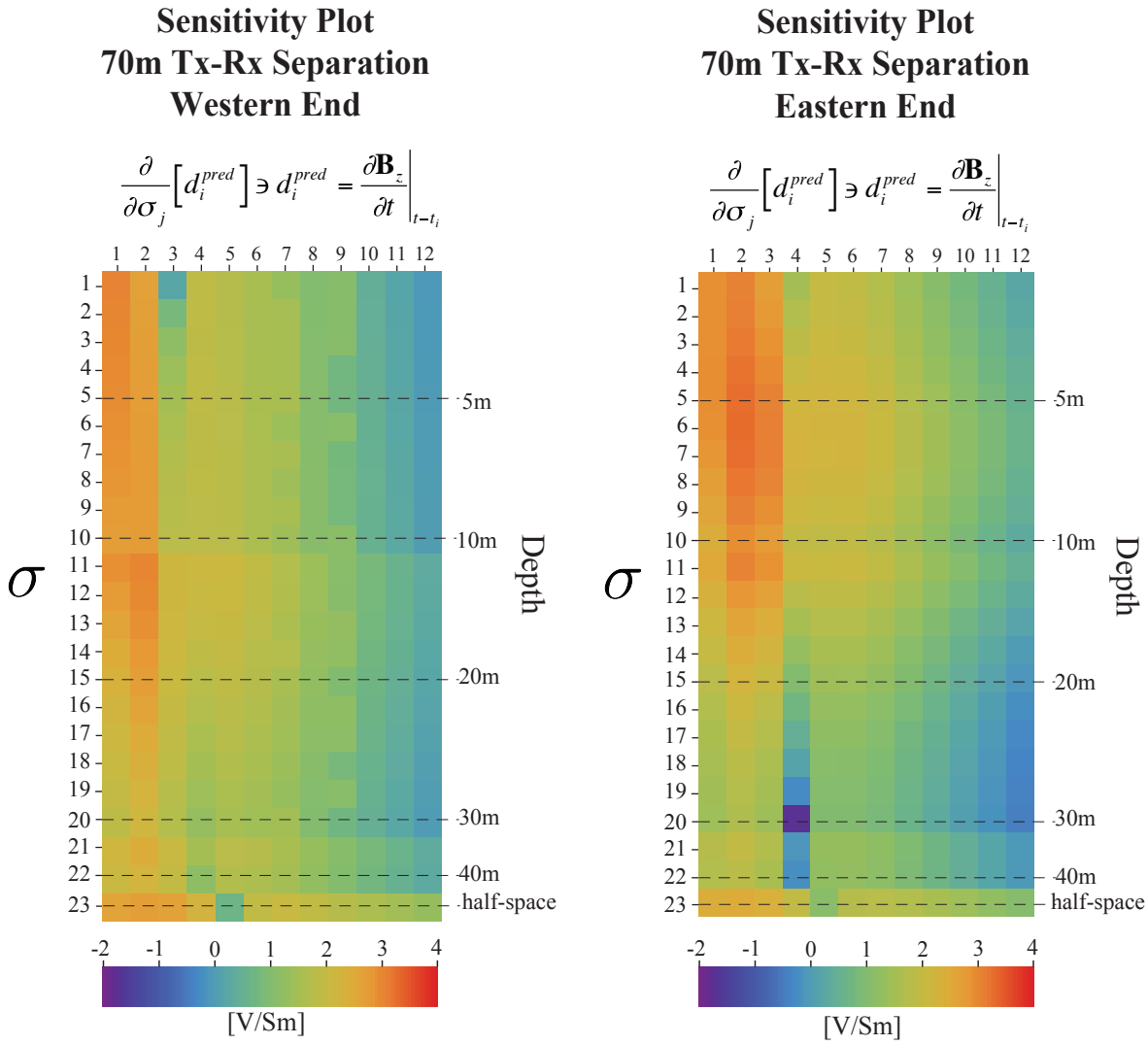


**Figure 4.13.** **S**ensitivity (Jacobian) matrix plots for 70 m TX – RX offset sounding on at both East (a) and West (b) ends of the 40 m terrace profile line. In each sensitivity plot, the horizontal axis is for the first 12 data points and the vertical axis is the 22 model parameters representing layer conductivities in the Earth model. Warm colors indicate increasing sensitivity of a given measurement to a particular model parameter.

# Chapter 5 Discussion and Conclusions

## 5.1 Discussion

### *5.1.1 Interpretation of the 1D Occam inversion results on the 40 m terrace*

A comparison of the final 1D conductivity models for different offsets (L) is shown in figure 5.1. As shown, the models span a broad conductivity range with the depth to the conductivity maximum, $\sigma_{max}$, varying by a much as two meters. Substantial lateral heterogeneity across the profile was observed in the log-normalized $\partial t\mathbf{B}_z$ pseudo-sections. Therefore, by grouping recovered models of similar traverse position, a broader understanding of the profiles overall conductivity can be attained. Recall that an offset electromagnetic induction response is conventionally taken as measure of the "bulk" conductivity between the TX and RX; therefore, a larger portion of the subsurface is sampled with longer offsets. Also, from the synthetic log-normalized $\partial t\mathbf{B}_z$ example, an increasing sensitivity of the measured response to deeper conductivity structure at larger offsets is seen. Hence, careful consideration must be made when correlating inversion results for differing L, especially in laterally heterogeneous environments.

In separating the 40 m terrace conductivity models based on profile location, noticeable similarities and differences are seen. For Eastern models (figure 5.2), similar conductivity values (0.006 S/m – 0.008 S/m) for the surface resistor and terminal half-space (0.0016 S/m – 0.002 S/m) were recovered for all three TX – RX separations. A similar, slightly more resistive, conductivity range (0.007 S/m to 0.004 S/m) is observed for the surface resistor on Western models (figure 5.3); however, the terminal half-space conductivity is more conductive ranging from 0.002 S/m to 0.0036 S/m. For Western models, similarities in $\sigma_{max}$ magnitude (0.01 S/m to 0.012 S/m) and depth (9 m) is observed for all four models in addition to a consistent gradational conductivity decrease to 30 m depth. Conversely, a consistent $\sigma_{max}$ depth of 7 m for all three models on Eastern end of the profile was observed, however the varying magnitude of the $\sigma_{max}$ from the 40 m model (0.016 S/m) to the 60 m and 70 m (0.03 S/m) suggests potentially laterally increasing conductivity between those offsets. Although the terminal half-space conductivities of the three Eastern models are similar, the 40 m model displays a gentle decrease in conductivity, whereas the 60 m and 70 m models decrease rapidly including a noticeable resistive "bulge" feature from 20 m to 40 m depth. One explanation is that the feature could be

the result of increased sensitivity to 3D structure particularly a depression or rise in the bedrock surface at those offsets resulting in higher conductivity maximum magnitudes and the addition of a deeper conductive structure as seen in Goldman et al. (1994). Alternatively, the feature may correspond to a third conductivity boundary – a hypothesis consistent with the observed decrease in eddy current dissipation rate at late times on the inversion results for both 60 m (figure 4.11c) and 70 m (figure 4.11d) offsets. However, being that the change occurs at late times and relatively close proximity to the noise threshold, we hesitate on making any definitive conclusions on its origin at this state of the analysis.

Smooth inversion results display gradational variations in conductivity as a function of depth, which makes the interpretation of a sharp boundary difficult. In theoretical inversion results, sharp boundaries are typically seen at the midpoint of the model's gradational conductivity increases/decreases (Constable et al., 1987; Farquharson & Oldenburg, 1998; Loke et al., 2003). Hence, a similar technique in boundary determination was applied here. It is important to note that these depth estimates are based on a visual approximation of the model and should not be considered as definitive boundary locations. For Eastern models, the basal depth of the $\sigma_{max}$ is 7 m, resulting in boundary estimates (shown by the dashed lines in figure 5.2) of 3.5 m between the surface resistor and secondary conductive layer and 16 m between the conductive layer and the resistive half-space. For Western models, the basal depth of the $\sigma_{max}$ increased to 9m resulting in deeper boundaries of 5 m and 20 m between the resistive surface layer and secondary conductive layer and between the conductive layer and resistive half-space respectively. Given the depth sensitivity of the conductivity models shown in the sensitivity plots (figure 14.3a-b) and the relative consistency of boundary depth between models of varying offset on either side of the profile, we conclude that the conductivity and boundary estimates presented are fair representations of the conductivity structure of the 40 m terrace at Kentland Farm.

Recognizing that in using 1D smooth models to represent a 3D Earth limits the model interpretation to a crude approximation of the subsurface's physical parameters, further qualitative interpretations of structural variations are made across the 40 m terrace profile. The variability observed between the models resulting from a highly complex geologic setting coupled with the smooth model's tendency to overshoot the true conductivity (Loke et al., 2003), constrains interpretation of conductivity to order of magnitude estimates. However, this is

acceptable in many cases given that conductivity of the earth materials seen in this area likely spans several decades in magnitude (figure 1.5). The conductivity of the upper layer ranges from 0.004 S/m to 0.008 S/m and thickens by approximately 1.5 m from the Eastern (d = 3.5 m) end to the Western end (d = 5 m). Also, the thickness of the conductive second layer, which ranges from 0.01 S/m to 0.03 S/m, increases from approximately 12.5 m thick at the Eastern end to 15 m thick at the Western end. Gross soil groupings on the 50 m terrace defined by Schwartz et al. (2008) revealed five laterally heterogeneous soil units within the upper 5 m – 10 m composed of varying degrees of sand, silt, and clay loams with ERI-derived conductivity estimates from 0.0079 S/m to 0.00051 S/m. Although the ERI conductivity range is large, our 1D smooth model represents a bulk average of these thinner soil units and the recovered 1D Occam conductivity ranges can be correlated to the 50 m soil groupings defined in Schwartz et al. (2008). In addition, the Occam derived conductivities for the upper 16 – 20 m of the 40 m terrace lie within the conductivity range given for loam in figure 1.5. Interpretation of the source of the first conductivity boundary is beyond the scope of this study. However, possible causes could be, but are not limited to: An increase in the volume fraction of clay, an increase in porosity, and/or increase in fluid content.

The half-space conductivity from the ZCMO modeling procedure on the 20 m terrace was approximately found to be 0.0024 S/m assuming a two-layer, 1D model with an overburden thickness of 5 m. The range of terminal conductivities from the inversion results is approximately 0.0016 S/m – 0.0036 S/m (275 Ωm – 675 Ωm), which agrees with the 20 m terrace ZCMO result. Referring to electrical conductivities of Earth materials in figure 1.5, the half-space conductivities observed on the 40 m terrace falls at the low end of the limestone conductivity range. Relatively low limestone conductivity values are correlated to a potential increase in sediment or pore fluid occupation of the secondary porosity created from the dissolution or "weathering" of the bedrock surface commonly seen in karstic environments. Therefore, correlation of our final 1D conductivity models with results from the 20 m terrace leads to the conclusion of a "weathered" limestone unit that begins at depths ranging from 16 m to 20 m. Additional information such as drill hole data or the implementation of a 2D or 3D inversion would further constrain these parameter estimates.

*5.1.2 Implications of the interpretations on the geology of the area*

The knowledge of the bedrock depth and geometry on the 40 m terrace at Kentland Farm, VA provides context into geologic processes of the area. Firstly, the interpretation of a Westerly increasing bedrock depth provides additional insight into the hydrological framework of the 40 m terrace. Daily precipitation totals (mm) in Blacksburg, VA (≈ 13km from the 40 m terrace field site) and Dublin, VA (≈ 10km from the 40 m terrace field site) are shown in figure 5.4 from 03/24/2009 to 04/23/2009 with the highlighted areas corresponding to days of data collection. Although total precipitation in both areas varied substantially, the timing of precipitation events is consistent for both areas. Therefore, for a given day in which it rained in Blacksburg and Dublin, we can assume that it rained at the field site as well. From the topographic map of the field site (figure 5.5), it is shown that the natural drainage path for groundwater from the 70 m terrace, intersects the Western portion of the 40 m terrace line. Hence, the increased thickness of the conductive second layer may be attributed to an excess of water from drainage on the Western end of the profile. In addition, the acquisition of an additional multi-fold TDEM profile perpendicular to the 40 m terrace profile line shown in this study would provide additional constraints on groundwater flow as well as bedrock orientation. The interpretation of a limestone bedrock depth of 16 m – 20 m has additional implications on the geomorphological history of the area. Ward et al. (2005) proposed that a thick alluvium fill, reaching approximately 128m AMRL, was deposited on a ≈ 15 m bedrock strath with the remaining river terraces created by a series of down-cutting events spanning ≈ 2 mya to ≈ 1 mya. The thickness of the observed soil unit on the 40 m terrace contradicts previous interpretations of it being a strath terrace overlain by a thin layer of alluvium and rather is consistent with the

fill-cut terrace model. Therefore, the interpreted thickness of the soil unit as well as the 20 m ZCMO inversion estimate of a 5 m depth to bedrock supports the aggradation/incision history previously described Ward et al. (2005). With the large depth sensitivity to structure (> 40 m depth) shown in the sensitivity plots (figure 4.13a-b), additional multi-fold TDEM surveys on the upper terraces at Kentland Farm could provide additional constraints on the geomorphological history of the New River by estimating depth to bedrocks that are currently unknown.

*5.1.3 Synthesis of the three analysis methods*

The multi-fold TDEM experimental design inherently provides the ability to analyze our robust data set using multiple techniques. Each of the three independent analysis techniques – log-normalized $\partial t\mathbf{B}_z$ pseudo-sections, ZCMO inversion, and regularized 1D Occam inversion – yielded a unique interpretation, which was synthesized into a complementary interpretation of the conductivity structure of the 40 m terrace at Kentland Farm. Figure 5.6 shows the recovered conductivity model for each of the three analysis methods. From the log-normalized $\partial t\mathbf{B}_z$ pseudo-sections (figure 5.6a), two laterally varying structural boundaries were qualitatively interpreted across the profile, however firm conductivity or depth values were unable to be assigned to these boundaries. Through ZCMO inversion (figure 5.6b), an estimate of a 17.5 m soil overburden with conductivity of 0.02 S/m overlying the 0.0025 S/m limestone bedrock was made, however the structural model did not represent the lateral variability observed in the pseudo-sections. Regularized 1D Occam inversion provided the final, two-layer structural model (figure 5.6c) consisting of a Westerly thickening upper loam layer (3.5 m in the East and 5 m in the West) over a more conductive Westerly thickening loam layer (12.5 m in the East and 15 m in the West) overlying a "weathered" limestone bedrock. Although the final conductivity model was obtained through regularized 1D Occam inversion, the result was dependent on the information provided from the other two analyses. Recognition of the lateral heterogeneity of the 40 m terrace profile obtained from the pseudo-sections revealed the need to analyze models from each end of the profile independently. Also, the requirement of a sufficient starting model for the Occam inversion was satisfied through the use of the ZCMO inversion derived conductivity estimate. Hence, the ability to perform multiple analysis of the data set was critical to the interpretations made on the 40 m terrace at Kentland Farm.

## 5.2 Conclusions

The complexity of the sedimentary structures and the karstic nature of the underlying bedrock coupled with a lack of *a priori* information on the 40 m terrace at Kentland Farm create a very difficult setting for geophysical exploration. Implementation of our optimal, multi-fold TDEM experimental design resulted in the acquisition of a robust data set that can be analyzed in

multiple fashions. By harmonizing results from three different analysis techniques – log-normalized $\partial t\mathbf{B}_z$ common offset pseudo-sections, zero crossing moveout analysis, and regularized 1D inversion – interpretations of the physical properties of the 40 m terrace were made. Results from a novel ZCMO inversion procedure provided an accurate approximation of the electrical structure on the 20 m terrace. Hence, ZCMO inversion result from the 40 m terrace were used to constrain the starting model used in the inversions, which is required for a successful solution. Final 1D conductivity models outlines a westerly dipping, three-layered electrical structure (resistor/conductor/resistor) with approximate layer boundaries of 3.5 m to 5 m and 16 m to 20 m, interpreted to be the limestone bedrock interface, respectively. Log-normalized $\partial t\mathbf{B}_z$ pseudo-sections revealed the lateral heterogeneity of the section, specifically the increased thickness of the conductive layer to the West. However the observed secondary Easterly increasing conductivity boundary could not be explained in the inversion results, outlining the perils of over-interpretation of the pseudo-sections. Additionally, the best-fitting two-layer model derived from the ZCMO estimation generally agrees with the recovered inversion results, thus confirming the potential for ZCMO analysis to be used in geophysical characterization of the subsurface. Because the ZCMO behavior of eddy currents in a 3D medium is relatively unknown, additional research into the potential use of ZCMO analysis to distinguish lateral variations in electrical structure with the use a 3D forward solver would further refine the ability of ZCMO model estimation to answer complex geologic problems. Also, the synthesis of an eddy current travel-time inversion would allow for the inclusion of multi-layered structure. Further inclusion of first order geologic information – depth to bedrock for instance – as well as the incorporation of a 3D time domain inversion would significantly improve the resolving capabilities of the multi-fold TDEM survey and should be considered as an area for future research. Although only broad approximations of the conductivity structure on 40 m terrace at Kentland Farm were made, the interpretations here complement and extent the previous resistivity work (Schwartz et al., 2008) and gemorphological models (Ward et al., 2005). The rich combination of analysis opportunities brought forth by the full-fold TDEM experiment are not only critical to the conclusions drawn here, but also aligned with our general philosophical approach to science: to maximize the likelihood of making sound inferences of the Earth's interior.

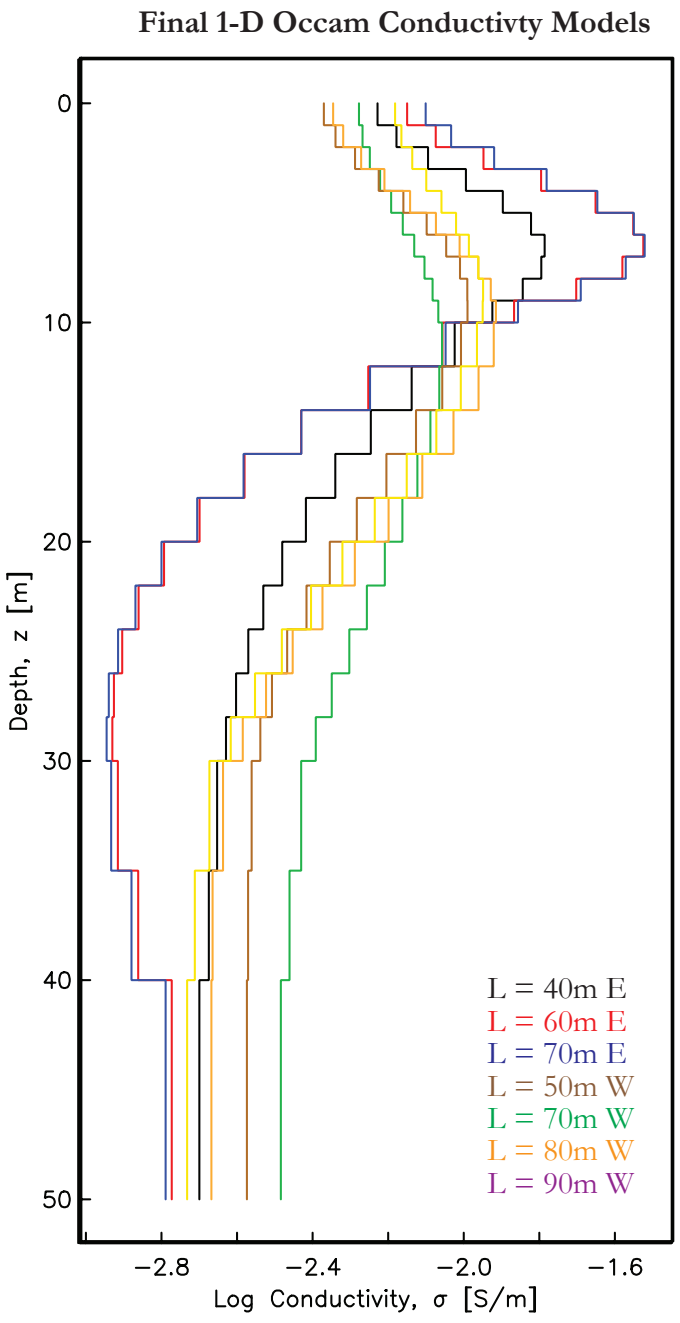


**Figure 5.1.** Comparison of the final recovered 1D conductivity models for all seven inversion results (colored lines) for TX – Rx separations ranging from 40 m to 90 m on the 40 m terrace at Kentland, Farm VA.

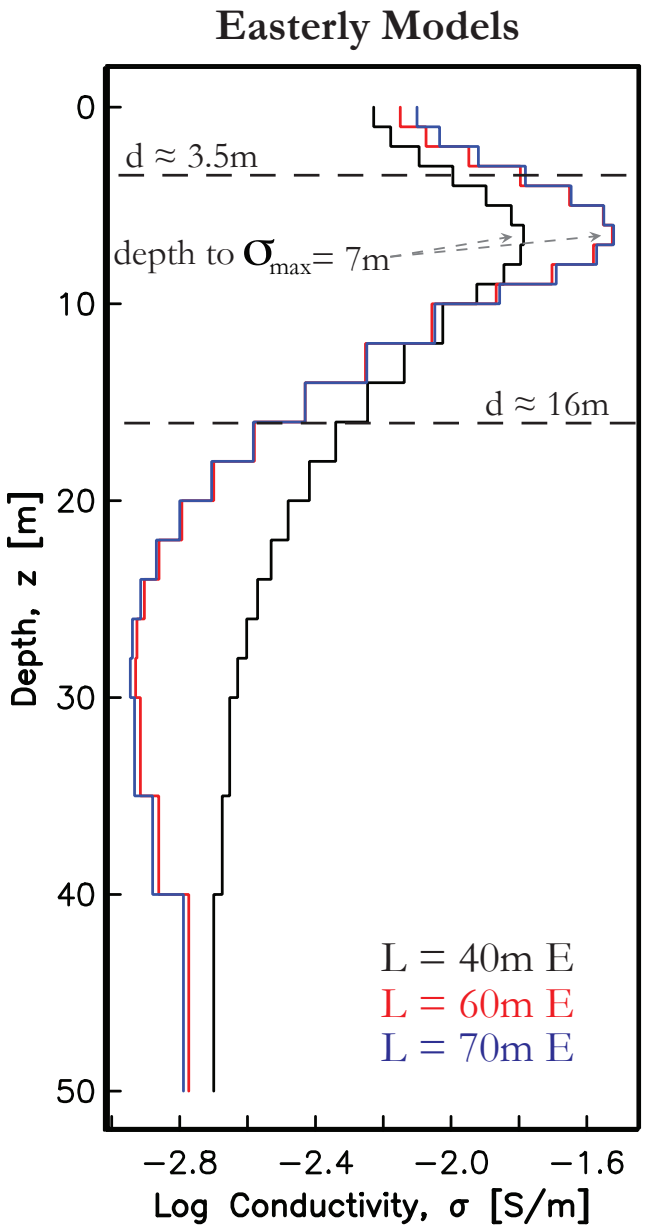


**Figure 5.2.** Final 1D conductivity models for soundings on the Eastern portion of the profile for TX – RX separations of 40 m (black), 60 m (red), and 70 m (blue). The model depth corresponding to the conductivity maximum is shown by the dashed-grey arrows. The dashed lines indicate the inferred layer depth.

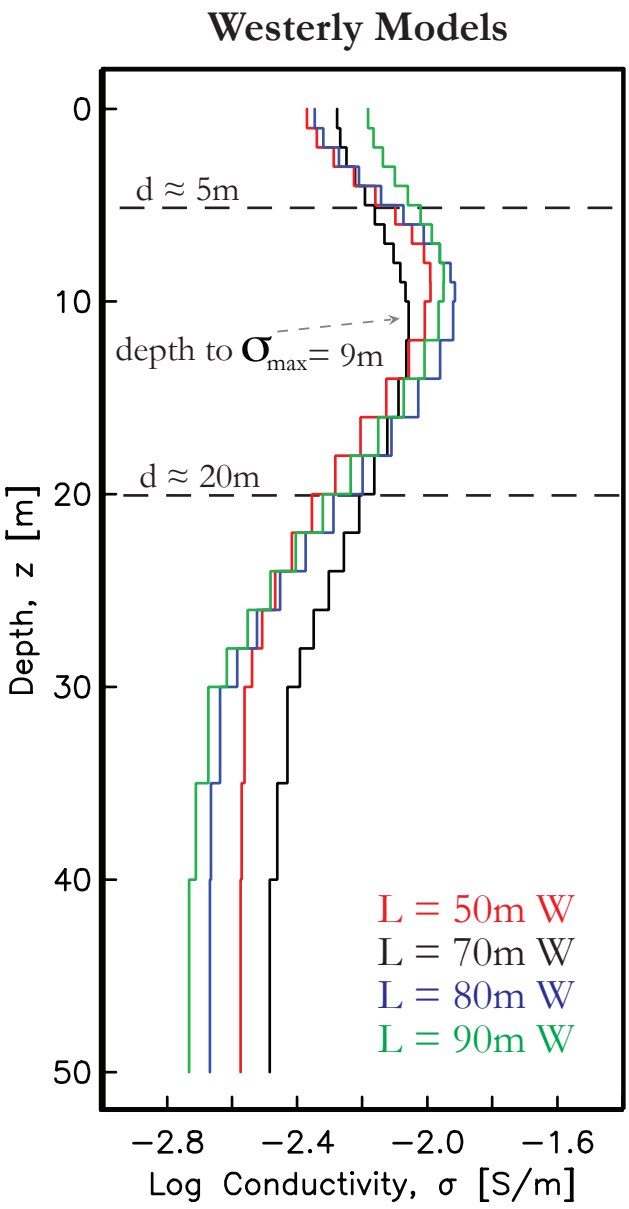


**Figure 5.3.** Final 1D conductivity models for soundings on the Western portion of the profile for TX – RX separations of 50 m (red), 70 m (black), 80 m (blue), and 90 m (green). The model depth corresponding to the conductivity maximum is shown by the dashed-grey arrows. The dashed lines indicate the inferred layer depth.

| Date | Total Precipitation (mm) Dublin, VA | Total Precipitation (mm) Blacksburg, VA |
|---|---|---|
| 3/24/09 | 0 | 0 |
| 3/25/09 | 2.54 | 14.22 |
| 3/26/09 | 3.3 | 9.652 |
| 3/27/09 | 1.78 | 8.636 |
| 3/28/09 | 1.78 | 6.35 |
| 3/29/09 | 0 | trace |
| 3/30/09 | 0 | trace |
| 3/31/09 | 0 | trace |
| 4/1/09 | 2.29 | 5.33 |
| 4/2/09 | 1.02 | 8.38 |
| 4/3/09 | 4.83 | 4.32 |
| 4/4/09 | 0 | 0 |
| 4/5/09 | 0 | 0 |
| 4/6/09 | 0.76 | 1.78 |
| 4/7/09 | 0 | trace |
| 4/8/09 | 0 | 0 |
| 4/9/09 | 0.25 | 2.54 |
| 4/10/09 | 1.27 | 5.59 |
| 4/11/09 | 1.52 | 1.52 |
| 4/12/09 | 0 | 0 |
| 4/13/09 | 0 | 2.03 |
| 4/14/09 | 1.27 | 6.1 |
| 4/15/09 | 0 | 0 |
| 4/16/09 | 0 | 0 |
| 4/17/09 | 0 | 0 |
| 4/18/09 | 0 | 0 |
| 4/19/09 | 0 | 3.3 |
| 4/20/09 | 0.25 | 28.45 |
| 4/21/09 | 0.25 | 0.25 |
| 4/22/09 | 0 | trace |
| 4/23/09 | 0 | 0 |

**Figure 5.4.** Daily precipitation totals (mm) in Blacksburg, VA (≈13km from the 40 m terrace field site) and Dublin, VA (≈10km from the 40 m terrace field site) are shown in figure 5.4 from 03/24/2009 to 04/23/2009 with the highlighted areas corresponding to days of data collection (data from Weather Underground, 2010).

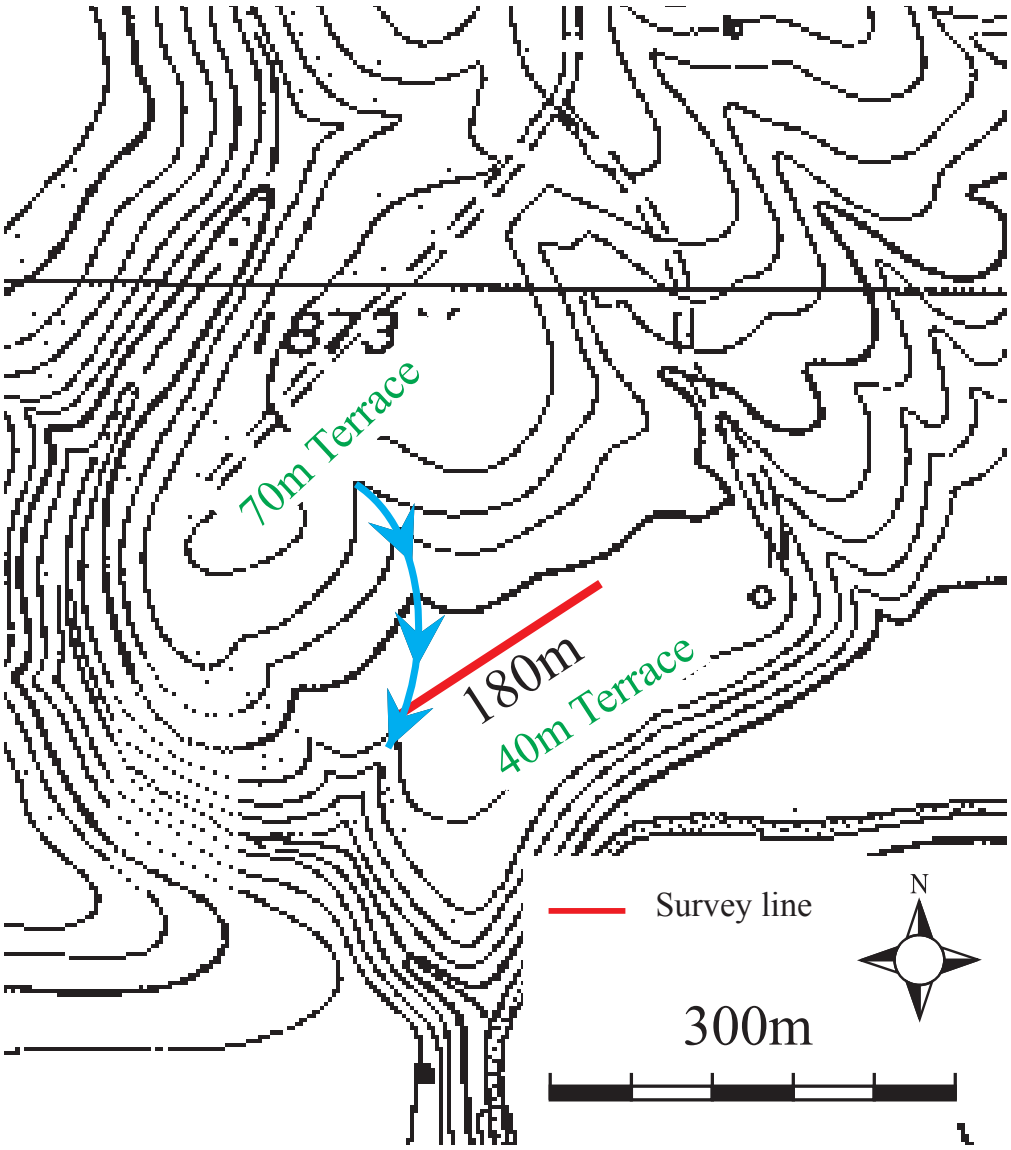


**Figure 5.5.** Topographic map of the Kentland Farm 40 m terrace field site with the red line indicating the 180 m survey line. The blue curve represents the natural drainage path from the 70 m terrace that may result in an increase in groundwater at the West end of the profile line (U.S. Geological Survey, 1998)

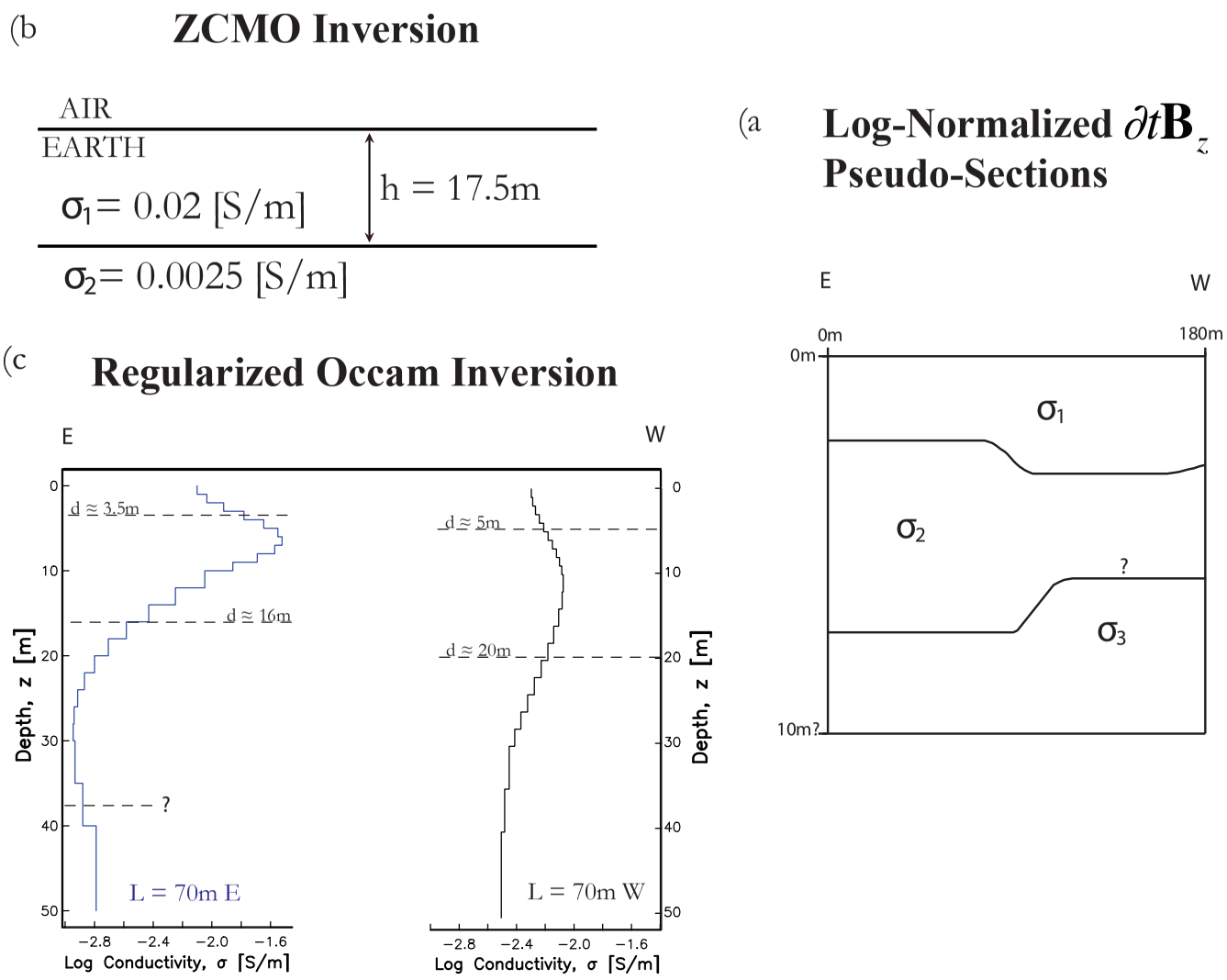


**Figure 5.6.** Final structural models derived from the three analysis methods: Log-normalized $\mathbf{dB}_z/dt$ pseudo-sections (a), ZCMO inversion (b), and regularized 1D Occam inversion (c).

## References


Angenheister G. (ed.) 1982. *Physical Properties of Rocks*, Vol. 1b, In Landolt-Bornstein (ed. K.H. Hellwege). Springer-Verlag, Inc.

Archie, G. E. (1942). The electrical resistivity log as an aid in determining some reservoir characteristics. *Petroleum Transactions*, AIME 146, 54-62.

Boerner, D. E., & West, G. F. (1989). Frechet derivatives and single scattering theory. *Geophysics Journal International,* 98 (2), 385-390.

Buselli, G., Barber, C., Davis, G. B., & Salama, R. B. (1990). Detection of groundwater contamination near waste disposal sites with transient electromagnetic and electrical methods. In S. H. Ward (Ed.), *Geotechnical and Environmental Geophysics,* (Vol. 2, pp. 27-39). Tulsa, OK. Society of Exploration Geophysicists.

Butler, D. K. (2005). What is near-surface geophysics? In D. K. Butler (Ed.), *Near Surface Geophysics* (pp. 1-6). Tulsa, OK. Society of Exploration Geophysicists.

Chave, A. D. (1984). The Fréchet derivatives of electromagnetic induction. *Journal of Geophysical Research, 89* (B5), 3373-3380.

Collins, J. L., Everett, M. E., & Johnson, B. (2006). Detection of near-surface horizontal anisotropy in a weathered metamorphic schist at Llano Uplift (Texas) by transient electromagnetic induction. *Physics of the Earth and Planetary Interiors, 158*, 159-173.

Constable, S. C., Parker, R. L., & Constable, C. G. (1987). Occam's inversion: A practical algorithm for generating smooth models from electromagnetic sounding data. *Geophysics, 52* (3), 289-300.

Danielsen, J. E., Auken, E., & Jorgensen, F. S. (2003). The application of the transient electromagnetic method in hydrophysical surveys. *Journal of Applied Geophysics, 53*, 181-198.

Eaton, P. A., & Hohmann, G. W. (1987). An evaluation of electromagnetic methods in the presence of geologic noise. *Geophysics, 52* (8), 1106-1126.

Everett, M. E. (2005). What do electromagnetic induction responses measure. *The Leading Edge*, 154-157.

Everett, M. E., & Weiss, C. J. (2002). Gelogical noise in near-surface controlled-source electromagnetic data. *Geophysical Research Letters, 29*, 2001GL014049.

Everett, M., & Meju, M. (2005). Near-surface controlled-source electromagnetics: Background and recent advances. In: Y. R. Hubbard (Ed.), *Hydrogeophysics* (Vol. 50). New York: Springer.

Farquharson, C. G., & Oldenburg, D. W. (1998). Non-linear inversion using general measures of data misfit and model structure. *Geophysics Journal International, 134*, 213-227.

Fitterman, D. V., & Labson, V. F. (2005). Electromagnetic induction methods for environmental problems. In D. K. Butler (Ed.), *Near-Surface Geophysics* (pp. 301-355). Tulsa, OK: Society of Exploration Geophysicists.

Frischknecht, F. C., Labson, V. C., Spies, B. R., & Anderson, W. L. (1991). Profiling methods using small sources. In M. N. Nabighian (Ed.), *Electromagnetic Methods in Applied Geophysics* (Vol. 2, pp. 105-283). Tulsa, OK: Society of Exploration Gephysicists.

Gomez-Trevino, E., & Edwards, R. N. (1983). Electromagnetic soundings in the sedimentary basin of southern Ontario - A case history. *Geophysics, 48* (3), 311-330.

Granger, D., Kirchner, J., & Finkel, R. (1997). Quaternary downcutting rate of the New River, Virginia, measured from differential decay of cosmogenic Al-26 and Be-10 in cave-deposited alluvium. *Geology, 25* (2), 107-110.

Harris, W. G., Iyengar, S. S., Zelazny, L. W., Parker, J. C., Lietzke, D. A., & Edmonds, W. J. (1980). Mineralogy of a chronosequence formed in New River alluvium. *Soil Society of America Journal, 44*, 862-868.

Hashin, Z., Shtrikman, S. (1962). A variational approach to the theory of the effective magnetic permeabillity of multiphase materials. *Journal of Applied Physics, 33* (10), 3125-3131.

Hoekstra, P., & Blohm, M. W. (1990). Case histories of time domain electromganetic sounding in environmental geophysics. In S. H. Ward (Ed.), *Investigations in Geophysics No.5: Geotechnical and Environmental Geophysics* (Vol. 2, pp. 1-14). Tulsa, OK: Society of Exploration Geophysicists.

Hordt, A. (1998). Calculation of electromagnetic sensitivities in the time domain. *Geophysics Journal International, 133*, 713-720.

Hoversten, G. M. (1982). Transient fields of a current loop source above a layered Earth. *Geophysics, 47* (7), 1068-1077.

Karato, S. (1990). The role of hydrogen in th electrical conductivity of the upper mantle. *Nature, 347*, 272-273.

Knight, R., & Endres, A. (2005). An introduction to rock physics principles for near-surface geophysics. In D. K. Butler (Ed.), *Near Surface Geophysics* (pp. 30-70). Tulsa: Society of Exploration Geophysicists .

Lamb, H. (1945). *Hydrodynamics*. New York: Dover Publications.

Loke, M. A. (2003). A comparison of smooth and blocky inversion methods in 2D electrical imaging surveys. *Exploration Geophysics, 34*, 182-187.

Maurer, H., & Boerner, D. E. (1998). Optimized and robust experimental design: A non-linear application to EM sounding. *Geophysics Journal International, 132*, 458-468.

Maurer, H., Boerner, D. E., & Curtis, A. (2000). Design strategies for electromagnetic geophysical surveys. *Inverse Problems, 16*, 1097-1117.

McNeill, J. D. (1980). Applications of transient electromagnetic technics, Technical Note TN-7. Geonics Limited, Mississauga, Ontario, Canada.

McNeill, J. (1994). Technical Note TN-27, Principles and application of time domain electromagnetic techniques for resistivity sounding. Geonics Limited, Mississauga, Ontario, Canada

Meju, M. A., Fenning, P., & Hawkings, T. (2000). Evaluation of small-loop transient electromagnetics soundings to locate the Sherwood Sandstone aquifer and confining formations at well sites in the Vale of York, England. *Journal of Applied Geophysics, 44*, 217-236.

Mills, H. H., & Wagner, J. A. (1985). Long-term change in regime of the New River indicated by vertical variation in extent and weathering intensity of alluvium. *Journal of Geology, 93*, 131-142.

Nabighian, M. N. (1979). Quasi-static transient response of a conducting half-space: an approximate representation. *Geophysics, 44*, 1700-1705.

Nabighian, M., & Macnae, J. (1991). Time domain electromagnetic prospecting methods. In M. N. Nabighian (Ed.), *Electromagnetic Methods in Applied Geophysics* (Vol. 2, pp. 427-520). the Society of Exploration Geophysicists.

Nielsen, L., Jorgensen, N. O., & Gelting, P. (2007). Mapping of the freshwater lens in a coastal aquifer on the Keta Barrier (Ghana) by transient electromagnetic soundings. *Journal of Applied Geophysics, 62* (1), 1-15.

Ogilvy, R. D. (1986). Transient electromagnetic studies over a Cu-Zn-Au mineral prospect Gairloch, Scotland. *Journal of Geological Society, London, 143*, 551-568.

Palacky, G., & West, G. (1991). Airborne electromagnetic methods. In M. N. Nabighian (Ed.), *Electromagnetic Methods in Applied Geophysics* (Vol. 2, pp. 811-880). Society of Exploration Geophysicists.

*PROTEM 47D OPERATING MANUAL for 20/30 Gate Model.* Mississauga, Ontario, Canada: Geonics Limited (2006).

Rath, V., Radic, T., & Krause, Y. (1999). Use of 3D modeling in design of a new type of near-surface survey. In M. O. Spies (Ed.), *Three-Dimensional Electromagnetics* (pp 658-667). Tulsa, OK: the Society of Exploration Geophysicists.

Ryu, J. H., & Morrison, F. W. (1970). Electromagnetic fields about a loop source of current. *Geophysics, 35* (5), 862-896.

Santamarina, J., Rinaldi, V. A., Fratta, D., Klein, K. A., Wang, Y.-H., Cho, G. C., et al. (2005). A survey of elastic and electromagnetic properties of near-surface soils. In D. K. Butler (Ed.), *Near Surface Geophysics* (pp. 71-87). Tulsa, OK: the Society of Exploration Geophysicists.

Schwartz, B. F., Schreiber, M. E., & Yan, T. (2008). Quantifying field-scale soil moisture using electrical resistivity imaging. *Journal of Hydrology, 362*, 234-246.

Sharma, P. V. (1997). *Environmental and engineering geophysics.* Cambridge University Press.

Sheriff, R. E., & Geldart, L. P. (1995). *Exploration Seismology* (Second Edition ed.). New York: Cambridge University Press.

Shultz, A. P., & Bartholomew, M. J. (2009). Geologic map of the Radford North quadrangle, Virginia. *Viginia Division of Geology and Mineral Resources Open File Report 09-01*. www.dmme.virginia.gov

Spies, B. R. (1989). Depth of investigation in electromagnetic sounding methods. *Geophysics, 54* (7), 872-888.

Spies, B. R. (1988). Local noise prediction filtering for central induction transient electromagnetic soundings. *Geophysics, 53* (8), 1068-1079.

Spies, B. R., & Frischknecht, F. C. (1991). Electromagnetic sounding. In M. N. Nabighian (Ed.), *Electromagnetic Methods in Applied Geophysics* (Vol. 2, pp. 285-426). Tulsa, OK: Society of Exploration Geophysicists.

Sumanovac, F., & Weisser, M. (2001). Evaluation of resistivity and seismic methods for hydrogeological mapping in karstic terrains. *Journal of Applied Geophysics, 47*, 13-28.

Swift Jr., C. M. (1988). Fundamentals of the electromagnetic method. In M. N. Nabighian (Ed.), *Electromagnetics Methods in Applied Geophysics Volume 1, Theory* (pp. 5-10). Tulsa, OK: the Society of Exploration Geophysicists.

USDA-NRCS. (2010). *Web Soil Survey*. www.websoilsurvey.com. Retrieved July 11th, 2010.

U.S. Geological Survey. *Raleigh West quadrangle, North Carolina* [map]. 1:24,000. 7.5 Minute Series. Reston, Va: United States Department of the Interior, USGS, 1998.

Ward, D. J., Spotila, J. A., Hancock, G. S., & Galbraith, J. M. (2005). New constraints on the late Cenozoic incision history of the New River, Virginia. *Geomorphology, 72*, 54-72.

Weiss, C. J. (2007). Anomalous diffusion of electromagnetic eddy currents in geological formations. *Journal of Geophysical Research, 112* (B08102).

Weiss, C. J. (2010). *The electromagnetic response of a layered Earth to an inductively-coupled, circular-loop antenna.* Viginia Tech, Geosciences. Unpublished Course Notes.

Weitemeyer, K. A. (2008). *Marine electromagnetic methods for gas hydrate characterization.* University of California, San Diego Scripps Institution of Oceanography.

Wenbo Wei, et. al. (2001). Detection of Widespread Fluids in the Tibetan Crust by Magnetotelluric Studies. *Science, 292* (pp. 716-718).

West, G. F., & Macnae, J. (1991). Physics of the electromagnetic induction exploration method. In M. N. Nabighian (Ed.), *Electromagnetic methods in applied Geophysics* (Vol. 2, pp. 5-45). Tulsa: Society of Exploration Geophysicists.

Weather Underground, Inc. (2010). *Precipitation data from 03/24/2009 to 04/23/2009 at Blacksburg, VA and Dublin, VA.* Retrieved August 8, 2010, from Weather Underground: http://www.wunderground.com/history/

White, W. B., Culver, D. C., Herman, J. S., Kane, T. C., & and Mylroie, J. E. (1995). Karst lands: The dissolution of caronate rock produces uniques landscapes and poses significant hydrological and environmental concerns. *American Scientist, 83* (5), 450-459.

Ziolkowski, A., Hobbs, B. A., & Wright, D. (2007). Multitransient electromagnetic demonstration survey in France. *Geophysics, 72* (4), F197-F209.